BOUNDARY-LAYER STABILITY AND TRANSITION ON A FLARED CONE IN A MACH 6 QUIET WIND TUNNEL

A Dissertation

by

JERROD W. HOFFERTH

Submitted to the Office of Graduate Studies of
Texas A&M University
in partial fulfillment of the requirements for the degree of

DOCTOR OF PHILOSOPHY

Chair of Committee,	William Saric
Committee Members,	Rodney Bowersox
	Prabir Daripa
	Helen Reed
	Edward White
Head of Department,	Rodney Bowersox

August 2013

Major Subject: Aerospace Engineering

ABSTRACT

A key remaining challenge in the design of hypersonic vehicles is the incomplete understanding of the process of boundary-layer transition. Turbulent heating rates are substantially higher than those for a laminar boundary layer, and large uncertainties in transition prediction therefore demand conservative, inefficient designs for thermal protection systems. It is only through close collaboration between theory, experiment, and computation that the state of the art can be advanced, but experiments relevant to flight require ground-test facilities with very low disturbance levels.

To enable this work, a unique Mach 6 low-disturbance wind tunnel, previously of NASA Langley Research Center, is established within a new pressure-vacuum blow-down infrastructure at Texas A&M. A 40-second run time at constant conditions enables detailed measurements for comparison with computation. The freestream environment is extensively characterized, with a large region of low-disturbance flow found to be reliably present for unit Reynolds numbers $Re < 11\times10^6$ m^{-1}.

Experiments are performed on a 5º half-angle flared cone model at $Re = 10\times10^6$ m^{-1} and zero angle of attack. For the study of the second-mode instability, well-resolved boundary-layer profiles of mean and fluctuating mass flux are acquired at several axial locations using hot-wire probes with a bandwidth of 330 kHz. The second mode instability is observed to undergo significant growth between 250 and 310 kHz. Mode shapes of the disturbance agree well with those predicted from linear parabolized stability equation (LPSE) computations. A 17% (40 kHz) disagreement is observed in

the frequency for most-amplified growth between experiment and LPSE. Possible sources of the disagreement are discussed, and the effect of small misalignments of the model is quantified experimentally.

A focused schlieren deflectometer with high bandwidth (1 MHz) and high signal-to-noise ratio is employed to complement the hot-wire work. The second-mode fundamental at 250 kHz is observed, as well as additional harmonic content not discernible in the hot-wire measurements at two and three times the fundamental. A bispectral analysis shows that after sufficient amplification of the second mode, several nonlinear mechanisms become significant, including ones involving the third harmonic, which have not hitherto been reported in the literature.

For my wife.

ACKNOWLEDGEMENTS

First, I should like to thank my committee chair and mentor, Dr. William Saric. I will be forever grateful for the generosity and trust he has shown me both professionally and personally. As his student, I have been afforded an incredible set of diverse opportunities, from participating in unique flight experiments, to architecting a cryogenic wind tunnel test overseas, to the awesome task of reconstructing an entire hypersonic wind-tunnel system and its infrastructure, characterizing it, and conducting exciting experiments therein. It is by his distinguished example and under his advisement that I have become a better scientist, a skilled experimentalist, and a deliberate, critical thinker.

Next, I should like to thank Dr. Bowersox for his frequent direct involvement in and guidance with this work, from the earliest phases of infrastructure construction and tunnel establishment through to the details of my experimental diagnostics. I also thank the remaining members of my committee – Dr. Daripa, Dr. Reed, and Dr. White – for their continued guidance and support throughout my work.

Thanks are due also to my fellow students & researchers, principally Michael Semper, with whom I was fortunate to share the experience of building a laboratory, and without whom it would not have been possible. Alex Craig, Ray Humble, Chi Mai, Brandon Pruski, Nicole Sharp, and numerous others at the Easterwood laboratories are gratefully acknowledged for their ongoing assistance and discussions regarding the tunnel infrastructure, laboratory operations, experimental diagnostics, and analysis.

Dr. Reed and her computational team – Eddie Perez, Joe Kuehl, and Travis Kocian – deserve special thanks for their efforts in providing the stability computations for comparison with my experiments. I have valued and learned much from our close collaboration; it has been exciting to be a part of the first generation of a combined experimental/computational hypersonic stability effort at Texas A&M.

The Air Force Office of Scientific Research (AFOSR) is acknowledged for the funding to reestablish the Mach 6 Quiet Tunnel (Grant #FA9550-08-1-0308), and both NASA and AFOSR are gratefully acknowledged for ongoing support through the *National Center for Hypersonic Laminar-Turbulent Transition Research* (Grant #FA9550-09-1-0341).

The *NASA/ASEE Aeronautics Scholarship* is gratefully acknowledged for supporting a portion of my work, and also for the valuable opportunity it provided in a summer internship with the quiet-tunnel team of the *Flow Physics and Control Branch* at NASA Langley during the summer of 2010. I'd like to thank the members of this team – principally Steve Wilkinson, Michael Kegerise, Rudy King, and Lewis Owens – for their insight into quiet-tunnel operation, diagnostics, and techniques. Mr. Kegerise was especially helpful with regards to hot-wire probe fabrication and operation, and Mr. Wilkinson has been an invaluable resource throughout our work in the quiet tunnel, regarding everything from its reconstruction, to repolishing, operational procedures, and the details of ongoing experiments. In many ways, I've regarded Steve as a second advisor, and have valued his input greatly.

For their diverse support throughout this work, from fabrication to infrastructure maintenance and operational safety, I thank the staff of the Oran W. Nicks Low Speed Wind Tunnel. For his help with maintaining the tunnel infrastructure and as a mentor for all things mechanical, I'd like to thank Cecil Rhodes.

The incredible administrative wizardry and friendship of Ms. Colleen Leatherman needs to be acknowledged. I am very grateful for her support over these years.

I must thank my family at home in Arizona – my father Dan, mother Kathi, brother Aaren, and sister Ciara – all of whom I love and have missed dearly during this extended time spent busily and far away.

Finally, and above all, I am deeply and forever grateful for the love and companionship of my wife Jacqueline – I love you dearly. Without your encouragement, strength, and sacrifice, this would not have been possible.

NOMENCLATURE

Acronyms

ACE	Adaptively Controlled Expansion Mach 5–7 Tunnel (TAMU)
AEDC	Arnold Engineering Development Center
AFOSR	Air Force Office of Scientific Research
BAM6QT	Boeing/AFOSR Mach 6 Quiet Tunnel (Purdue University)
BVC	Bleed valves closed ("noisy" mode)
BVO	Bleed valves open ("quiet" mode)
CCD	Charge-coupled device (imaging sensor)
CCA	Constant-current anemometry
CTA	Constant-temperature anemometry
CVA	Constant-voltage anemometry
DAQ	Data acquisition
DNS	Direct numerical simulation
EMI	Electromagnetic interference
FSD	Focused schlieren deflectometry
GASP	General Aerodynamic Simulation Program
HSLDT	High-Speed Low Disturbance Tunnel (NASA Langley)
LED	Light-emitting diode
LST	Linear stability theory
M3.5QT	Mach 3.5 Quiet Tunnel (NASA Langley), aka SLDT

M6NTC	Advanced Mach 6 Pilot Quiet Nozzle in the Nozzle Test Chamber (NASA Langley)
M6QT	Mach 6 Quiet Tunnel (Texas A&M); formerly M6NTC
M8VDT	Mach 8 Variable Density Tunnel (NASA Langley)
M18QHT	Mach 18 Quiet Helium Tunnel (NASA Langley)
MKS	MKS Instruments, Inc.
NAL	National Aerothermochemistry Laboratory
NASA	National Air and Space Administration
NASP	National Aerospace Plane
NI	National Instruments Corporation
[N/L]PSE	[Linear/Nonlinear] Parabolized stability equations
PCB	PCB Piezotronics, Inc.
RMS	Root mean square
SCFM	Standard cubic feet per minute
SLDT	Supersonic Low Disturbance Tunnel, aka M3.5QT
SNR	Signal-to-noise ratio
TAMU	Texas A&M University
TPS	Thermal protection systems
UAH	University of Alabama, Huntsville
UCLA	University of California, Los Angeles
VI	Virtual Instrument (an NI LabVIEW program)

Variables

A	Aperture diameter of focused-schlieren lens
DS	Depth of sharp focus for focused schlieren system
DU	Depth of unsharp focus for focused schlieren system
d	Hot-wire element diameter
f	Focal length of focused-schlieren lens
f_0	Frequency of most-amplified second-mode waves (also 'fundamental' or 'first harmonic')
f_1, f_2	Frequency variables in bispectrum/bicoherence analyses
L	(1) Nozzle length, from throat = 1.01 m
	(2) Focused schlieren: distance from lens to source grid
L'	Focused schlieren: distance from lens to cutoff grid
l	(1) Hot-wire element length
	(2) Focused schlieren: distance from lens to object plane
l'	Focused schlieren: distance from lens to image plane
M	Mach number
N	N-factor (e^N = integrated growth amplitude ratio)
Nu	Nusselt number
p_{t1}	Tunnel stagnation pressure
p_{t2}	Pitot pressure ($\bar{p}_{t2}$ = mean, $\tilde{p}_{t2}$ = RMS)
Pr	Prandtl number
R	Cone Reynolds number = $\sqrt{Re_S}$

R_{20}	Ambient-temperature resistance of hot-wire sensor element
r	Radial (transverse) coordinate in nozzle, from centerline
Re	Freestream unit Reynolds number = $\rho_\infty U_\infty/\mu_\infty$
Re_d	Hot-wire Reynolds number, based on d and properties behind probe shock
Re_S	Reynolds number based on cone arc distance = $\rho_\infty U_\infty S/\mu_\infty$
$Re_{S,tr}$	Reynolds number at transition onset, based on cone arc distance
r_{exit}	Nozzle radius at exit = 95.1 mm
S	Distance along flared cone surface, from sharp tip
T_∞	Freestream static temperature
T_e	Hot-wire recovery temperature = ηT_t
T_t	Total temperature
T_{t1}	Tunnel stagnation temperature
T_w	Hot-wire operating temperature
U_∞	Freestream velocity
X	Distance along nozzle axis, from throat
X_0	Centerline axial location of last nozzle characteristic (onset of uniform flow), from throat
X_c	Distance along flared cone model axis, from sharp tip
$X_{T,C}$	Axial location of nozzle-centerline freestream noise impingement, from throat
$X_{T,W}$	Axial location of transition on the nozzle wall, from throat

w	Focused schlieren: resolution limit due to grids and magnification
δ	Boundary-layer thickness
ΔX	Length of nozzle quiet core on centerline = $X_{T,C} - X_0$
η	Hot-wire recovery factor ≡ T_e/T_t
λ	Wavelength
μ_∞	Freestream absolute viscosity (via Sutherland's Law)
ρ	Density
ρ_∞	Freestream density
τ	Hot-wire temperature loading factor = $(T_w - T_e) / T_t$

TABLE OF CONTENTS

LIST OF FIGURES

LIST OF TABLES

1. INTRODUCTION

1.1. Background and motivation

Laminar-turbulent boundary-layer transition has a profound effect on the design and performance of hypersonic flight vehicles. As is true for subsonic transport vehicles, transition to turbulence for high speed vehicles leads to substantially increased vehicle skin friction drag and loss of efficiency (Reed *et al.* 1997) versus the laminar case. However, at high speeds, this effect of increased skin friction is amplified and manifests itself more importantly as heat, with high turbulent heating rates driving the design of heavy, complicated thermal protection systems (TPS). Additionally, asymmetric transition can have adverse implications on vehicle flight dynamics and aerostability, cause increased lateral trim loads, or decreased accuracy of ballistic trajectories and larger impact zones (Lin 2008).

Despite its importance on vehicle design, the hypersonic transition process remains incompletely understood, and techniques for predicting boundary-layer transition location remain primitive. Simple empirical correlations are commonly employed by designers, and their large uncertainty leads to the conservative over-design of vehicle TPS, increasing weight and reducing efficiency and/or payload.

As an example, a common criterion used in design is one in which transition is estimated to occur when the momentum-thickness Reynolds number, Re_θ, divided by the edge Mach number, M_e, reaches a particular constant value. Reshotko (2007) shows that this correlation effectively ignores instability mechanisms and important physical

parameters such as surface roughness, surface temperature, and pressure gradient, and even gives incorrect Mach number trends. The correlation is only very narrowly applicable to re-entry vehicles, and even then only for approximating an altitude at which transition may occur, not for predicting a transition location on the body. Other common correlations – tabulated by Lin (2008) – are similarly limited.

To reduce uncertainty in predictive techniques, one must instead use an approach that is based more fundamentally upon the physical mechanisms which lead to transition. On a very basic level, the laminar boundary layer acts as a selective-passband amplifier; tiny disturbances in the upstream flowfield enter the boundary layer, undergo tremendous growth, interact, and eventually cause the boundary layer to break down into turbulence as the energy is redistributed to a broad band of flow scales.

This process is depicted in further detail in the classic transition roadmap presented as Figure 1–1, adapted from Morkovin (1969) and Morkovin *et al.* (1994). Disturbances external to the boundary layer – whether freestream sound or vorticity, temperature spots, interactions with surface roughness, or otherwise – enter the boundary layer and establish the initial amplitudes and scales of an instability through the process of 'receptivity' (Saric *et al.* 2002). Depending on the initial amplitude of the resulting disturbances, any of a number of pathways (listed as A–E in the diagram) may be selected. In path A, the disturbances undergo modal (linear, exponential) growth until they reach such an amplitude that they undergo nonlinear interactions, excite secondary mechanisms, or otherwise cause breakdown to turbulence. Alternatively, disturbances may grow in an algebraic (non-modal) fashion through the process of transient growth,

and either subsequently excite primary modes (path B), secondary instabilities (path C), or lead directly to bypass transition (path D). If initial disturbances are sufficiently large (path E), such as those caused by a large isolated roughness, the transition to turbulence may be abrupt, bypassing the classical mechanisms for initial instability growth.

Both the process of receptivity and these mechanisms by which instabilities can grow can be modified or selected based on flight parameters (e.g. Mach number, unit Reynolds number, *Re*, angle of attack), vehicle geometry (e.g. bluntness, pressure gradients), and other physical processes (e.g. high-enthalpy effects, chemical reactions). The effects of these many parameters must be understood.

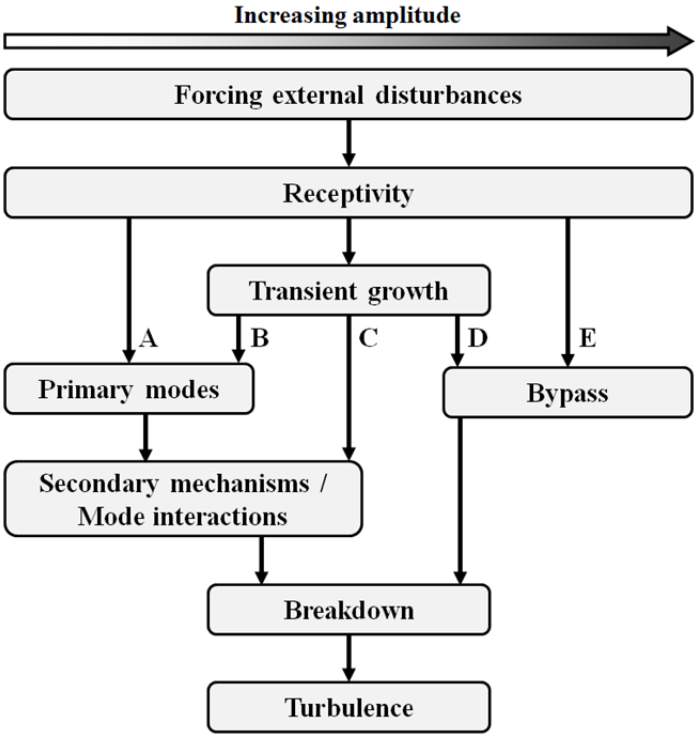

Figure 1–1. Roadmap for the process of transition to turbulence in boundary layers. Simplified from Morkovin (1969) and Morkovin *et al.* (1994) via Saric *et al.* (2002).

Due to the complex nature of the processes and mechanisms involved in instability growth and boundary-layer transition, the state of the art in predictive and control techniques can only be advanced through a rigorous, physics-based approach which integrates theoretical, computational, and experimental efforts – and one which intelligently decomposes the vast parameter space into manageable areas of fundamental study.

It is under this motivation and in support of this approach that the National Center for Hypersonic Laminar-Turbulent Transition Research (hereafter the Center) was established by NASA and the Air Force Office of Scientific Research (AFOSR) in early 2009 as a five-year program. The work of the Center is summarized by Saric (2012). The effort integrates the theoretical, computational, and experimental work of 13 PIs from Texas A&M University (TAMU), the University of Arizona, the California Institute of Technology (Caltech), and the University of California, Los Angeles (UCLA) into a common framework shown in Figure 1–2. The figure depicts on a notional hypersonic cone the key stages of the transition process, from receptivity to linear and nonlinear growth, mode interactions, and finally breakdown to turbulence. Listed below the cone as areas of study are the parameters and physical processes which are known to affect the transition process. Listed above it are the personnel, experimental facilities, and computational tools employed in the study of each stage of the process. The overlapping regions of processes, techniques and personnel shown in the roadmap depict the many critical opportunities for close collaboration that will

ultimately lead to a more-complete physics-based understanding of the hypersonic transition problem.

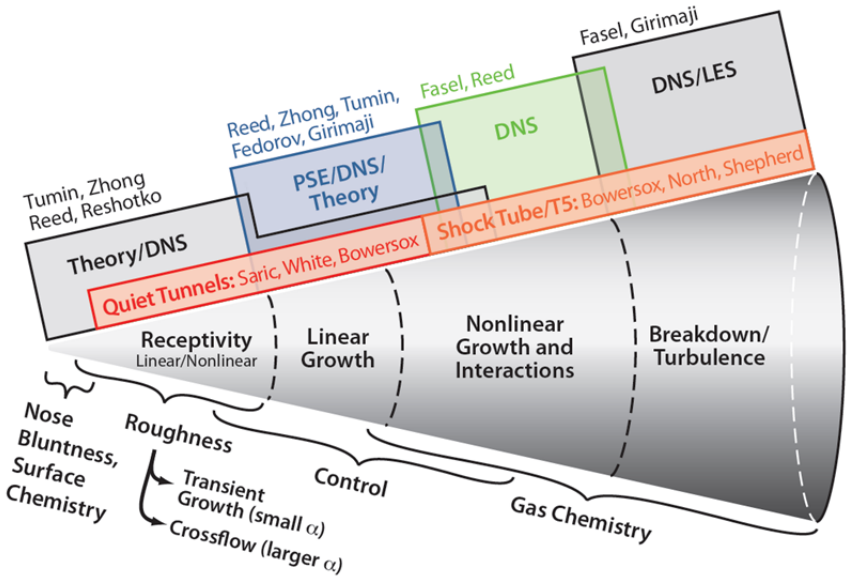

Figure 1–2. Overview of hypersonic transition processes and approaches for study. Roadmap for research & collaboration through the NASA/AFOSR National Center for Hypersonic Laminar-Turbulent Transition Research.

As a critical experimental component of the Center activities, a low-disturbance Mach 6 wind tunnel originally designed, built, and operated at NASA Langley Research Center is reconstructed at TAMU. The facility will ultimately serve as an experimental platform for guiding and providing validation data for the development of stability computations, identifying and characterizing the mechanisms and interactions responsible for instability growth, interactions, and breakdown to transition, and for demonstrating control technologies.

This dissertation describes the reconstruction and characterization of this facility, as well as a series of experiments conducted therein for the study of the second-mode instability on a sharp-tipped, flared, 5º half-angle cone. This geometry is chosen as a fundamental analog of hypersonic flight vehicles that emphasizes the second-mode instablity, and for which computations are relatively straight-forward. Growth of the instability in the linear and early nonlinear regimes is explored, and comparisons are made to predictions based upon linear stability theory (LST) and parabolized stability equations (PSE). Additional work with later-stage nonlinear interactions and breakdown is proposed, motivated and supported by recent direct numerical simulations (DNS) performed as a part of the Center activities.

1.2. Compressible instability and the acoustic modes

To provide the necessary background and context for the stability experiments performed, this section briefly discusses the basic aspects of compressible boundary-layer stability as it differs from the incompressible case. A complete description of both incompressible and compressible boundary-layer stability theory is provided by Mack (1984), and a concise introduction is provided by Reed *et al.* (1996).

A linear stability analysis of supersonic boundary layers reveals three notable differences versus the incompressible case. The first is an extension of the Rayleigh inflection point criterion, whereby a sufficient condition for the existence of an instability is that

$$D\left(\rho DU\right) = 0, \quad \text{at } y = y_s > y_0 \tag{1.1}$$

where the nondimensionalized velocity $U(y_0) = 1 - 1/M_e$, and M_e is the edge Mach number. The consequence of this *generalized inflection point* is that, because a compressible, adiabatic flat plate boundary layer always has $D(\rho DU) = 0$ somewhere in the flow, even zero-pressure gradient flows are subject to inviscid instabilities.

The second key difference is that, above Mach 1, the 3-D (or oblique) waves of the first viscous mode have higher amplification rates than the 2-D (or streamwise) waves, and so the assumption of 2-D waves cannot be applied.

The third – and most relevant to the present work – is the presence of an additional family of solutions to the disturbance equations. The inviscid stability equations for compressible flow can be written in the form

$$\frac{\partial^2 \psi}{\partial y^2} + \left(1 - \hat{M}^2\right)\frac{\partial^2 \psi}{\partial x^2} + f\left(\hat{M}, \psi, \frac{\partial \psi}{\partial y}\right) = 0, \tag{1.2}$$

where ψ is the nondimensionalized disturbance amplitude, y is the wall-normal coordinate, and $\hat{M}(y)$ is the relative Mach number between the local basic-state velocity and the disturbance phase speed. When $\hat{M} < 1$, the equation is elliptic, and solutions are exponentials as for the low-speed case. When $\hat{M} > 1$, however, the equation is hyperbolic and a set of oscillatory solutions are permitted. These solutions are called the Mack modes, or the acoustic modes. Physically, they represent trapped acoustic waves which reflect between the wall and a height near the point, $y = y_a$, where the relative disturbance Mach number $\hat{M} = 1$. In this sense, the boundary layer acts as an acoustic waveguide (Fedorov 2011). This is depicted in Figure 1–3.

Parziale *et al.* (2012) alternatively describe the acoustic mode in a more direct physical sense, explicitly demonstrating the concept of trapped acoustic waves by conducting ray-tracing computations within the velocity and sound-speed gradients of typical supersonic and hypervelocity boundary layers.

The first of these acoustic modes (lowest in wavenumber) is commonly referred to as Mack's 'second-mode', or simply the second mode instability, and this nomenclature will be utilized throughout this work, although more a mathematically-consistent terminology has been proposed (Fedorov and Tumin 2011).

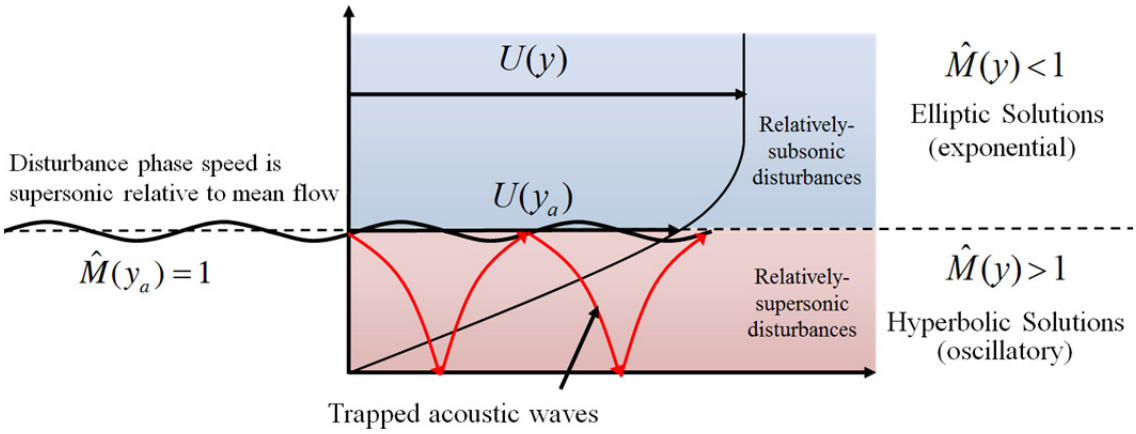

Figure 1–3. The acoustic-mode instability in a hypersonic boundary layer.

It is instructive to list several of the basic properties of the second mode instability. It is an inviscid, streamwise (2-D) phenomenon, and although it first appears on an adiabatic flat plate near M = 2.2, it becomes the dominant instability as M > 4. It tends to be the dominant instability on sharp, smooth bodies in this Mach number range,

such as the cone model used for the present experiments. The cone has a flared contour (see Section 3.1) to introduce an adverse pressure gradient, as this is destabilizing to the second mode. Finally, the second mode instability is highly-tuned to the boundary-layer thickness as $\lambda \approx 2\delta$, where λ is the wavelength and δ is the boundary-layer thickness. Because boundary-layer thickness can be quite small (for the present work), second-mode frequencies are high – several hundred kilohertz to several megahertz for typical experiments. For the present work, $\delta \approx 1.5$ mm, and the resulting second-mode frequencies are 200–300 kHz.

1.3. Experiments and the need for low-disturbance wind tunnels

The second mode instability has been observed and measured in a variety of wind tunnel experiments: Kendall (1975) studied a sharp 4º cone at Mach 8.5; Demetriades (1974) studied a 5º half-angle cone at Mach 8.0; and Stetson *et al.* (1983) studied a 7º cone at Mach 8.0. These experiments provided valuable insight, and instability growth was seen to agree well with linear stability theory. However, these experiments and others of the time were conducted in conventional wind tunnels, where pressure disturbances originating on a turbulent nozzle wall boundary layer radiate along Mach waves into the test region (Laufer 1961, Morkovin 1959). These disturbances produce a freestream environment with disturbances an order of magnitude higher than those observed in flight. They are then able to enter the boundary layer through receptivity, and modify the process of instability growth and transition, as reviewed by Schneider (2001). Transition may occur earlier, or due to entirely different mechanisms,

so extreme care must be taken in the interpretation of results obtained in quiet tunnels for application to flight.

The acoustic disturbances can arise in a stationary fashion, where Mach waves present at fixed locations due to defects on the nozzle wall ‘shimmer’ as turbulence passes through them, or as convecting acoustic disturbances that follow the turbulent eddies in the boundary layer, due to the expanding flow effectively seeing the turbulent boundary layer as a rough wall.

This phenomenon is visible in a shadowgraph image in Figure 1–4, taken from a ballistic range test. The sharp cone is traveling through still air at Mach 4.31. The lower surface is turbulent, and acoustic disturbances emanating from the wall along Mach lines are clearly visible. The upper surface is nominally laminar. Above the laminar region, no disturbances are visible, although above isolated turbulent spots, both strong, isolated waves and patches of lower-level acoustic radiation are visible.

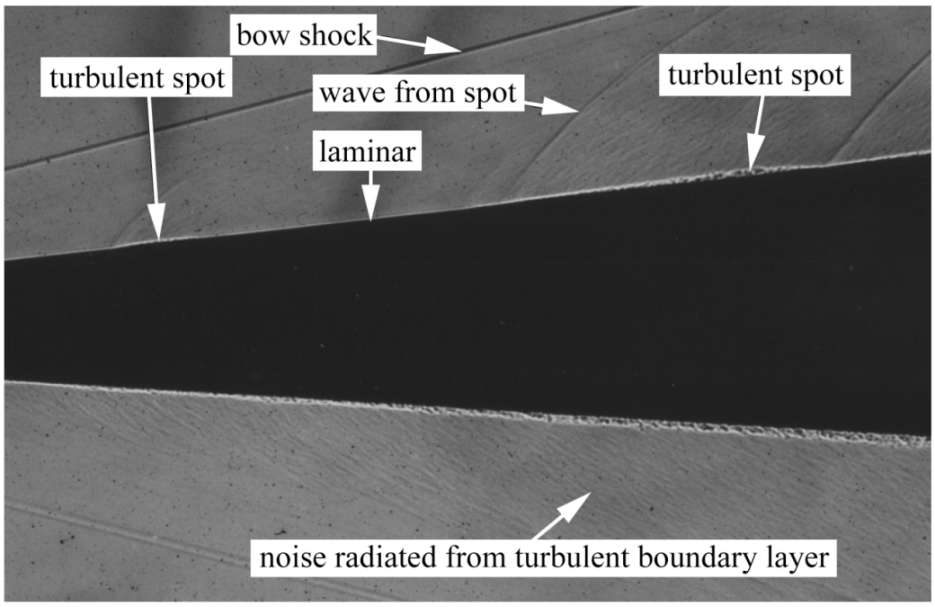

Figure 1–4. Acoustic radiation visible in shadowgraph of sharp cone transition. Mach number is 4.31; flow is left to right. Photograph adapted from Schneider (2008). Experiment described in Reda (1979).

The effect is known to dominate noise in typical wind tunnel facilities for $M > 2.5$ (Pate and Schueler 1969; Pate 1971, 1978). Other disturbances may originate upstream (as temperature spottiness, vorticity, or sound), but as Mach number increases, the high expansion ratios stretch these scales out and minimize their significance versus the strengthening Mach-wave acoustic radiation from the nozzle boundary layer. Typical disturbance levels are in the range of 1–3% in root-mean-square (RMS) Pitot pressure.

Figure 1–5(*a*) depicts a typical, rapid-expansion wind tunnel nozzle. At a typical operating unit Reynolds number, transition on the nozzle wall occurs very early, and the majority of the test environment is under the influence of acoustic waves.

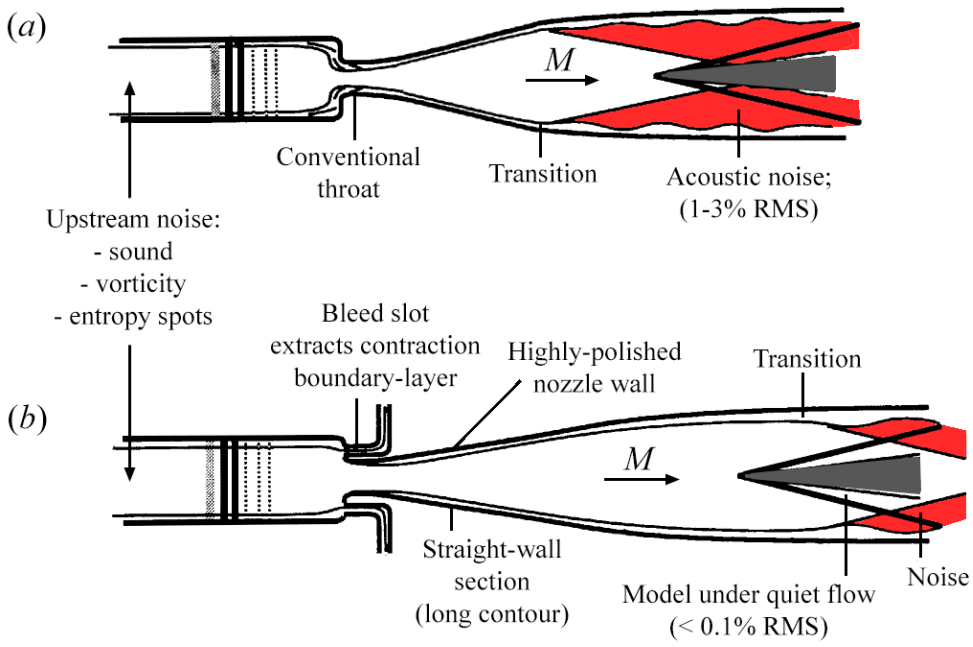

Figure 1–5. Schematics of (*a*) conventional and (*b*) quiet supersonic wind tunnels. Quiet tunnels achieve low-disturbance freestream environments at high unit Reynolds number through the application of several laminar flow control techniques. Figure adapted from Lachowicz (1995).

Through an extensive facilities research program in the 1970s–1990s (detailed further in Section 2.1.1), NASA Langley Research Center developed a set of design principles which enable low-disturbance ground test facilities, or "quiet tunnels," at Reynolds numbers suitable for stability experiments. The basic principle is to mitigate the acoustic waves radiated by a turbulent boundary layer by maximizing the laminar extent of the nozzle-wall boundary layer. After much research, success was achieved with a design as depicted by Figure 1–5(*b*). A bleed slot is employed upstream of the nozzle throat for the extraction of the contraction-wall boundary layer, thus initiating a new laminar boundary layer on the nozzle wall. In order to maintain the laminarity, the nozzle wall is highly polished, minimizing surface roughness effects. In addition, the

nozzle contour is designed as a long-expansion contour, delaying the onset of the instability which leads to transition. With transition on the nozzle wall delayed substantially further downstream than for conventional facilities, a region of uniform Mach number, low-disturbance flow is created – often referred to as the quiet test core. In this region, pressure disturbances measured with a fast-response Pitot probe are remarkably lower (< 0.1% RMS of the mean, versus 1–3% for conventional facilities).

A number of facilities were developed using this strategy, one of which was the Advanced Mach 6 Pilot Quiet Nozzle in the Nozzle Test Chamber (M6NTC). The M6NTC is an axisymmetric nozzle 1 m in length with a 190 mm exit diameter, and operated at NASA Langley with quiet flow to at least $Re = 10\times10^6$ m^{-1}.

After much development and iteration of the facility itself to achieve this level of performance reliably, Lachowicz (1995) and Lachowicz *et al.* (1996) studied a sharp-tipped, 5º half-angle cone with a circular-arc flare to generate an adverse pressure gradient and thereby increase the second-mode amplitudes within the limited spatial extent of the low-disturbance area. The cone was operated at a nominally zero angle of attack, with transition location monitored by embedded thermocouples and boundary-layer profiles of mass flux and total temperature observed using a constant-voltage anemometer. Acoustic-mode instabilities were observed on the cone between frequencies of 210 and 290 kHz, and growth rates were measured and compared with computation. Also studied in this work was the effects of small bluntness, although with very small increases in nose radius, the second-mode growth rates were substantially reduced and the model remained laminar.

Doggett (1996) then studied the same cone at 2º and 4º angle of attack. The second mode was observed to be destabilized (with maximum growth at lower frequencies) on the leeward side of the model, and stabilized (at higher frequencies) on the windward ray of the model. These findings were consistent with expectation based on the expected scaling of the second-mode frequency with boundary-layer thickness, and with previous studies (Stetson *et al.* 1983) in conventional tunnels. In the transitional region on the leeward side, nonlinear growth and harmonics were observed.

Blanchard and Selby (1996) finally used a similar cone geometry equipped with an actively-cooled wall to study wall-temperature effects and observe higher levels of second-mode growth.

A concise review of all of these experiments is provided by Wilkinson (1997), and Chokani (2001) provides a review in the context of the accompanying computations and nonlinear analyses. Although brief, the Langley experimental series was valuable both specifically for the observations and computational comparisons they provided, and in a general sense for what they represented – the first hypersonic stability experiments performed in a low-disturbance wind tunnel at Reynolds numbers sufficient to see substantial instability growth. Unfortunately, at the conclusion of this test series, the M6NTC was decommissioned due to declining funding levels, and was put into storage.

Around this time, design and preparation for the construction of a new quiet hypersonic facility at Purdue University was well underway (Schneider 2008). Developed as a Ludwieg tube design, the Boeing/AFOSR Mach 6 Quiet Tunnel (BAM6QT) operates with run-times of a few seconds. While this design precludes the

acquisition of boundary-layer profiles at constant conditions in a single run, the facility has been productive in a diverse array of stability and transition studies. Since achieving reliable high-Reynolds number quiet flow in 2006, Purdue researchers have explored the second-mode instability via high-frequency surface pressure measurements (Berridge 2010), wake instabilities of isolated roughness elements (Wheaton and Schneider 2012), the crossflow instability (Berridge *et al.* 2010), and much more. Extensive optical access to the model is available, enabling the use of temperature-sensitive paints for transition detection and identification of flow structures.

In 2005, after years of dormant storage, the key components of the Langley Mach 6 quiet tunnel – the nozzle, settling chamber, and particle filter – and the flared cone test article of Lachowicz and Doggett were moved to Texas A&M University, where it was to be reactivated with a run-time suitable for detailed studies of the instabilies via the acquisition of boundary-layer profiles. In this way, the Texas A&M and Purdue facilities serve complementary roles, with each offering unique advantages.

The work performed for this dissertation begins with this reactivation of the facility and continues with its renewed application to the study of hypersonic boundary-layer instability and transition. Additional discussion on the development of quiet tunnels and what is now known as the Mach 6 Quiet Tunnel (M6QT) at Texas A&M is given in Section 2.1.

1.4. Experimental objectives

In consideration of the motivation and background provided above, and in support of the collaborative, physics-based fundamental approach chosen by the Center, the work performed for this dissertation re-establishes a long-duration, low-disturbance ground test capability and employs it in the study of the second-mode instability with computational support. On a basic level, the work as a whole restores to the hypersonic transition community an experimental capability lost when the NASA Langley M6NTC was decommissioned, and employs it in a new series of experiments which reproduce and build upon the earlier work conducted the in tunnel at NASA Langley.

The three major components of the effort are described in detail below.

1.4.1. Restoration and characterization of the M6QT at Texas A&M

At the onset of this work, no hypersonic, low-disturbance ground test facility with constant-condition run-times of sufficiently long duration for the acquisition of well-resolved code-validation data existed in operational status. Necessarily, then, the first step in the process was to restore to experimental readiness the decommissioned NASA Langley Mach 6 low-disturbance facility. The facility is integrated into a new pressure-vacuum blowdown infrastructure at Texas A&M, together with all necessary controls and instrumentation, and the freestream quiet flow performance is comprehensively characterized in order to qualify it for use in the stability experiments that follow.

The history and design of the M6QT are described in detail in Section 2, as are details of the new supporting infrastructure and capabilities at Texas A&M. Experimental setup and diagnostic techniques are described in Sections 3 and 4, respectively, and the characterization of the tunnel freestream is presented in Section 5.

1.4.2. Second-mode instability measurements as code-validation data

With the facility established and characterized, the second key objective of the work was the study of the development of the second-mode instability for comparison with PSE simulations. This stage of the work focuses on the acquisition of well-resolved boundary-layer profiles on the NASA Langley 93–10 flared cone model previously studied by Lachowicz (1995), Doggett (1996), and Horvath *et al.* (2002). Hot-wire anemometry is used as the primary diagnostic, with a bandwidth of several hundred kilohertz. The second mode instability is observed and compared with prediction, and, to provide context for the comparison, the sensitivity of the most-unstable frequency to model incidence is experimentally determined. By reproducing and expanding upon earlier experiments (in addition to making comparisons to modern computations), the performance of the newly-reestablished facility is further proven suitable for the work. These results of this objective are presented in Section 6.

1.4.3. Investigation of nonlinear interactions using optical diagnostics

The third and final component of the work complements the hot-wire studies through the use of a focused schlieren deflectometer – an optical diagnostic with an

O(1 MHz) bandwidth and high signal-to-noise ratio. The work reveals the presence of early nonlinear interactions of the second mode in the cone boundary layer, with harmonics of the instability observed at two and three times the fundamental frequency. A nonlinear analysis of the time series data is conducted using bispectral techniques, which, by identifying a strong degree of phase coupling between the harmonics and the fundamental, confirms their self-excited nature. Several nonlinear interactions not seen in the original hot-wire studies conducted at NASA Langley are now observed. Results are presented in Section 7.

The confirmation of the presence of nonlinear interactions on the model at the test conditions in the M6QT additionally sets the stage for the next generation of experiments on the flared cone. Preparations were made for an additional campaign to investigate the spanwise-periodic flow structures which develop on the cone as a result of the nonlinear interaction between the two-dimensional second-mode and oblique modes (Sivasubramanian & Fasel 2012a, 2012b). An azimuthal probe-traversing axis was designed, constructed, and tested, although this work was not completed for discussion in this dissertation. The mechanism itself – which additionally lays the groundwork for more future studies regarding transient growth and the crossflow instability – will be briefly discussed in Section 3.2.4, and details of the planned investigation of nonlinear breakdown structures will be briefly discussed in Section 9 as future work.

2. TEST FACILITY

2.1. Texas A&M Mach 6 Quiet Tunnel

The facility used for this work, the Texas A&M Mach 6 Quiet Tunnel (M6QT), was originally fabricated and assembled during an extensive facilities research program at NASA Langley which began in the late 1960s and lasted through the mid-1990s. This program was responsible for the establishment of a set of design methodologies which led to the creation of several supersonic and hypersonic ground-test facilities with freestream disturbance levels suitably low for the study of boundary-layer stability and transition.

At NASA Langley, the M6QT facility – there known as the Advanced Mach 6 Pilot Quiet Nozzle in the Nozzle Test Chamber (M6NTC) – was utilized for a brief series of stability and transition experiments in the early and mid-1990s, and was subsequently put into storage until the nozzle and settling chamber were moved to Texas A&M in 2005. A major component of the work performed for this dissertation was then necessarily the complete refurbishment and reestablishment of the facility within a brand-new laboratory infrastructure. Save for the major components received from NASA Langley, everything necessary for the operation of the tunnel – an all-new test section, piping, pressure regulators, heaters, instrumentation, data acquisition hardware and software, diagnostic techniques, and associated procedures – was selected, designed, constructed, and/or otherwise implemented by the author and collaborators for this first generation of studies in the laboratory's hypersonic blow-down tunnels. As such,

substantial discussion is given here to the facility itself, supporting equipment, and operating procedures. Discussion begins below with detail on the history and unique design features of the M6QT nozzle, and proceeds to the specifics of the tunnel apparatus and supporting infrastructure.

2.1.1. Quiet-tunnel design concepts and facility history

As was discussed in the introduction, conventional supersonic and hypersonic ground test facilities, operated at sufficient Reynolds numbers, exhibit high levels of acoustic noise in the freestream. This noise originates from turbulent nozzle-wall boundary layers, where turbulent structures effectively appear to the expanding flow as a rough wall, creating pressure disturbances in the form of weak expansions and compressions which radiate into the test environment along Mach lines. This noise is present at amplitudes and length scales that are not present in the flight environment, and as such have the potential to enter the boundary layer through receptivity, grow, and alter the mechanisms which may have otherwise naturally led to transition on test articles in flight. In this sense, conventional facilities are often ill-suited to the study of boundary-layer stability and transition. As a consequence, data between facilities differed even though the model and test conditions were identical. Much of the work in the ‘60s and ‘70s are thusly suspect.

It is with this motivation that an extensive sustained effort was undertaken at NASA Langley Research Center to develop low-disturbance, or “quiet,” ground test facilities in the supersonic and hypersonic regimes. The effort was led primarily by Ivan

Beckwith, and lasted from the late 1960s through the mid-1990s. An excellent, extensively-referenced review of the program is presented by Schneider (2008), with additional detail by Wilkinson *et al.* (1994). Only a brief summary of the program and its quiet-tunnel design concepts is provided here.

As the overall guiding principle of the quiet-tunnel program, it was known that a successful quiet tunnel design must do each of the following: provide a clean, dry air supply; minimize upstream flow disturbances; and initiate and maintain a laminar boundary layer on the nozzle wall. Of these, the last is the most difficult and the most crucial.

Early attempts applied suction to porous nozzle walls (Beckwith *et al.* 1973), but difficulties with surface roughness and nonuniform suction yielded poor results. Subsequent designs (Beckwith 1975) achieved better performance with a suction slot upstream of the throat, through which the contraction-wall boundary layer was removed. Initial pilot nozzles used a rapid-expansion contour in an attempt to stabilize the boundary layer with a strong favorable pressure gradient. Anders *et al.* (1977) discuss extensive testing on various nozzles of this design and settling chamber configurations. Two rapid-expansion Mach 5 axisymmetric nozzles with bleed slots were used: one machined conventionally, and one manufactured via a highly-accurate electroforming process and highly polished. With its accurate, low-roughness, low-waviness construction, the electroformed nozzle was seen to provide substantially more laminar flow and substantially lower noise levels, regardless of the specifics of the settling chamber flow conditioning.

Once it became clear that the curvature-induced Görtler instability (Saric 1994) was the dominant mechanism in the transition on nozzle walls, one additional key improvement to the design was made. Here, a straight-wall (radial flow) section downstream of the throat was imposed on the nozzle contour, lengthening the nozzle by delaying the onset and amplification of the Görtler instability (Beckwith *et al.* 1988).

Indeed, the design concept of a highly-polished, long-expansion nozzle with a bleed slot upstream of the throat has served as the guiding principle for all quiet-tunnel designs since.

As the program progressed and with strong interest and funding through the National Aerospace Plane (NASP) program, five key facilities were developed for high-Reynolds number, low-disturbance operation. These include: the Supersonic Low Disturbance Tunnel (SLDT), operating at Mach 3.5 with both 2D and axisymmetric nozzles; the Mach 6 Quiet Nozzle in the Nozzle Test Chamber (M6NTC); the Mach 18 Quiet Helium Tunnel (M18QHT); the Mach 8 Variable Density Tunnel (M8VDT); and the larger High-Speed Low Disturbance Tunnel (HSLDT). All of these but the HSLDT were built and tested.

Additionally, Dr. Steven Schneider – under the advisement of Ivan Beckwith and the NASA Langley group – began an effort at Purdue University in 1990 to produce a low-cost quiet tunnel by applying the Langley nozzle design methodologies in a Ludwieg-tube infrastructure (Schneider 1998). Work began with a small pilot Mach 4 tunnel, and evolved in the late 1990s to include a Mach 6 nozzle with a longer expansion and slightly larger diameter than the M6NTC. After extensive research and iteration, this

tunnel – the Purdue Boeing/AFOSR Mach 6 Quiet Tunnel (BAM6QT) – has been operating with reliable quiet flow at or above $Re = 10\times10^6$ m^{-1} since late 2006, and remains a valuable and productive resource to the hypersonic stability and transition community. The Ludwieg tube design produces an overall run-time of ≈ 7 seconds, with a stair-step variation of freestream unit Reynolds number as expansion waves reflect in the tube; constant-condition duration between each expansion is ≈ 90 milliseconds. The design and development of the BAM6QT are summarized by Schneider (2007), a flow-quality characterization is given by Steen (2010), and the latest research activity is summarized by Abney *et al.* (2013).

Of the NASA Langley facilities, only those operating at Mach 3.5 and 6 were ever successfully employed in stability and transition experiments. The earlier Mach 5 pilot nozzles, being of the early rapid expansion design, had too short a quiet test core to be useful, and the Mach 8 and 18 facilities encountered unexpected design issues and never produced useful amounts of quiet flow by the end of their programs.

The M6NTC was used in the early and mid-1990s for the three experimental campaigns discussed in Section 1 (Lachowicz 1995; Doggett 1996; and Blanchard and Selby 1996), but due to changing facility priorities and a sharp decline in funding with the termination of the NASP program, the M6NTC was decommissioned and put into storage. In 2005, it was relocated to Texas A&M, along with its settling chamber, particle filter, and the two rapid-expansion Mach 5 pilot nozzles. For the present work, this facility has been reestablished as the Mach 6 Quiet Tunnel, characterized, and implemented in a new set of stability and transition experiments.

The M6QT now operates with a nominal run time of 40 seconds at constant conditions, which enables the acquisition of well-resolved boundary-layer profiles – an important complement to the capabilities of the comparatively short-duration Purdue BAM6QT. Details of the M6QT design and infrastructure at Texas A&M are provided in the subsequent sections.

2.1.2. M6QT nozzle description

A cross-sectional schematic of the M6QT nozzle is shown in Figure 2–1, annotated with key features, dimensions, and nomenclature. The nozzle has a 25.4 mm diameter throat and is 1.01 m long, measured from the throat (X = 0) to the exit ($X = L$ = 1.01 m). The nozzle exit diameter is 190.3 mm. The interior contour is of the long-expansion design, where a straight-wall region downstream of the throat with a constant 9.84º angle delays the onset and growth of the Görtler instability which dominates transition.

Upstream of the throat, a protruding lip and exterior contour mate with the contraction (discussed further in Section 2.1.3) to create the bleed slot and plenum through which the contraction-wall boundary layer is extracted.

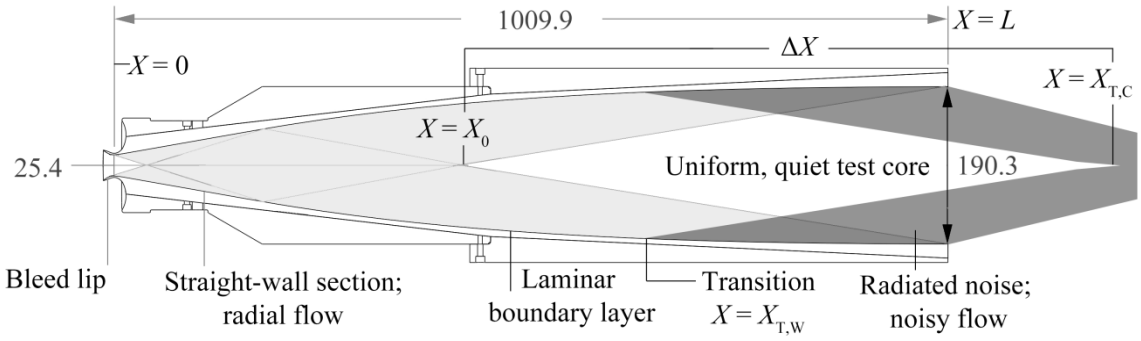

Figure 2–1. Cross-section of M6QT quiet tunnel nozzle design. The design initiates and maintains a laminar wall boundary layer in order to achieve a region of quiet freestream flow. Dimensions are in millimeters.

In an effort to maximize the manufactured quality of the interior contour, the nozzle was fabricated in one piece using an electroforming process, depositing nickel onto a precision-ground, highly-polished stainless steel mandrel.

In the first NASA Langley tests with the nozzle as initially fabricated, a substantial amount of quiet flow was observed. For a unit Reynolds number of 6×10^6 m^{-1} < Re < 15.5×10^6 m^{-1}, transition on the nozzle wall was seen to coincide with a computed Görtler N-factor of 7.5. At the high end of this range, a quiet-core length ($\Delta X = X_{T,C} - X_0$) of 54.4 cm was observed, yielding a quiet-core length Reynolds number, $Re_{\Delta X} = 8.5\times10^6$. Unit Reynolds numbers higher than 15.5×10^6 m^{-1} resulted in an abrupt loss of quiet flow in the entirety of the nozzle, thought to be due to a roughness-induced bypass transition. Further detail on the design and original performance of the M6QT nozzle is given by Chen *et al.* (1993).

Although the quiet flow performance (in $Re_{\Delta X}$) of the Mach 6 nozzle was superior to earlier rapid-expansion Mach 5 pilot nozzle designs, the performance was

unpredictable on a run-to-run basis, and, on average, degraded over time. This was determined to be attributed to atmospheric particle contamination between runs and the formation of a nickel-oxide layer in the throat region via the slow corrosion of the nickel surface when operated at elevated temperatures. The former issue was resolved readily with the addition of a bleed-air purge system used when the tunnel was not in operation. To combat the corrosion issue and to improve the hardness of the material for polishing and particle resistance, the decision was made to chemically (non-electrolytically) deposit a thin layer (50 μm) of an alloy of nickel and 10% phosphorous onto the interior surface of the model.

Unfortunately, this effort was met with considerable difficulty and misfortune. The first step in the plating procedure was to electrolytically deposit a much thinner nickel layer on the surface to prime it for the chemical application of the nickel–phosphorous layer. A copper electrode was placed inside the nozzle as a part of the procedure, but had inadvertently impacted the interior surface, causing pit defects in three locations in the straight-wall section of the contour. Additionally, the high currents used in this process concentrated near the bleed lip, causing nickel nodules to develop. These nodules were repaired as best as possible by hand polishing, but the pits remained. When lapping the nickel-phosphorous overplating proved ineffective in their repair, the decision was made to chemically remove the plating (with some difficulty) and re-apply it. The pits were found to be deep enough that they remained in the base nickel material, and even the re-plating procedure also encountered difficulty. Issues with the circulation of the solution through the nozzle and an inadequate tank size resulted in additional

surface imperfections. An axially-oriented stripe of dull finish down the length of one ray of the nozzle was created by hydrogen bubbles collecting there, and was flanked 15º to either side by low-period surface waviness evident even by visual inspection. After extensive additional polishing work, the waviness was only partially improved, and the stripe of dull plating was polished through to bare nickel. Full detail of these nozzle plating and polishing efforts – conducted by vendors under the advisement of experts at NASA Marshall Space Flight Center and the University of Alabama in Huntsville (UAH) – are described in a detailed report by Rood *et al.* (1992) and in a review by Wilkinson *et al.* (1992).

At the conclusion of the plating effort, performance of the tunnel was reduced as might be expected, albeit was indeed more reliable. Blanchard *et al.* (1997) show that transition locations (and resulting quiet-core lengths ΔX) were comparable to the original nozzle data for $Re < 10\times10^6$ m^{-1}, but the ability to maintain quiet flow at higher Re was lost, with the abrupt loss of quiet flow now occurring near $Re = 10.8\times10^6$ m^{-1} – a 30% reduction.

In initial shakedown testing with the M6QT nozzle as installed in the Texas A&M infrastructure over 20 years later, quiet flow performance was largely consistent with the Blanchard data. To maximize reliability of the quiet flow performance by reducing particle contamination, an opportunity was taken in the fall of 2010 to improve the cleanliness of the shakedown test section by stripping and recoating it. As a part of this process, the test section was sandblasted, thoroughly pressure-washed, and repainted on the interior with a high-temperature, vacuum-rated two-part epoxy. After

reinstallation of the test section and nozzle, however, the subsequent tunnel run exposed the nozzle to fine-grain particulate which had become lodged in the interior seams of the test cabin during the sandblasting process, and which were apparently neither removed by pressure-washing nor trapped by the coats of paint. The fine particulate appeared to be embedded in the surface, necessitating another polishing effort. This time, however, the repair occurred without incident.

Polishing was performed by the Valley Design Corporation of Shirley, MA. One of the smaller, rapid-expansion Mach 5 pilot nozzles – also electroformed and plated, with the same throat and bleed lip geometry as the M6QT – was sent initially as a test piece for technique development. As the UAH group had done previously, Valley Design employed modified cylinder hones with an apparatus that rotated the hone and nozzle and maintained constant axial movement of the hone to avoid creating rings in the surface. The throat region was polished by hand.

During the polishing of the M6QT, it became clear after only a light initial polish that the particulates were readily removed and their damage was not deep. As such, attention in the effort turned toward a more general improvement of the nozzle surface. A miniature right-angle digital microscope offered optical access to previously-inaccessible regions of the nozzle. Deliberate hand-work was performed in order to remove or improve visible defects, particularly in the throat region, although stock removal was kept to a minimum in order to not further expose the bare nickel material. The majority of the significant pit defects (which likely dominate transition) and the waviness downstream of the throat still remain.

In May 2011, the nozzle was returned to Texas A&M and reinstalled alongside many other facility improvements, including a new test section, described below. As Section 5 will show, the quiet-flow performance of the nozzle was largely unaltered by the Fall 2010–Spring 2011 nozzle repolishing effort, remaining at the levels observed by Blanchard *et al.* (1997). In fact, the performance of the nozzle as discussed here is now remarkably reliable; disassembly of the throat for cleaning due to loss of performance has not been required since the polishing was completed.

It should also be explicitly noted that all data presented in this dissertation were obtained following the repolishing effort, and thus represent the current status of the nozzle as of this writing.

2.1.3. Other tunnel components and flow conditioning

Although the nozzle design, construction, surface finish, and bleed-slot provisions described above are the most important aspects of the M6QT's quiet-flow design, a number of other components specific to the facility are crucial to its operation. Shown in Figure 2–2 is a schematic of the M6QT flow path from the settling chamber through the diffuser. This section describes each of these in further detail.

In order to both prevent transition due to surface roughness deposited by contaminants and to protect the nozzle surface from particle damage, a filter with sintered metal elements is employed just upstream of the settling chamber, removing 99.9% of particles greater than 1 μm in diameter.

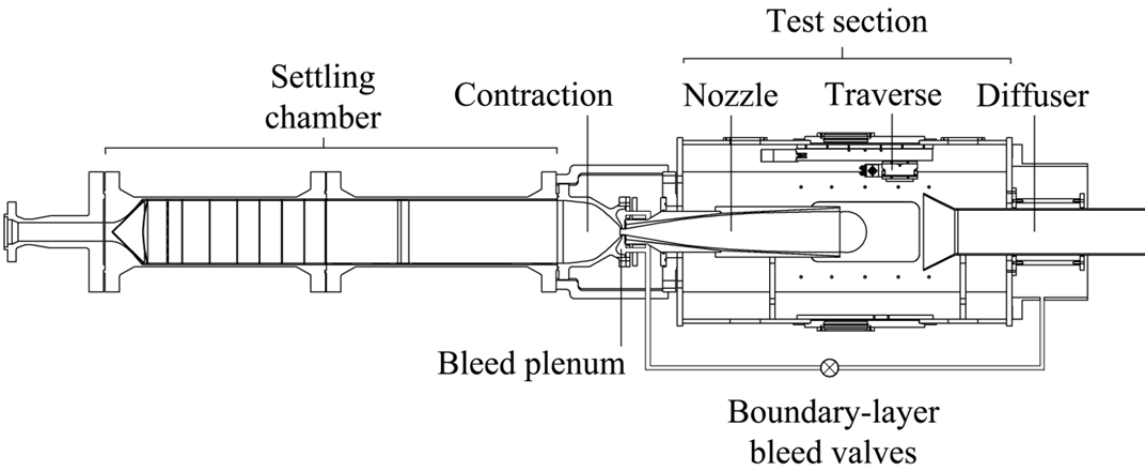

Figure 2–2. Schematic of major M6QT components.

The outlet of the particle filter is connected to the settling chamber inlet with 3.6 m length of corrugated stainless-steel braided hose 102 mm in diameter that has been lined with a smooth-bore Teflon® liner. The lining provides a smooth flow surface and facilitates cleaning versus a standard corrugated, braided hose.

In order to establish a uniform, low-disturbance inlet flow for the nozzle, a large settling chamber, shown schematically in Figure 2–3, employs a number of flow conditioning features. As the inlet flow expands into the settling chamber's interior diameter, it first encounters a dense, conical woven sintered metal plate (Rigimesh®) 3.2 mm in thickness. This material provides a relatively large pressure drop, and serves both to encourage a smooth transition to the larger diameter and to attenuate acoustic noise from valves and regulators upstream. Next, a second Rigimesh® (dome shaped) screen and perforated stainless steel plate (6.4 mm thick, 57% open area) provide additional acoustic attenuation. The remainder of the settling chamber's first meter of

length is populated with seven woven stainless steel wire screens of mesh density increasing from 8×8/cm to 20×20/cm. The flow conditioning devices (pictured in Figure 2–4(*a*)), separator rings (Figure 2–4(*b*)), and smooth-bore machined stainless steel liners provide a continuous flow-path diameter in the settling chamber of 292 mm.

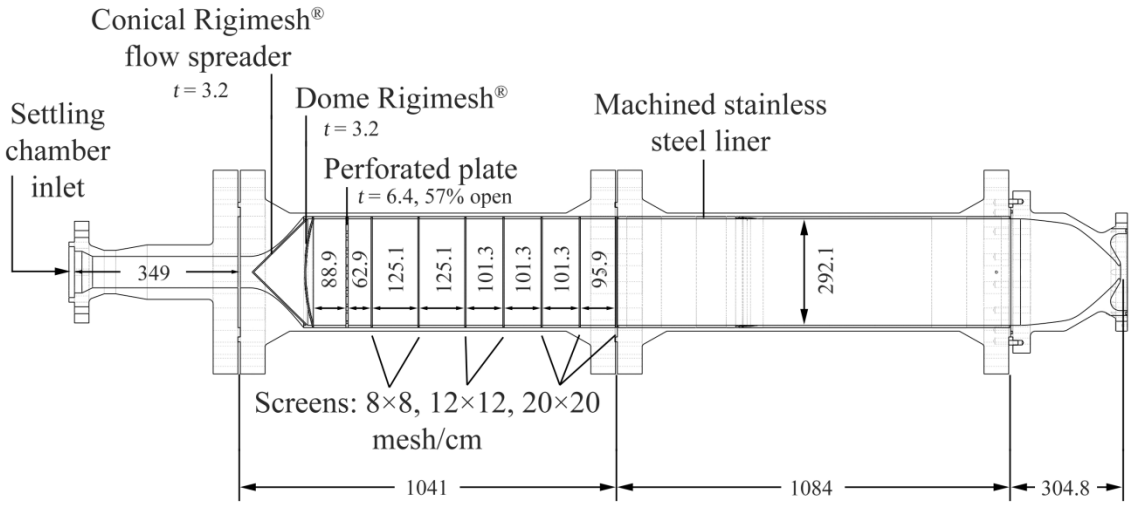

Figure 2–3. Settling chamber cross section and flow quality features. Dimensions are in millimeters. Adapted and updated from Chen *et al.* (1993).

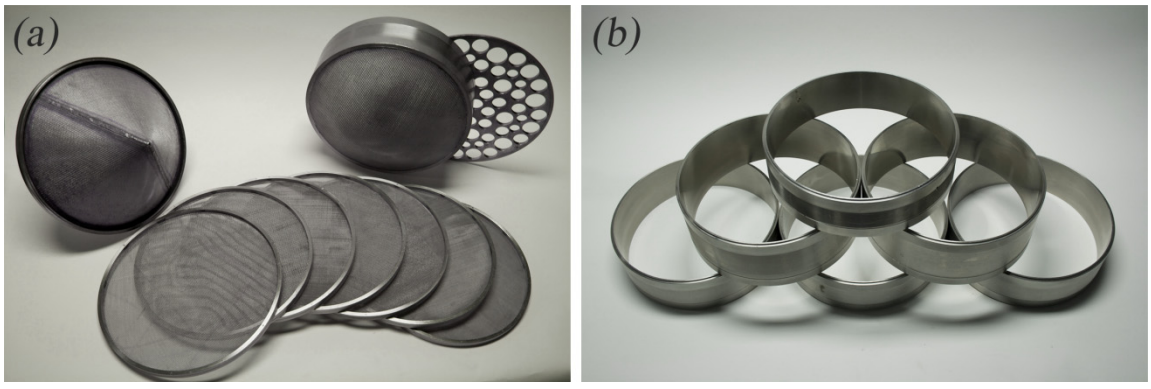

Figure 2–4. Upstream settling chamber flow conditioning components. Shown are (a) Rigimesh®, perforated plate, and screens, and (b) liner spacers.

This settling chamber is the same that was used with the M6QT nozzle at NASA Langley, as well as for earlier pilot nozzles during the early stages of the quiet-tunnel program, although its configuration has slightly evolved. During initial NASA Langley tests of quiet tunnel design methodologies using rapid-expansion Mach 5 nozzle designs, Anders *et al.* (1977) made disturbance measurements in the settling chamber for a number of different configurations of the test-section interior and upstream piping. Turning vanes at the 90º entrance to the settling chamber were found to be largely ineffective, and were removed. Steel wool between the Rigimesh® and perforated plate showed some attenuation of frequencies between 20 and 40 kHz in the settling chamber, but was seen to have no significant impact on the quiet-flow performance of the nozzle, which was dominated by the nozzle surface itself. The steel wool was later removed due to concerns of particle contamination.

Following the settling chamber, a subsonic nozzle – or contraction – region 305 mm in length accelerates the flow with a contraction ratio of 132.25. The contraction mates with the nozzle and its bleed lip contour to create a toroidal chamber through which the turbulent boundary layer is extracted, initiating the laminar boundary layer on the nozzle wall. During installation, shims with a thickness of 10.2 mm set the bleed gap to the optimum dimension as guided by the NASA experiments (Chen *et al.* 1993) and confirmed for the present installation with a parametric study during initial shakedown testing. A cross-section of the mate between the contraction, nozzle bleed lip, and bleed plenum is shown in Figure 2–5.

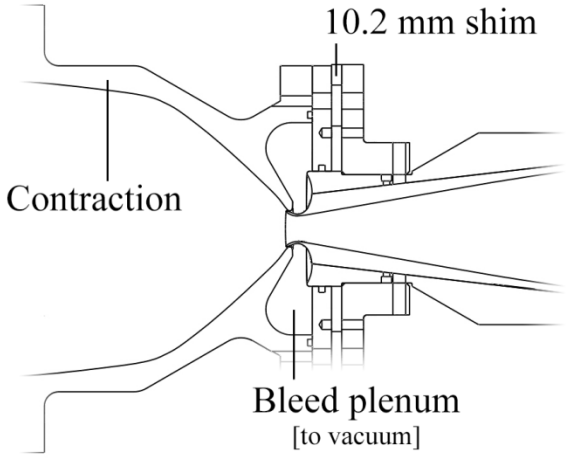

Figure 2–5. Cross-section of contraction–nozzle assembly, with bleed lip and plenum.

Downstream of the nozzle itself (already described in detail above) is the large test section. The test section serves as a vacuum chamber inside which the nozzle, test jet, and diffuser are contained and operated. In this fashion, the M6QT operates in an enclosed-free-jet configuration (Pope & Goin 1965). The test section's interior height and width (0.81 m square, with corner relief) allow sufficient interior room for model and instrumentation mounting provisions, including a multiple-axis probe traversing mechanism (§3.2) on the interior ceiling. Several access ports are provided for maintenance and instrument cable penetration, and large-aperture doors on all four walls allow optical access to the test area (200 mm diameter) from any direction, although typically the floor and ceiling are left closed for the test model and traverse.

In response to the flaws in the design of the shakedown test section and its operation that led to the contamination of the nozzle, this new test section has several design features that maximize the cleanliness of the test chamber. All interior plate-to-

plate seams are fully welded, and therefore there are no gaps on its interior where particles can collect. Furthermore, the stainless steel construction does not require a coating or paint.

The final component of the M6QT flow path is the diffuser pipe. A simple aluminum bell mouth with a 348 mm maximum diameter and 25º entrance angle is placed at a fixed 1.8 nozzle-exit diameters downstream of the nozzle. The diffuser pipe itself is a simple 1.8 m section of extruded aluminum tubing with a 203 mm interior diameter, which exhausts directly into the 609 mm diameter exhaust pipe connected to the vacuum source. The diffuser has no interior contour, and no attempt was made to optimize its efficiency, as tunnel run time is heavily dominated by the mass flow requirements of the vacuum ejector infrastructure, as discussed below.

2.2. Infrastructure and operation at Texas A&M

2.2.1. Infrastructure overview

The M6QT tunnel facility components as described above are installed at the TAMU National Aerothermochemistry Laboratory (TAMU-NAL) in College Station, Texas, and are operated in a pressure-vacuum blow-down configuration. Vacuum is supplied by a two-stage Fox-brand Venturi air-ejector system capable of generating a minimum starting backpressure of 4 torr using, as its motive air, approximately 20 kg/sec of compressed air at 10.2 atm. Tunnel run time is largely governed by the high mass flow requirements for the ejector.

High-pressure air is provided by two Chicago Pneumatic air compressors (250 SCFM each), filtered (99% efficient sub-micron), dried with a twin-tower desiccant drier to –40ºC, and stored in a 23.2 m^3 tank at 170 atm. Air is supplied to the ejector via a 4-inch carbon-steel pipe system, and air to the tunnel is delivered through a 2-inch stainless steel line, heated by a 500 kW Chromalox electric-resistance heater (up to 533 K output), and filtered again, removing 99.9% of particles larger than 1 μm just before entering the tunnel. Both pipelines are controlled by a combination of Bray pneumatic actuators, which start and stop the ejector and tunnel systems, and a series of Stra-Val regulators that provide the correct control pressure to the ejector system and the desired stagnation pressure to the tunnel.

In its early shakedown installations in 2008 and 2009, the M6QT operated in the TAMU-NAL interchangeably with the Adaptively-Controlled Expansion (ACE) Mach 5–7 tunnel (Semper *et al.* 2009). In this arrangement, one tunnel would be removed from the infrastructure for months at a time to allow the other to complete a test campaign. In November 2009, this was significantly improved with the conclusion of a major construction project allowing both the ACE tunnel and the M6QT to be permanently installed in the same laboratory and share the same pressure-vacuum infrastructure. The vacuum from the ejector system is supplied to either tunnel by using a pair of 609 mm diameter actuated knife gate valves, and pressure is supplied to either tunnel using a pair of manual ball valves downstream of the 1-micron particle filter. With these improvements, it is possible to switch between active facilities in a matter of

minutes by the simple toggling of valves, minimizing facility downtime and maximizing experimental productivity and repeatability.

2.2.2. Tunnel operating envelope and procedures

Nominal operating conditions for the M6QT are listed in Table 2–1. To avoid the liquefaction of oxygen in the expanded flow, the M6QT flow is always heated to and maintained at a stagnation temperature, T_{t1}, of 430 K. The nominal range of stagnation pressures, p_{t1}, for which quiet flow is observed in the nozzle with bleed valves open is 200 to 1000 kPa, or Re = 2.3 to 11×10^6 m^{-1}. The tunnel can operate at higher pressures – up to approximately 1350 kPa, or Re = 15×10^6 m^{-1} – but the flow is noisy regardless of the state of the bleed valves. The quiet flow performance of the nozzle is discussed in far greater detail in Section 5.

Table 2–1. Nominal operating conditions for M6QT.

	T_{t1} [K]	p_{t1} [kPa, absolute] (psia)	M [ ]	Re [10^6 m^{-1}]
Quiet (BVO)	430	200 – 1000 (30-145)	5.9	2.3 – 11
Noisy (BVO)	430	1000 – 1350 (145-195)	5.8	11 – 15
Noisy (BVC)	430	200 – 1350 (30-195)	5.8	2.3 – 15

In order to provide context for the experiments performed for this work, it is also instructive to briefly describe the manner in which a typical run of the M6QT is conducted, as certain aspects of the procedure have implications discussed later.

To achieve the typical operating total temperature of 430 K, the M6QT must be preheated convectively prior to a full tunnel run by sending air through the tunnel subsonically at a total pressure of 3.4 to 6.8 atm without activating the ejectors. With the 500 kW heater active, this process takes 10–15 minutes for the first run of the day. For subsequent runs, the preheating process takes less time, as the tunnel supply piping and settling chamber are fully insulated with fiberglass insulation blankets and retain their heat well throughout the day. Additionally, 8 kW of direct heating on the settling chamber is provided by Ogden Mighty-Tuff electric-resistance band heaters and a Chromalox 3340 closed-loop controller in order to maintain the high-thermal-inertia settling chamber at 430K, which greatly reduces preheating requirements.

Once the tunnel achieves the proper temperature, the subsonic airflow is stopped, regulator control pressures are set as required, and final safety checks are made. A full tunnel run is initiated by first activating each of the two stages of the vacuum ejector system. After 4–5 seconds, the tunnel is evacuated to ≈10 torr up to the settling chamber pressure regulator, which is located just upstream of the particle filter. At this time, an actuated ball valve just upstream of the 500 kW heater is opened, filling the settling chamber to the set pressure and starting the nominally Mach 6 flow.

The tunnel is started in this manner with its bleed valves closed (BVC). Very shortly after started flow is established in the tunnel, the bleed valves are opened (BVO), initiating the “on-condition” portion of the run, with constant stagnation temperature and pressure and a low-disturbance freestream test environment. Conditions are maintained

in this manner for up to 40 seconds as the high-pressure air tank is depleted from 170 atm to approximately 95 atm. During this time, experiments are performed.

When the tank reaches approximately 95 atm (just prior to the natural unstart of the ejectors, given pressure losses and regulator characteristics), the tunnel bleed valves are first closed, and then the valve which supplies the ejector motive air is closed, which causes a rapid loss of vacuum and subsequently unstarts the tunnel. A valve on the tank which supplies the clean tunnel air supply is also closed, and the remaining air in the line is allowed to vent through the tunnel subsonically.

2.3. Instrumentation and data acquisition

Discussed below are the generic instrumentation and data acquisition (DAQ) implementations utilized for the M6QT and laboratory infrastructure. Detail of the primary experimental setups is provided in Section 4.

A wide variety of instrumentation is employed throughout the infrastructure for the monitoring of system pressures and temperatures. Largely, generic infrastructure parameters are monitored using Omega-brand pressure transducers and type-K thermocouples. Measurements more critical to the M6QT experiments, however, utilize more accurate pressure sensors from MKS. Settling chamber stagnation pressure is measured using an MKS Baratron 615A High-Accuracy Capacitance Manometer with a 10,000 torr full scale range, together with an MKS 670B Signal Conditioner. The unit is temperature compensated and accuracy is quoted to ±0.12% of the reading. Test section and diffuser pressures are measured using MKS 902 Piezo Vacuum Transducers with a

1,000 torr full scale range and accurate to 1% of the reading. Alternatively, for more critical vacuum measurements, MKS Baratron 631C temperature-stabilized capacitance manometers are available in 10 and 100 torr ranges, with substantially better accuracy of 0.5% of the reading.

Data acquisition provisions for the M6QT are provided by two desktop computers equipped with National Instruments (NI) data acquisition hardware and custom LabVIEW software.

One system, the "NAL–DAQ", is dedicated to the monitoring and acquisition of a wide number of general parameters, including pressures and temperatures in the laboratory's tunnel and ejector air supply systems (common to the M6QT and ACE), as well as each tunnel's stagnation, test cabin, and diffuser conditions, M6QT bleed valve state, and more. This system is equipped with an NI USB-6255 M Series 16-bit multiplexing data acquisition board with 40 differential input channels. These data are sampled at 1 kHz per channel, averaged to 10 Hz, and saved in a spreadsheet for each run. Between runs, the NAL–DAQ operates in a monitoring mode, where key pressures and temperatures are available both on-screen and online in real time (e.g. high-pressure air tank fill status, tunnel pre-heating status, etc.). The NAL–DAQ LabVIEW program also sends alerts to tunnel operators when the high-pressure air tank is full.

The other system, "M6QT–DAQ," is dedicated to the specialized experimental data acquisition needs of the current M6QT campaign. Depending on the experiment, this can include integrated functionality for: low-bandwidth, high-channel-count acquisition of test article wall temperatures (§3.1.2), control of the multi-axis probe

traversing mechanism (§3.2), high-bandwidth acquisition of data from hot wires (§4.1), Kulite (§4.2.1) or PCB (§4.2.2) pressure sensors, or optical (§4.3) diagnostics, as well as additional capabilities like instrument control. In addition, several key tunnel flow parameters (e.g. p_{t1}, T_{t1}, etc.) are acquired simultaneously on M6QT–DAQ as well as NAL–DAQ, allowing for proper matching between the experimental and infrastructure data.

Specifics of the data acquisition and filtering schemes are described in further detail in the above-referenced sections. In general, the low-bandwidth tasks are enabled by an NI SCXI acquisition chassis outfitted with several multiplexing voltage and thermocouple input modules. High-bandwidth acquisition is enabled using an NI USB-6366 X-Series Data Acquisition board, which offers 2 MHz sampling across 8 differential channels with simultaneous sampling. That is, each channel operates with an independent analog-to-digital converter, eliminating cross-talk issues that can often arise when sampling at high rate on a multiplexing acquisition board.

All of the software and hardware described above have been selected, implemented, and programmed by the author specifically as a crucial part of the re-establishment of the tunnel and its necessary experimental capabilities.

3. EXPERIMENTAL CONFIGURATION

The experimental apparatus for the present work principally consists of a flared cone test article for the study of the second-mode instability and a two-axis precision probe traversing mechanism. The traversing mechanism serves as a versatile platform for enabling the efficient acquisition of freestream data, boundary-layer profiles, and azimuthal scans with a variety of diagnostics, and also serves to enable precise optical alignment of the flared-cone model. The following sections detail these components and associated procedures.

3.1. Flared-cone model

The model used in the present study is the Langley 93–10 flared cone, shown in Figure 3–1. This is the same test article as was used for the work at NASA Langley of Lachowicz (1995), Doggett (1996), and Horvath *et al.* (2002) as discussed in Section 1. The model was selected because of its well-studied history, enabling direct comparisons to past work in order to guide the initial experiments in the new Texas A&M laboratory and initial implementation of its new diagnostics and methods. The work would then naturally evolve to expand upon the work of the Langley researchers with the study of nonlinear interactions and the breakdown process.

The subsections to follow describe the model geometry, its embedded instrumentation, and the methods by which it is installed and aligned.

3.1.1. Geometry

The flared-cone geometry consists of a 5º half-angle right-circular conical profile for the first 254 mm [10″] of axial distance, followed by a circular flare of radius 2.36 m [93.071″] until the base of the cone at the 508 mm [20″] axial station. The flare is tangent to the cone at the 254 mm station, but a curvature discontinuity is present here.

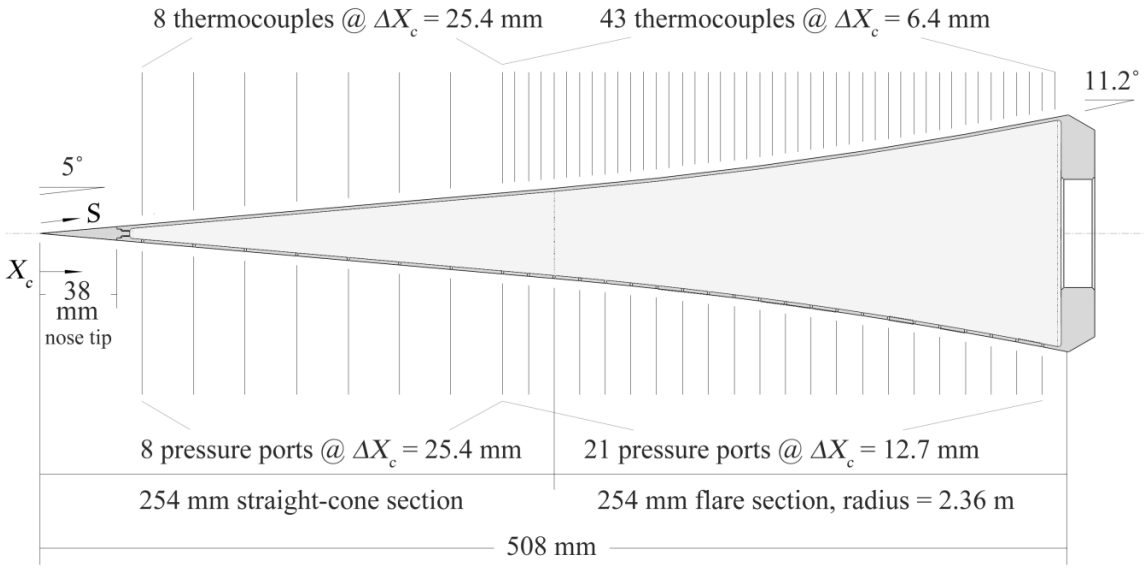

Figure 3–1. Cross-section of the flared cone model and embedded instrumentation.

The adverse pressure gradient imposed by the flare serves to destabilize the second-mode instability, promoting additional growth within the small quiet test environment of the M6QT. The base diameter is 0.12 m. The model is of a thin-wall stainless steel construction with nominal wall thickness of 1.8 mm. The first 38 mm of length can be removed and replaced with alternate nose-tips. The present experiments utilized nominally sharp tips, for which the manufacturing specification was for a nose

radius of 2.54 μm. The blunt tips used by Lachowicz (1995) are also available in radiuses of 0.8 mm, 1.6 mm, 2.4 mm, and 3.2 mm, although any of these blunt tips were found by Lachowicz to reduce instability growth and delay transition on the model, and are therefore not presently of interest.

Coordinate tolerances on the model are quoted as being within 25 μm on the radius in the straight section, and 50 μm on the flare. Coordinate measurements at Langley revealed a maximum RMS radius error less than 2.8% of the model boundary-layer thickness (Lachowicz *et al.* 1996). The model is polished to a surface finish of 50–100 nm RMS for the first 0.18 m of length, and 150–200 nm thereafter. Surface waviness is within 0.2 μm/mm.

3.1.2. Embedded instrumentation

The model is instrumented along two axial rays separated by 180º azimuthally. Along one ray is a total of 29 pressure ports (8 in the straight-wall section, and 21 along the flare) 1 mm in diameter, whereas the opposite ray contains a total of 51 Type K thermocouples (8 in the straight-wall section, and 43 along the flare) welded to the interior wall. The wall thickness beneath the array of thermocouples is reduced to 0.8 mm in order to reduce the thermal inertia, improving measurement response time.

Although transition location measurements are only briefly discussed in Section 6.2, the embedded thermocouples are sampled during every tunnel run as a simple diagnostic, and to establish a wall-temperature condition for computational comparison. The data are sampled using a National Instruments SCXI multiplexing

acquisition chassis equipped with three SCXI-1102 thermocouple input modules, offering a total of 96 channels of thermocouple inputs with 2 Hz low-pass filtering. These data are monitored during initial tunnel preheating and acquired at 10 Hz during each run.

3.1.3. Installation and alignment

Because most of the freestream quiet flow environment exists inside the M6QT nozzle itself, the flared-cone test article is placed far into the nozzle such that its tip is only just downstream of the last characteristic on the nozzle centerline. Figure 3–2 depicts the installation of the flared cone inside the M6QT test section. In this position, 406 mm of the cone length is inside the nozzle, with the base of the flared contour located 102 mm aft of the nozzle exit plane. This placement is approximately 12 mm downstream of the location used by Lachowicz (1995). With the model in this location, the aft portion of the flared cone is available for optical diagnostics (e.g. schlieren imaging and/or deflectometry) and is easily accessible for hot-wire profile measurements.

Placement of the model within the M6QT test section is discussed in additional detail in Section 5.5 within the context of the measured spatial extent of the quiet test core.

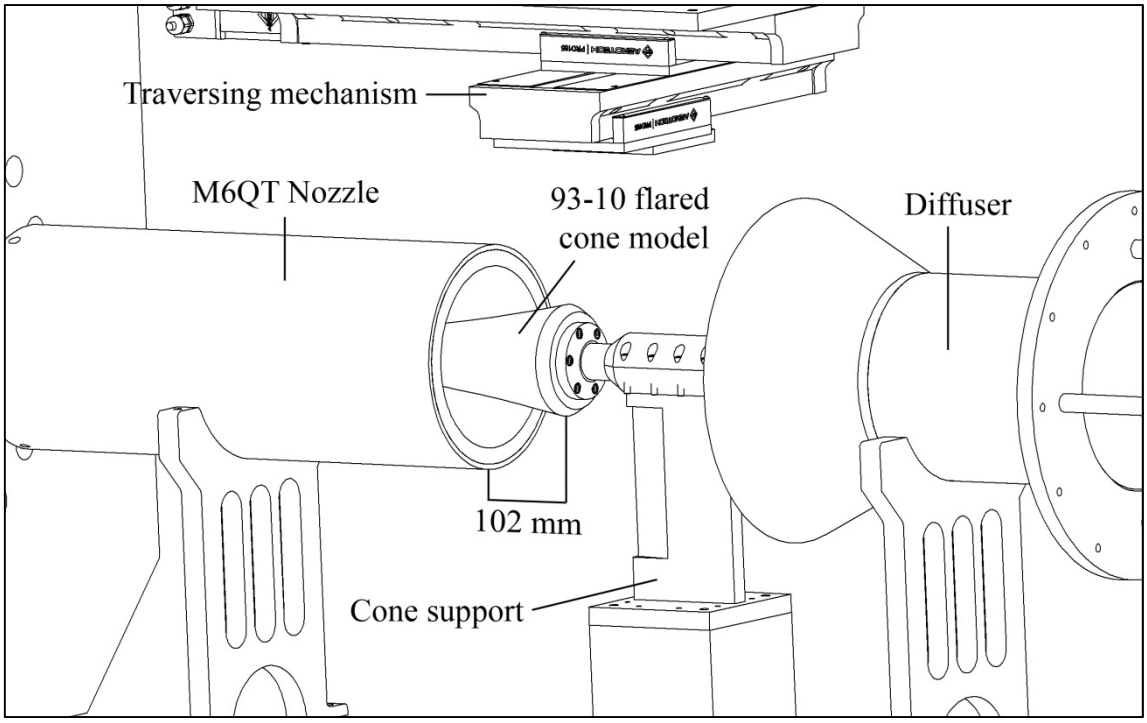

Figure 3–2. M6QT test section with 93–10 flared cone model and traverse. Test cabin walls are hidden for clarity.

The model was aligned to a nominally zero degree incidence in pitch and yaw, and was geometrically quantified using a Keyence LT-8120 Confocal Laser Displacement Sensor system mounted to a two-axis traversing mechanism on the interior ceiling of the test enclosure. The traversing mechanism is discussed in further detail in Section 3.2.

The Keyence device outputs a voltage signal proportional to a height difference, with a maximum range of 2 mm and resolution of 0.2 μm. The LT-8120 was scanned in grid patterns across the upper surfaces of the nozzle's outer sheath and of the cone support shaft, producing a three-dimensional point cloud of each surface in the reference

frame of the traverse's axes of motion. Then, in each axial slice through the point cloud, circles of known diameter (235 mm for the nozzle sheath, 38.1 mm for the cone shaft) were fit to the data to determine the position of circle centers at each axial location. From these center locations, pitch and yaw angles relative to the traverse axis of motion were determined. By comparing the traverse-relative alignments of the cone and nozzle, the alignment of the cone to the nozzle was determined.

Representative scanned data from the confocal laser and the resulting best-fit circles for the cone shaft are shown in Figure 3–3.

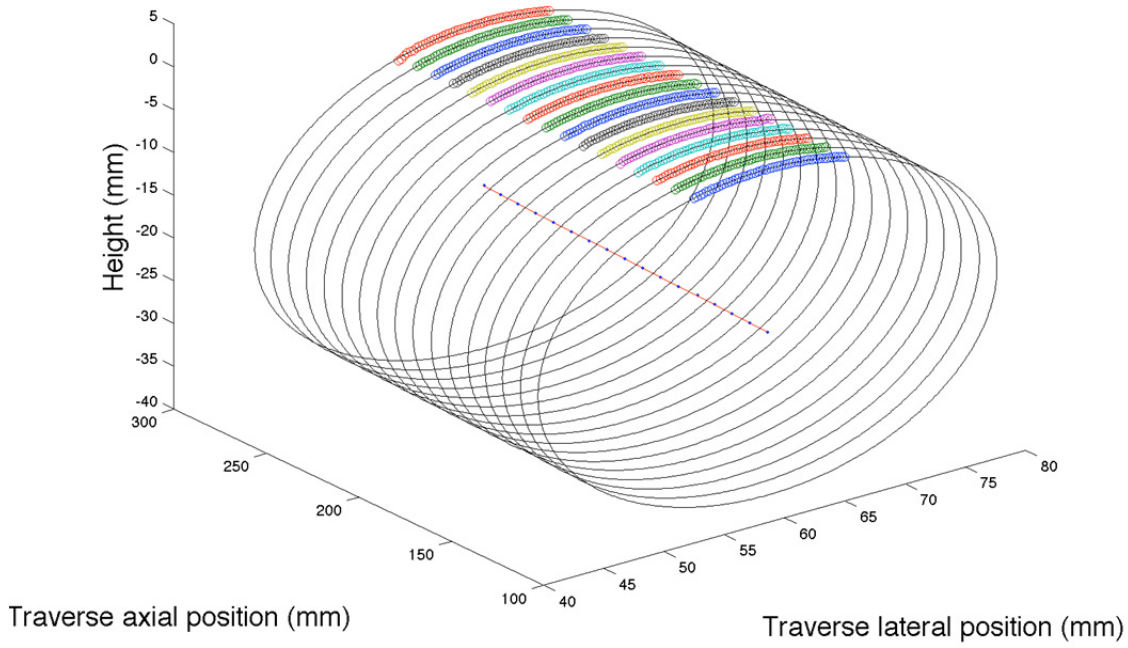

Figure 3–3. Example alignment data from confocal laser scan of the 93-10 cone shaft. Collected height data are displayed as markers on top; best-fit circles and resulting centerline shown below.

This method relies upon the assumption that the nozzle flow is concentric with the nozzle's stainless-steel sheath, and that the cone body is concentric with its own shaft. Given the tight tolerances with which both parts were constructed, this assumption was deemed reasonable for the present study.

Cone alignment issues are further explored in Section 6.6 by comparing most-amplified second mode frequencies on the upper and lower rays of the cone using the focused schlieren deflectometry system.

3.2. Probe traversing mechanism

A vital part of the M6QT's set of experimental capabilities is its versatile, multi-axis probe traversing mechanism. Because of the broad potential utility of these systems to a wide variety of types of research, this system was brought online early in the re-establishment of the tunnel. It was designed with campaigns for both spatial freestream characterization and hot-wire profiles of O(1 mm) boundary layers as primary goals, but was implemented in a manner general enough to enable a wide variety of future capabilities.

The following subsections describe the traversing mechanism itself, several of its most common experimental configurations thus far, and its practical operation.

3.2.1. Design selection and system specifications

After much research and consideration, and in observance of the advice of researchers from NASA Langley and Purdue University regarding their recent

experiences with the motion control systems used in their quiet tunnels, a commercial motion solution from Aerotech, Inc. was selected.

Because the system was originally configured for use in the M6QT's original, 33% smaller shakedown test section, it was built as – and remains – a compact two-axis device. In this regard, the current capability effectively mirrors that used by Blanchard *et al.* (1997) and others in the facility's previous installation at NASA Langley. The current, larger test section is likely large enough to support a third Cartesian axis if it becomes necessary for future work.

Two Aerotech PRO165 Mechanical-Bearing Ball Screw Linear Stage tables are mounted in an *X*–*Y* configuration to the interior ceiling of the M6QT test section, and provide 400 mm of travel in the axial direction and 200 mm of travel laterally. This assembly is shown in Figure 3–5(*a*). A precision ball screw with a 5 mm/rev lead and two linear motion guides serve as the primary mechanics. The standard mechanical positioning accuracy of the mechanics is on the order of, but larger than, the diameter of a hot wire, at ±8 μm for the 200 mm lateral stage and ±12 μm for the 400 mm axial stage. However, the stages were calibrated at the factory with Aerotech's "HALAR" (High Accuracy Linear and Rotary) option to provide the motion controllers with a linear error correction table to offset these inaccuracies in the mechanics; this improves the overall system accuracy to better than ±5 μm at room temperature.

Each ball screw is driven by a BM130 brushless servomotor. Position feedback is provided by 2500-line quadrature encoders integrated into the motor housings, yielding a theoretical position resolution of 0.5 μm. Again due to the anticipated space constraints

of the original M6QT test section, the lateral stage is equipped with a “motor fold-back” option, which makes the stage more compact using a belt-and-gear indirect drive setup. The factory calibration and motor controller software include automatic corrections for any backlash in this setup.

Motor power and closed-loop position control is provided by two Aerotech Ensemble HLe Controllers and Linear Drives. These controllers internally coordinate motor drive and position feedback functionality, and communicate through a Gigabit Ethernet connection and LabVIEW application programming interface (API) on the M6QT data acquisition computer. The control laws are independently tuned for typical loads and operating temperatures, and are specifically optimized for efficient and accurate stop-and-go motion, as opposed to on-the-fly accuracy.

Special care was taken in the selection of the electronic components such that they would not interfere with sensitive hot-wire anemometry work. Previous experience at both NASA Langley and Purdue using stepper-motor and early Aerotech motion systems indicated difficulty with electromagnetic interference (EMI) on hot-wire measurements (Wheaton 2010). These experiences guided the configuration and selection of the present system, and additional tests were performed. Prior to purchase of the Texas A&M system, loaner equipment was obtained from Aerotech, and extensive EMI testing was performed. The combination of the BM130-series brushless motor and the Ensemble HLe controller (with its linear motor-drive power supply) was found to cause no discernible effect on the noise floor of hot-wire measurements, whether during active motion or under simple holding torque.

Figure 3–4. LabVIEW VI for combined probe traverse motion and data acquisition.

The Aerotech traversing mechanism is controlled via a custom, event-driven LabVIEW virtual instrument (VI) written specifically for this work, for which the front panel – or user interace – is shown in Figure 3–4. The program integrates the necessary provisions for manual or automated motion control (freestream scans, boundary-layer profiles, etc.) as well as data acquisition setup, test, and execution for hot wires, Kulites, PCBs, focused schlieren, or other diagnostics at up to 2 MHz. Also included are provisions for RS-232-based control of a Keithley 2000 Multimeter for the acquisition of cold-wire resistance profiles.

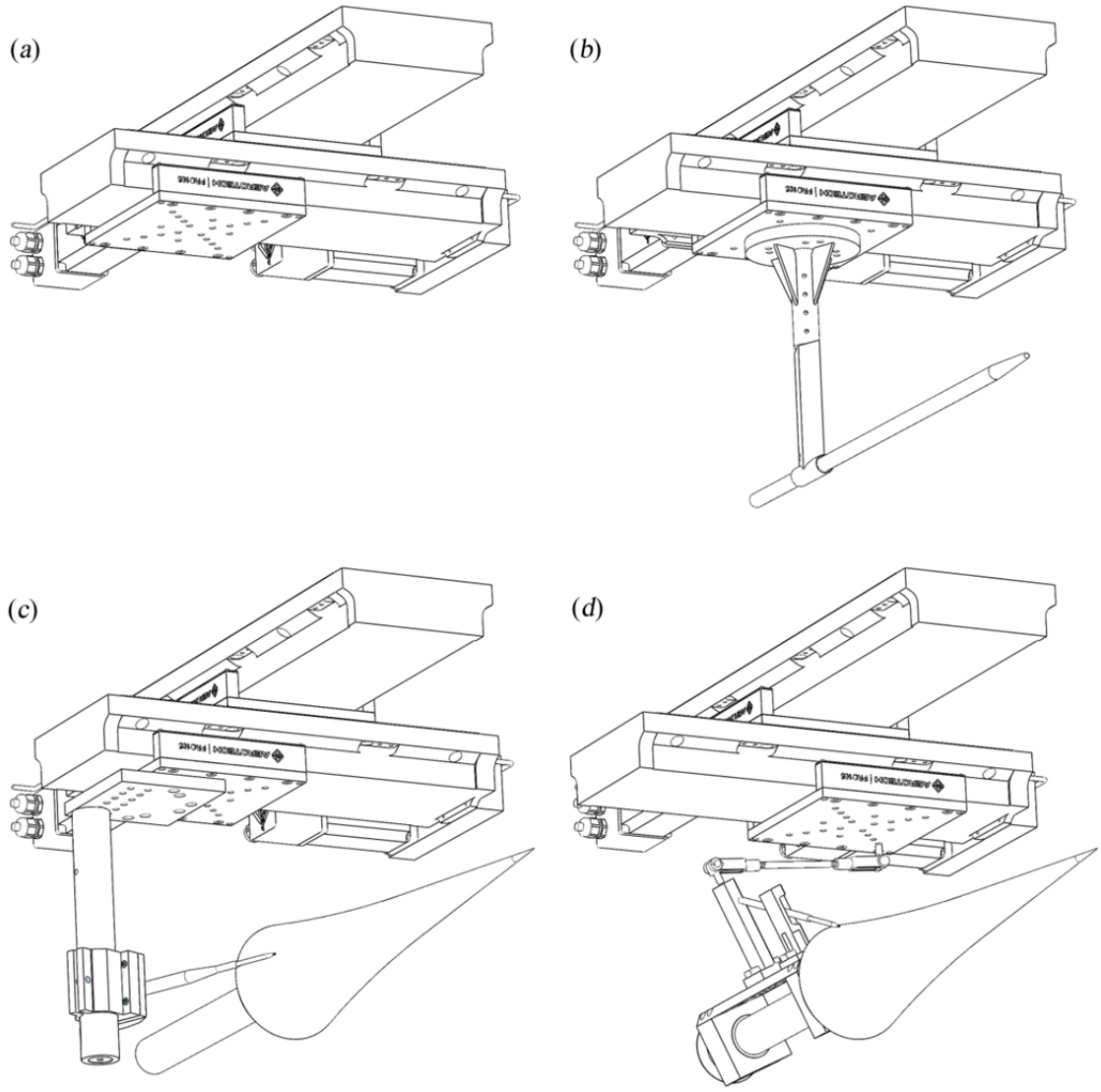

Figure 3–5. Schematics of the M6QT traverse in various experimental configurations. The (*a*) Aerotech PRO165 system is mounted to the interior ceiling of the enclosed-free-jet test section and configured for (*b*) freestream Pitot pressure or hot-wire scans, (*c*) hot-wire profiles on a cone model, or (*d*) azimuthal hot-wire scans by means of a linkage connected to a rotating platform.

3.2.2. Freestream characterization configuration

For two-dimensional instrumented scans of the tunnel freestream – such as for the flow quality characterization presented in Section 5 – the probe traverse can be equipped with a generic sting probe support as shown in Figure 3–5(*b*). A stainless steel tube 14.2 mm in diameter and 760 mm long serves as a probe support for Kulite pressure sensors, PCB pressure sensors, or hot-wire probes. Tapered conical tips are employed as appropriate.

The vertical support sting is streamlined on the upstream and downstream sides with 22º half-angle wedges. The sting can be raised or lowered for scan of off-center planes, and the long stainless-steel tube can be fixed to the wedged support sting with set screws at any axial position along its length, allowing the arbitrary selection of axial coordinate ranges available in a given motion profile. If necessary, the entire traverse assembly can be moved from the test section ceiling to either interior wall to enable scans in vertical planes (*X*–*Z* vs. *X*–*Y* motion).

To minimize vibration, the stainless steel tube has a relatively thick wall (3 mm), and probe cables are routed out of the flow carefully, routed internally wherever possible, and otherwise taped down securely with high-temperature, fiber-reinforced tape.

3.2.3. Boundary-layer profile configuration

In order to acquire boundary-layer profiles on the flared cone model as for the experiments of Section 6, the traversing mechanism was equipped with an offset probe

holder as shown in Figure 3–5(*c*). Here, a straight hot-wire probe body was mounted to the probe holder at an angle sufficient that the 40 mm diameter optical post used as a vertical support would remain out of the nozzle flow. Height of the probe was set manually to coincide with the center-plane of the flared cone. By mounting the cone with small incidence about the vertical axis, this configuration allows the acquisition of boundary-layer profiles on leeward and windward rays. This configuration closely mirrors that used by Lachowicz (1995), Doggett (1996), and Blanchard and Selby (1996) in the original series of cone studies conducted in the tunnel at NASA Langley.

To protect the hot wire from breakage during starting and unstarting shocks, this configuration allows the probe to begin and end the run "parked" just behind the base of the cone. Upon the establishment of started flow, the wire emerges and acquires a boundary-layer profile at any axial station on the cone. Within a single full-duration run, 40 to 60 points in the boundary layer can be acquired.

3.2.4. Azimuthal scan configuration

An additional, novel traverse configuration was devised for the study of azimuthally-periodic structures which develop in the boundary layer through nonlinear interactions between the fundamental, streamwise 2-D second-mode and oblique modes. The mechanism is also suitable for the study of crossflow for a cone mounted at an angle of attack.

There is precedent for probe-traversing mechanisms with this capability. At a significant cost and extended time of design and iteration, Owens *et al.* (2011) have

developed for the NASA Langley SLDT an exquisite cone-mounted three-axis traversing mechanism which allows for precise axial, azimuthal, and wall-normal positioning of a miniature Pitot or hot-wire probe. As a low-cost, low-risk alternative to this ideal capability, the present configuration employs only a single azimuthal axis, and powers this axis via a mechanical linkage to the Aerotech traversing mechanism on the interior ceiling of the test section.

In this configuration, shown in Figure 3–5(*d*), a rotating platform is mounted to two bronze sleeve bearings, spanning across the clamping sleeve which affixes the cone to its own sting support. Mounted to the platform is a simple probe holder with fine-thread screw adjustment which holds the probe at a fixed axial and wall-normal position.

Also mounted to the rotating platform is a wedged riser which provides a streamlined mounting point for a clevis joint connection to a linkage which then connects to the Aerotech motion table. The linkage joints have very tight tolerances to minimize backlash in the mapping between azimuthal angle and the lateral traverse axis of motion. Utilizing the entire 200 mm travel of the lateral traverse axis, a ≈55º range of azimuthal motion is achieved. The resulting resolution of azimuthal motion is at least an order of magnitude finer than the effective azimuthal span of a hot-wire probe element, so the linkage mechanism itself does not limit the resolution of a measurement.

The entire mechanism, save for the probe, streamlined probe support, and linkage riser, fits behind the 117 mm cone base diameter; very little blockage is added.

While this linkage-based azimuthal traversing mechanism has been successfully implemented in an initial exploratory campaign for the study of breakdown structures on

the 93–10 flared cone, this work is not yet mature and results will not be reported in this dissertation. Concurrently with this ongoing work, the mechanism design is also being expanded upon by other M6QT researchers to include multiple axes for future studies of crossflow and transient growth.

3.2.5. Probe height determination

In addition to ensuring the positioning accuracy and repeatability of the probe traversing mechanism itself, it is important to properly register the probe coordinates to the experimental frame and model surface, particularly for work in the flared cone boundary layer, which is nominally only 1.5 mm thick.

Depending on the setup, one of two methods was used for the determination of probe height. For the acquisition of boundary-layer profiles using the configuration described in Section 3.2.3 (as for the results presented in Section 6), the model wall was located in traverse coordinates by slowly, carefully making contact between the hot-wire prong tips and the body of the model at each axial profile location. Because the hot-wire prongs are electrically insulated from the tunnel and model, this is a straight-forward procedure performed with a multimeter connected between the model and hot wire, and operated in a mode which produces a tone when continuity is achieved. The hot wire is moved in very small, slow steps (≈10 μm) and is not damaged in the process. Because the hot-wire body is positioned at a relatively steep angle in this setup, the wire makes contact with the wall very near the tip (rather than on the side of a prong or on the

rounded edge of the prong tip), and so the offset between the contacted area and the actual active sensing element is minimal.

When it is not possible to use the contact method, such as for a probe installed at a fixed height on the azimuthal mechanism of Section 3.2.4, an optical technique is used. Here, a Keyence LS-7030 Optical Micrometer is used. This device uses produces a thin, collimated sheet of light 33 mm tall and 160±40 mm wide using a GaN green LED in one of two enclosures. In the other enclosure on the opposing end of the sheet, a CCD detects the light sheet and measures the width of any interruptions to it (i.e. shadows) with an accuracy of ±2 μm. The minimum detectable gap is nominally 0.15 mm, approximately the width of the hot-wire prongs at their tip.

Figure 3–6 depicts the Keyence optical micrometer as installed and used in the M6QT test section. The device is mounted to a two-axis, manually-adjusted precision linear stage, which is itself mounted to a clamp sized specifically to fit around the nozzle exterior. These mounting devices allow the micrometer to be positioned precisely at a given axial, radial, and azimuthal position. To take a probe-height measurement, the azimuthal clamp mount is fixed with the LED sheet just in front of the probe, at an angle selected to match the inclination of the probe body, whether it is mounted on the azimuthal mechanism or directly to the traverse in the profile configuration. The angle of the micrometer axis is initially set using a digital inclinometer. Next, the radial positioning stage is manipulated such that the cone begins to interrupt the bottom edge of the sheet of light, registering an initial measurement on the display of the micrometer controller. Finally, the axial positioning stage is manipulated such that the prong tip only

just barely pierces the LED sheet, creating another registered measurement on the display – the probe tip diameter at approximately 150 μm. At this point, the display also reads out the gap distance between the cone surface and the probe tip. This measurement is the height of the probe tip above the wall. The measurement procedure can then be repeated at several azimuthal locations to verify the constant nature of the probe height above the model surface.

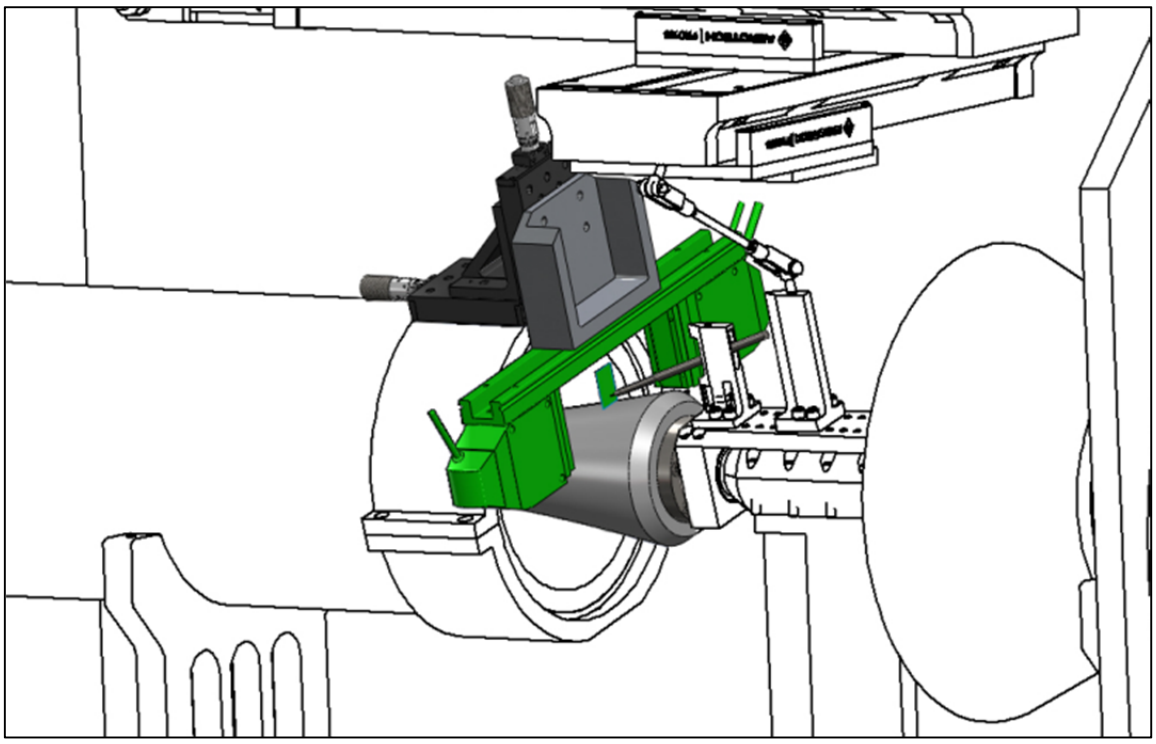

Figure 3–6. Optical micrometer apparatus for determining hot-wire probe height. Pictured in green is the Keyence LS-7030 optical micrometer, mounted to two fine-positioning linear stages and a clamp ring around the nozzle for axial, radial, and azimuthal position adjustment.

To compare the probe position as determined by the optical and contact methods, the optical micrometer was used to determine the height of a hot-wire probe in the boundary-layer profile configuration, positioned 1.5 mm off the model surface following a contact-method wall-finding procedure. The height measured by the micrometer was within 25 μm of the set height. Thus, for typical boundary-layer measurements, the uncertainty probe height is estimated to be approximately 0.02δ.

There is, of course, still an inherent weakness in both of these methods in that they are each performed without flow in the test section, and thus without a dynamic pressure acting on the probe body and support, potentially deforming its position. To alleviate these concerns for a representative run of each probe configuration, a high-definition video camera was equipped with a zoom lens and focused on the probe tip with high magnification prior to a run. During startup and throughout the duration of a run, video was taken and inspected after the run was completed. In each case, no discernible movement of the probe tip was observed.

4. EXPERIMENTAL TECHNIQUES

A substantial component of the initial work to reestablish and characterize the Mach 6 Quiet Tunnel for the study of stability and transition was to establish in the new laboratory capabilities and experiences with a diverse array of experimental diagnostics and supporting equipment. The diagnostics and systems described in this section are not new to the community; the hot-wire anemometry, fast-response pressure transducers, and focused schlieren deflectometry system discussed here have been widely utilized in similar supersonic and hypersonic stability and transition experiments. Nevertheless, it is important to thoroughly describe these first-generation implementations of experimental techniques as now employed in the M6QT, with special attention to their unique strengths (e.g., high SNR, high bandwidth deflectometry) and current weaknesses (e.g., uncalibrated hot-wire measurements).

4.1. Hot-wire anemometry

As the primary diagnostic to be used for the principal goal of the M6QT – the acquisition of well-resolved mean flow and instability profiles for code validation – hot-wire anemometry is discussed first. Basic background on the theory behind the technique is provided, followed by discussion of the present probe design, fabrication and repair techniques, and practical operating procedures. Also discussed in detail are future plans to correct the largest deficiency in the current hot-wire measurements – the lack of calibration and explicit separation of sensitivities to mass flux and total temperature.

4.1.1. Theory

Hot-wire anemometry is a technique which leverages the concept of convective cooling of a heated cylinder to measure flow properties with excellent spatial resolution and frequency response. By using a sufficiently small (micron-sized diameter) wire sensor heated by a high-frequency feedback circuit tuned to compensate for the thermal lag of the sensor, an overall diagnostic frequency response on the order of several hundred kilohertz is attainable, a quality necessary for the study of the second-mode instability in the M6QT.

For the present work, wires are operated in a constant-temperature anemometry (CTA) circuit, whereby the wire temperature (via its resistance) is maintained as a part of a closed-loop feedback circuit. Other anemometry circuit types include constant-current (CCA) and constant-voltage (CVA), but these operate as open-loop amplifiers, correcting for frequency response with a separate fixed-time-constant compensation circuit, which complicates their operation for boundary-layer studies. Kegerise and Spina (2000a, 2000b) present a comprehensive comparison of the static and dynamic responses of the various systems.

The hot-wire sensors themselves typically consist of a length of tungsten or platinum-alloy wire (2.5–5 μm in diameter) attached, either by spot-welding or soft-soldering, to two prong tips separated by 100–300 wire diameters. The wires respond to the mass flux normal to the wire axis, and can be used in a typical ‘straight probe’ configuration, or inclined to the flow in a variety of multiple-wire combinations to allow

for transverse velocity measurements as well. For the present work, the straight-probe design is utilized.

For a straight-probe hot-wire sensor in a general compressible flow, the heat transfer relationship is of the form

$$Nu = f\left(Re_{\mathrm{d}}, Pr, M, \tau, {}^{l}\!/_{d}\right), \tag{4.1}$$

where Nu is the Nusselt number, Re_{d} is the wire-diameter Reynolds number, Pr is the Prandtl number, M is the Mach number, $\tau = (T_w - \eta T_{\mathrm{t}}) / T_{\mathrm{t}}$ is the temperature loading factor (Kovasznay 1950), T_w is the operating wire temperature, T_{t} is the total temperature, $\eta = T_e / T_{\mathrm{t}}$ is the wire recovery factor, and T_e is the wire's equilibrium (or recovery) temperature.

For a constant Prandtl number and sufficiently high-aspect ratio wires (or with corrections for end losses),

$$Nu = f\left(Re_{\mathrm{d}}, M, \tau\right). \tag{4.2}$$

Kovasznay (1950) and others determined that for supersonic Mach numbers, the Mach number dependence on the heat transfer becomes minimal, as does the effect of Mach number on wire recovery factor, η, and therefore also on τ. Thus, for supersonic and hypersonic flows,

$$Nu = f\left(Re_{\mathrm{d}}, \tau\right), \tag{4.3}$$

or, alternatively,

$$Nu = f\left(\rho U, T_{\mathrm{t}}, \tau\right). \tag{4.4}$$

That is, the signal from a hot-wire sensor operated in a hypersonic flow is dependent upon the mass flux, ρU, the total temperature, T_t, and the wire temperature loading factor, τ.

The calibration curve for a hot wire is typically of the form

$$E^2 = L + M\left(\rho U\right)^n, \tag{4.5}$$

where E is the anemometer output voltage, L and M are constants for a given T_t and τ, and n is determined from a best-fit regression of the data. For sufficiently high Re_d, n is often found to be ≈ 0.55. For the present measurements in the flared cone boundary layer, however, $1 < Re_d < 10$, and in preliminary calibration estimates, n is closer to 1.

By calibrating and operating the hot-wire sensor at a number of overheat ratios (or temperature loading factors), it is possible to algorithmically separate the wire's sensitivities to mass flux and total temperature, and thereby produce profiles of mean and dynamic quantities for each.

The present measurements, however, are uncalibrated and wires are operated at a single overheat ratio, $\tau \approx 1$. Smits *et al.* (1983) have shown that for a temperature loading factor in this regime, the wire's dynamic response is primarily sensitive to mass flux, and the effect of total temperature fluctuations is negligible. Thus, the uncalibrated hot-wire measurements presented in Section 6 as profiles of fluctuating anemometer voltage can be seen as representative of fluctuating mass flux, and at least notionally compared with growth in $(\rho U)'$ predicted from computation.

4.1.2. Probe design and fabrication

Custom hot-wire probe bodies and sensors are fabricated and repaired at the M6QT laboratory by the author. The straight probe bodies, loosely following the design used by Kendall (1975), are constructed with a taper created by telescoping several diameters of stainless steel tubing, silver-soldered together. To form the hot-wire prongs, stainless steel botany pins are then fitted into a cylindrical, ceramic insulator pre-drilled at the appropriate separation (nominally 1.2 mm for the current work), and secured with Duralco 4525 high-temperature insulating epoxy. The conductor and shield of a length of low-noise, small-diameter, high-temperature coaxial cabling (Belden 83265) are then each soldered to the aft end of either prong tip, and the junctions are insulated with the same epoxy. Next, the ceramic body is secured inside the stainless steel tubing with again more Duralco epoxy, which is also used to create a conically streamlined forebody at the tip of the probe.

After construction of the probe bodies, the sensor wire is fitted to the prong tips. The sensor wire is a Wollaston wire with a platinum–10% rhodium core of diameter $d = 2.5$ μm. The Wollaston wire is clad in silver of diameter approximately 50 μm. This aids handling and mounting of the wire, making a robust junction to the prongs. To create the sensing element, however, the cladding must be selectively removed from the center of the mounted wire as the last stage of the fabrication process. For the delicate, intricate procedure of mounting and etching the wire, a binocular microscope and custom-built, 14-axis micromanipulator apparatus is used. The process is described in the following text and annotated sequentially in Figure 4–1(*a*)-(*i*).

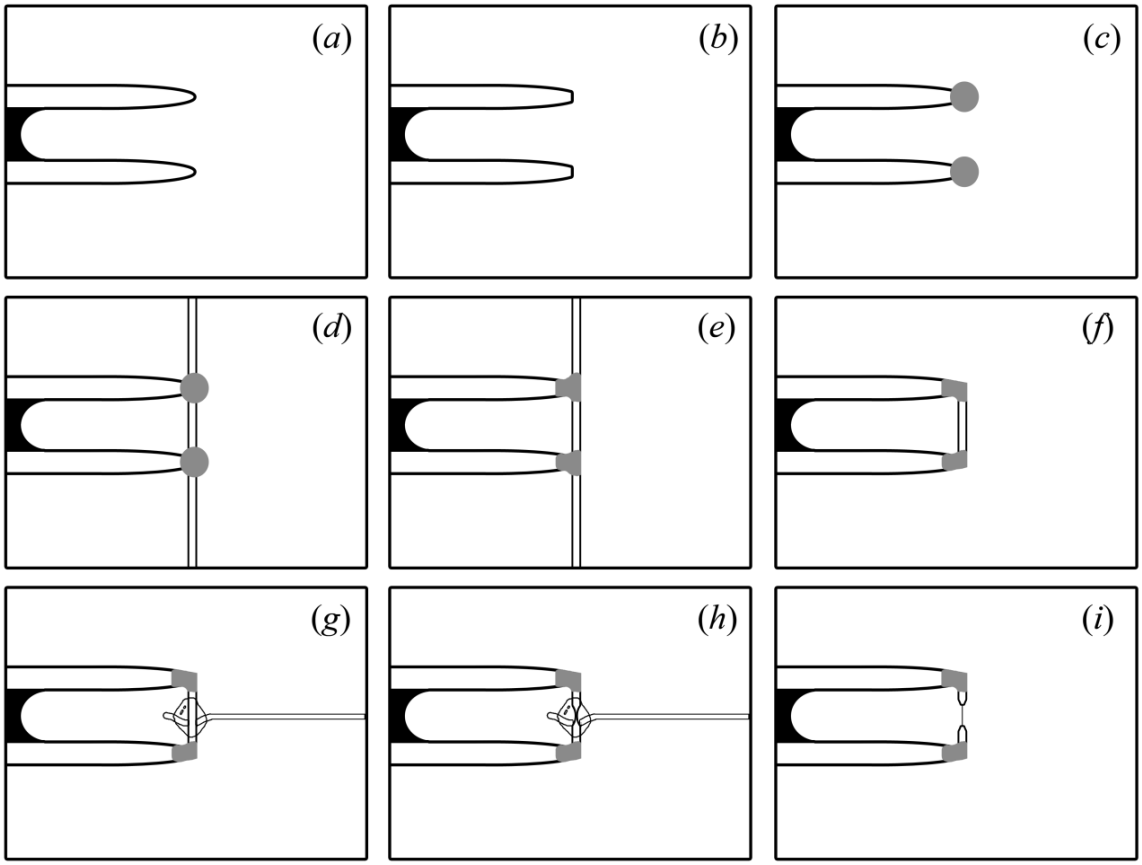

Figure 4–1. Hot-wire probe fabrication process; soft-solder and chemical etch.

To mount the wire, the tips of the botany pins are first lightly sanded to create a flat (Figure 4–1(*a*, *b*)), then cleaned, treated with a phosphoric acid flux, and tinned with a solder with a melting point of 450ºF (well above tunnel operating conditions). Next, a small amount of combination solder–flux paste is added to the prong tips (*c*), and the wire is positioned in place across them (*d*). The prong tips are then carefully and briefly heated with a soldering iron, cleanly securing the Wollaston wire to the prong tips (*e*). Excess Wollaston wire is removed easily (*f*) with a razor blade mounted to the manipulator.

To create the active sensing element, the center portion of the wire's core is exposed via a chemical etching process. Optionally, permanent marker ink may first be applied to the soldered junctions as a mask to protect them should the acid wick to either side of the wire. This solder mask can be removed at the completion of the construction by gently placing the probe in an acetone bath. A drop of dilute nitric acid is applied via surface tension to a miniature nichrome wire hook 25 μm in diameter, and a low-level DC bias voltage is applied between the hook and hot wire. Because the drop of acid evaporates quickly, several applications (*g*–*h*) are required to fully and cleanly expose the proper length of core material (*i*). The wire is etched until its resistance (which monitored continuously) is nominally $R_{20} = 9.0\ \Omega$.

Ideally, the length, *l,* of the active element would be chosen such that its length-to-diameter ratio is approximately 150 to avoid end conduction effects and provide adequate sensitivity, and the wire mounted with slack to avoid strain-gaging effects (Kovasznay 1953, Smits *et al.* 1983, Smits & Dussauge 1989). In the interest of sensor robustness, anemometer tuning, and ease of construction for the present work, the wires were etched such that the element *l/d* ratio was only 100, and the wire was mounted without appreciable slack. As expected, strain-gaging effects may indeed be visible in the results (§6.4).

For a representative completed sensor assembly, see Figure 4–2.

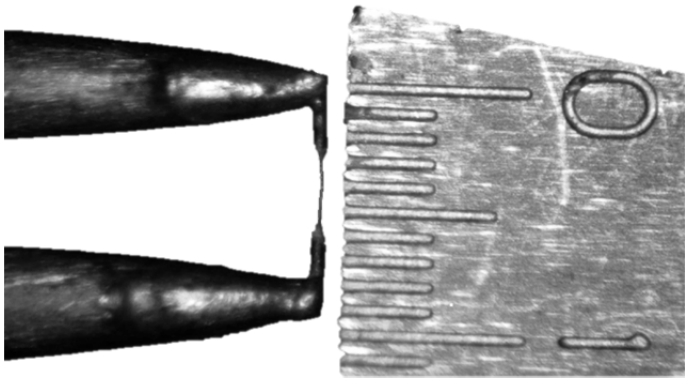

Figure 4–2. Hot-wire probe with soft-soldered Wollaston wire construction. Active element is Pt-10%Rh material 2.5 μm in diameter, with an active-element $l/d \approx 100$. Shown for scale is a 1 mm rule.

4.1.3. Operational procedure

Because the M6QT run time is limited to 40 seconds, special care must be taken with regard to the procedures by which the manually-adjusted A.A. Lab Systems AN-1003 hot-wire anemometer is tuned and operated during a measurement campaign. Due to the limited run time – and even for uncalibrated wires – multiple runs must be used in order to optimize the wire frequency response at flow conditions and prepare the gain and offset on the amplifier for proper data collection.

After a wire has been constructed and annealed, it is installed into the tunnel test section and mounted to the traversing mechanism as per Section 3.2.3 or 3.2.4. Next, a motion program is manually configured which sets an array of points between 0.25 and 4 mm from the model surface at the desired axial location. The tunnel is then preheated subsonically, during which time a conservative tuning balance is set on the anemometer to ensure stable operation during the full hypersonic run. When the run begins, a full boundary-layer profile is acquired normally in order to determine the height in the

motion program that corresponds to the location of maximum RMS fluctuation. During a second run, the wire is placed directly in this maximum RMS location for the full duration of the run, so that bridge tuning can be specifically optimized using square wave injection at test conditions. Here, the impulse input and wire response are each recorded using a PC-based oscilloscope, and analyzed to determine the frequency–amplitude transfer function. A –3 dB rolloff at 333 kHz, consistent with a pulse-response time constant of 2.5 μs, was seen for the wires used in the campaign presented in Section 6.

For runs subsequent to the tuning run(s), the tuning, gain, and offset settings on the anemometer are fixed and the wire can be operated at other axial locations immediately.

For protection against wire breakage during the tunnel start and unstart processes, the hot-wire probe is initially parked just behind the base of the cone model, it emerges once flow is established, and returns to a location behind base of the cone prior to tunnel shutdown. Additionally (or, alternatively, for fixed probe setups as per Section 3.2.4) the tunnel run is initiated with the anemometer circuit in 'neutral' mode, disabling the active feedback circuit and preventing a thermally-induced wire breakage caused by an overshoot in the circuit response to a starting shock. Once the tunnel flow is established, the feedback circuit is switched into the 'operate' mode. Similarly, the anemometer is returned to 'neutral' mode before the end of a tunnel run.

At the completion of a measurement series (or when a wire breaks), the wall is found in the traverse coordinate system at each axial location by carefully seeking

electrical continuity between the prong tips and the model surface (as was described further in Section 3.2.5). It is only then that actual wall-normal distances are known. To automate this process in the future, new probe bodies may employ a fouling wire offset a known distance from the prong tips, with wall-finding circuitry integrated into the traverse controller, as was originally done by Lachowicz (1995).

Hot-wire data are low-pass filtered at 500 kHz for antialiasing using an 8-pole Butterworth filter and sampled at 1 MHz, with a 100–250 ms residence time at each location within the boundary layer.

4.1.4. Regarding sensor calibration

Unfortunately, for the hot-wire anemometry work presented in Section 6, the data remain uncalibrated. However, even in the absence of a rigorous calibration and proper separation of sensitivities to mass flux and total temperature, valuable conclusions can still be drawn. Operated at a high overheat ratio ($\tau \sim 1$), the wire is primarily sensitive to mass flux, and total temperature contributions can effectively be ignored. In these data, frequencies of most-amplified instabilities can be readily identified, and from several profiles obtained with a single wire operated at the same conditions, relative instability growth can be observed and at least qualitatively compared with computation. However, it is acknowledged that without a proper calibration procedure, the hot-wire data obtained in the M6QT cannot comprehensively, quantitatively be used for their stated purpose of providing validation for stability computations. This section describes the

current plans to implement a proper hot-wire calibration procedure at the M6QT in support of this goal.

Reasons for the present lack of calibration are varied. The earliest efforts with custom-fabricated probes encountered robustness issues; typical hot wires of the design used for the data of Section 6 would last only six or seven runs, at best. Operating with this constraint makes the inclusion of a number of calibration runs difficult. Later, techniques for improving the wire longevity were discovered (e.g., probe shielding, keeping CTA circuit in idle until flow established, etc.), and this became less of an issue.

Second, the mass flux conditions in the flared cone boundary layer – after the compressions imposed by the cone shock and the flare itself – are considerably higher (at 80 kg/m^{2}s) than those achievable in the M6QT freestream (≈ 38 kg/m^{2}s). The smaller, Mach 5 facility at the laboratory operates at temperatures too low (370 K) and mass fluxes too high (200 kg/m^{2}s), and thus no facility at the laboratory is suitable for the calibration of M6QT hot wires in the freestream, at least without significant extrapolation. A new, small Mach 4 facility (40 mm exit diameter nozzle) that matches the M6QT's total temperature condition of T_{t1} = 430 K would make an ideal dedicated hot-wire calibration facility, but appropriately-sized heating and vacuum provisions are not currently available at the TAMU NAL, and so the time and cost to establish this capability would be prohibitive.

For his work on a 7º sharp cone in the Langley M3.5 SLDT, Matlis (2003) encountered similar limitations on the ability to calibrate in the tunnel freestream, and so developed a novel in-situ calibration method to calibrate a hot wire operated in CCA

mode in the cone boundary layer during a profile acquisition. Here, a Pitot pressure profile is first taken along with a surface static pressure measurement to yield a Mach number profile. Next, a multiple-overheat hot-wire profile is taken (including cold-wire measurements to obtain T_t) at the same location. The Pitot and static pressure measurements, together with the experimental T_t profile, yield known profiles of mass flux and total temperature against which the multiple-overheat hot-wire profile can be calibrated. A similar procedure could be employed in the M6QT, save for substantial difficulty obtaining a proper static pressure measurement on the model in a nominal 30 second run time. An alternative would be to utilize a computed Mach number profile in its place, but this introduces additional uncertainty. With a limited number of short runs available per day, this procedure as applied in the M6QT could have taken as long as several days to calibrate and use a single hot wire, assuming no wire breakage. Thus, a more efficient solution was desired.

For this, we return to the idea of calibrating several wires at once in the M6QT freestream. In order to extend the range of mass flux available for hot-wire calibration, a simple wedge model is currently being designed. A wedge with half-angle of 10º will yield a mass flux in the shock layer of up to 90 kg/m^{2}s at p_{t1} = 145 psia, sufficient to match the maximum expected conditions on the current 93–10 flared cone as well as future crossflow and transient growth experiments. The wedge will be sized to enable the simultaneous calibration of at least five hot-wire probes, and will incorporate Kulite pressure sensors to accurately determine the aerodynamic wedge angle.

Although this calibration method requires a dedicated model setup in the test section, a large number of hot-wire probes can be calibrated in a small number of runs in preparation for a measurement campaign. Calibration data will be obtained as p_{t1} is varied to produce a range of mass flux conditions during a single run, and multiple overheat ratios will applied to the sensors in sequence in order to generate the matrix of data required to separate mass-flux and total-temperature sensitivities.

In order to enable the efficient acquisition of these data at multiple overheat ratios, several channels of the anemometer have been substantially modified by the author to accept a computer-controlled overheat ratio scanner, similar to that employed by Bowersox (1992). The AN-1003's internal resistance decade was removed from the channel and installed into an external enclosure that also houses 8 additional fixed resistors. The adjustable decade resistor serves to define the maximum overheat ratio, and the 8 fixed resistors are iteratively placed in parallel with the decade by means of reed relays fired by a Berkeley Nucleonics Model 575 Pulse / Delay generator. The pulse generator is itself triggered by the LabVIEW motion program (§3.2.1) such that the range of overheat ratios is scanned at each point in the boundary layer. The relays are fired in a "make-before-break" configuration and all additional resistances are in parallel with the maximum resistance such that the sensor does not see any unexpectedly high overheat ratios. As is to be expected, the tuning of the feedback circuit degrades at lower overheat ratios (longer time constants), but this effect is minimized through careful design of the setup and additional optimizations are in progress.

4.2. Fast-response pressure measurement

4.2.1. Kulite pressure transducers

For freestream Pitot-pressure measurements, Kulite fast-response pressure transducers were used. These devices are strain-gage sensors with small cylindrical bodies and miniature (≈ 1 mm square), thin sensing elements on a silicon diaphragm. The miniature size and low mass of the sensing element yields a fast response and very high natural frequencies, O(150 kHz). The transfer function of the sensor's dynamic response is typically flat from DC through at least 30% of the sensor's natural frequency, typically ≈ 50 kHz. The devices are rated and compensated for a range of temperatures appropriate for operation in the M6QT, although there remains a slight variation in the zero-offset of the calibration with actual sensor temperature, so static calibrations must be performed as close to operating temperature as possible.

For most of the work presented in Section 5, a miniature Kulite XCEL-100-series pressure transducer was flush-mounted in the tapered tip of a stainless steel rod, which itself was fixed to the two-axis traversing mechanism mounted to the interior ceiling of the test enclosure as described in Section 3.2.2. The Kulite transducer had an absolute full-scale range of 0.7 bar absolute [10 psia], a body diameter of 2.57 mm [0.101″], a "B" screen, and a nominal resonant frequency of 150 kHz.

The 10V DC supply power to the transducer and the initial amplification of its 100 millivolt full-scale output signal was provided by an Endevco Model 136 signal conditioner. Acquisition of the full-scale output signal was performed using a National Instruments 16-bit data acquisition system, sampling at 250 kHz. This preamplified

signal was also sent to a Stanford Research SR560 low-noise filter unit, AC coupled, and further amplified within a passband of 1 kHz to 100 kHz for better analog-to-digital (A/D) resolution when measuring the small fluctuations (< 0.1%) present in the quiet flow test area. Unfortunately, it was found that the Endevco Model 136 introduces a broad band of electronic noise in the range of 20–50 kHz. It is believed that this noise is introduced due to the use of a switching-type DC power supply in the Model 136 unit.

Later Kulite work employed a custom signal-conditioning circuit designed by personnel of the Boeing/AFOSR Mach 6 Quiet Tunnel (BAM6QT) at Purdue University. This uses a linear DC power supply, a series of INA163 low-noise instrumentation amplifier components, and simple RC filters to amplify the Kulite signal's DC and AC components independently with minimal electronic noise.

The particular signal conditioning equipment selected for each data set will be specified along with the results in Section 5.

4.2.2. PCB piezoelectric pressure sensors

As a complement to the Kulite pressure sensors described above, a PCB® 132A31 piezoelectric pressure sensor is employed. Like the Kulite, this sensor has a cylindrical body (3.2 mm diameter) and an *O*(1 mm) active sensing area. However, unlike the Kulite's strain-gage design, the PCB's sensing element is piezoelectric in nature, driven by a constant current and acting as a source follower. The nature of the PCB's design gives it an extremely frequency response (up to 1 MHz), but does not support measurement of DC pressures; the output signal is high-pass filtered at 10 kHz.

PCB piezoelectric pressure sensors of this type are typically used as simple time-of-arrival sensors in shock tubes, although recently they have been employed with some success for the measurement of second-mode instability waves (Berridge 2010, Berridge *et al.* 2010). Because they are typically used only to measure time-of-arrival, the manufacturer supplies only a single-point sensitivity (nominally 140 mV/psi) and the actual frequency response transfer function is unknown; calibration for instability measurement remains a major challenge. Berridge is currently working to characterize these sensors using weak, thin shock waves in a shock tube (Abney *et al.* 2013). Another possible calibration method is to use ultrasonic transducers to sweep a range of frequencies at controlled amplitude levels.

For the work presented in Section 5.4, however, PCB® sensors are not used for measurement of the second-mode instability, but rather to augment the Kulite freestream measurements by providing a higher-bandwidth perspective of Pitot pressure fluctuations in the quiet and noisy modes. The PCB® sensor is mounted in the same tapered stainless-steel Pitot probe as the Kulite described above, and similarly mounted to the traversing mechanism. The sensor is driven by a PCB® 482C05 signal conditioner, which provides a constant 4 mA current to the sensor and returns its full-bandwidth (1 MHz) signal with unity gain. A Stanford Research Systems SR560 provides filtering at 1 MHz, and a gain of 50. Data acquisition is performed with a National Instruments 16-bit USB-6255 DAQ board, this time sampling at 2 MHz.

4.3. Focusing schlieren deflectometry

Originally configured and implemented in the M6QT merely as a simple, inexpensive way to verify hot-wire measurements, the focused schlieren deflectometer described below quickly proved to be a uniquely robust and valuable independent diagnostic for the study of second-mode instabilities, with its own distinct advantages, including a frequency response which far exceeds that of the hot wire.

4.3.1. Background

A focusing schlieren system is similar to the classical schlieren system in that it provides visualization of density gradients in a flowfield as light and dark areas in an image by leveraging the variation in refractive index, selectively cutting off those light rays which are bent by flow disturbances using an opaque knife-edge. It has the additional distinction, however, of being only sensitive to these changes in a single narrow plane of interest, whereas classical schlieren diagnostics respond across the entire optical path, producing an image of integrated flowfield variation. Focusing schlieren systems were first conceived during the mid-20th century (Schardin 1942; Burton 1949; Kantrowitz & Trimpi 1950; Fish & Parnham 1950) and steadily improved until Weinstein (1993) wrote a guide to the modern lens-and-grid type focusing schlieren system, schematically shown using his nomenclature in Figure 4–3. There are several variations of focusing schlieren systems; the system implemented for this work is of the lens-and-grid type. Classically, this type of system consists of an extended light source, two grids, and a lens. Boedeker (1959) added a Fresnel lens after the light source in

order to dramatically improve the image brightness. The source and cutoff grids are sets of alternating opaque and clear stripes, and are photographic negatives of each other. In this way, each pair of source and cutoff stripes function as the slit-source of light and knife edge cutoff of a conventional schlieren system. The system as a whole can be thought of as superposition of many conventional schlieren systems, with each clear stripe of the source grid and corresponding opaque stripe of the cutoff grid functioning as the light source and knife edge, respectively. This, along with a large lens aperture and non-collimated light path, lend the system its focusing ability.

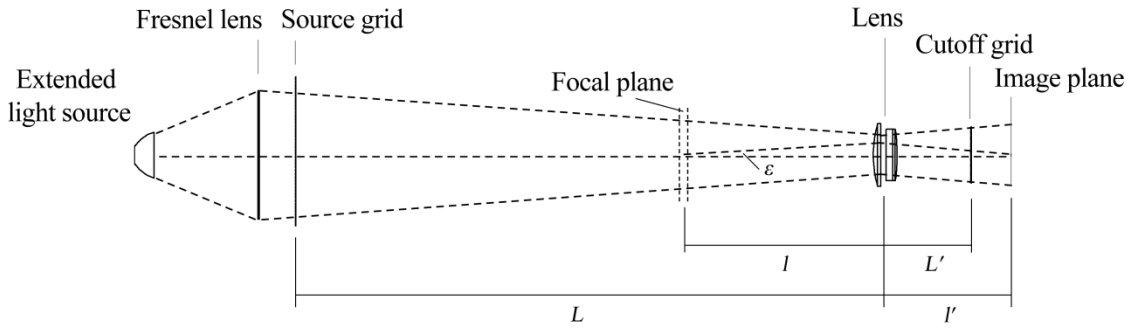

Figure 4–3. Basic schematic layout of a lens-grid type focusing schlieren apparatus. Variables follow the nomenclature of Weinstein (1993).

The shallow depth of field of the lens-grid focused schlieren system is particularly beneficial for use in the Mach 6 Quiet Tunnel. Because the M6QT operates as an enclosed free jet, a shear layer aft of the nozzle exit surrounds the optically-accessible portions of the model. While conventional schlieren systems are equally as sensitive to flow structures in these regions as they are to the instabilities on the cone

model, a focused schlieren system with a sufficiently limited focal depth is immune to these shear layers (and other out-of-plane schlieren like window defects), and therefore maximizes signal-to-noise ratio for the instabilities of interest. The focusing schlieren system is also relatively compact and well-suited to the limited laboratory space available surrounding the M6QT.

For fixed locations of the source and cutoff grids relative to the lens (distances L and L'), a focal plane location (distance l from the lens) can be chosen by selection of the image plane at distance l' from the lens. At the image plane, one may place a screen or camera and use a high-intensity pulsed light source for high-speed imaging. Alternatively, one may use the focused schlieren setup for high-bandwidth deflectometry, as is done for the present work. In this configuration, a constant light source is used, and a fiber optic is precisely placed in the image plane to correspond to a particular physical location in the focal plane. The fiber optic is then coupled to a high-bandwidth photodetector, enabling acquisition of time series of light intensity, and therefore, spectra of density fluctuations at a point in the image. VanDercreek (2010) applied this technique using a photomultiplier tube for the study of the second-mode instability on a 7-degree straight cone at Mach 10 in Tunnel 9 at Arnold Engineering Development Center (AEDC). VanDercreek observed in the photomultiplier signal frequencies consistent with those measured with PCB® pressure sensors embedded in the model surface. The present work employs an avalanche photodetector in a similar capacity.

For a full analytical description of the lens-and-grid focused schlieren system sizing and performance, together with practical implementation guidance, see Weinstein (1993). The apparatus as specifically configured and implemented for the present experiments is described in the context of Weinstein's parameters below.

4.3.2. Implementation

Using the design guidance and analysis provided by Weinstein (1993), a lens-and-grid focused schlieren system was configured and built specifically for use in the M6QT. Primary design goals were to obtain a focal depth less than 25 mm and a field of view of at least 25-50 mm, with maximum practical sensitivity and an overall system footprint suited to the spatial constraints of the M6QT laboratory.

The resulting system design is depicted below in Figure 4–4, shown to scale and accompanied by a cross-section of the M6QT test section, nozzle, and flared cone model.

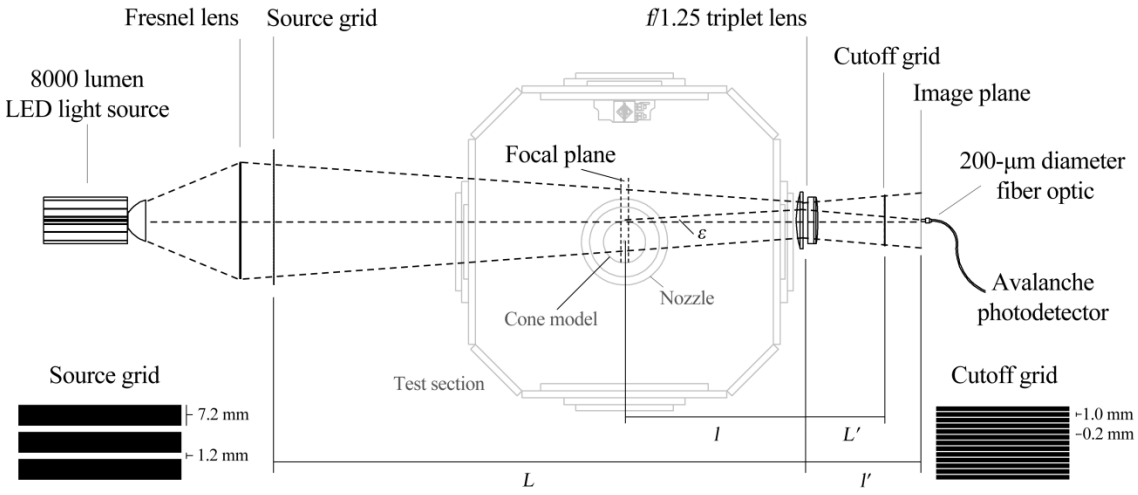

Figure 4–4. Detailed schematic of focused schlieren apparatus in M6QT.

Table 4–1 gives the chosen values for the key geometric parameters of the system as well as two measures of the focal depth performance. The depth of sharp focus, *DS*, is defined by Weinstein as

$$DS = 2\frac{l}{A}w, \tag{4.6}$$

where l is the distance from the lens to the object plane, A is the diameter of the lens aperture, and w is the resolution limit of the image due to the grid geometry and image magnification. Replacing this length scale with a chosen length scale for the flowfield of interest (here, the ≈ 3 mm wavelength of the second-mode instability), a depth of "unsharp" focus is defined as

$$DU = 6\frac{l}{A}\ \text{mm}. \tag{4.7}$$

Table 4–1. Key configuration parameters for focused schlieren apparatus.

Parameter	Description	Value
A	Lens aperture diameter	155 mm
f	Lens focal length	195 mm
L	Distance from lens to source grid	1444 mm
L'	Distance from lens to cutoff grid	221 mm
l	Distance from lens to object plane	530 mm
l'	Distance from lens to image plane	308 mm
DS	Depth of sharp focus	0.97 mm
DU	Depth of unsharp focus (for 3 mm structure)	21 mm

In the present implementation, the extended light source is a Bridgelux C8000LM high-power, 8000-lumen LED array driven with 3.0A current at 30.5V using a 95W Mean Well CEN-100 constant-current LED driver. The LED array is mounted to a large heat sink and surrounded by a shaped reflector to maximize light delivered to the system. The Fresnel lens is 317 mm in diameter with a 213 mm focal length.

Classically, source and cutoff grids for focused schlieren systems are manufactured from photographic film, and one is exposed to be the negative of the other. However, for simplicity in this initial configuration of the system, both the cutoff and source grids were printed on ordinary transparency film using a black-and-white laser printer from Adobe Photoshop source files. Special care was taken to maximize the opacity of the printed grid lines using the printer's contrast and brightness controls, and to maximize the sharpness of the lines by matching the source files' resolution to the printer's native resolution. To increase the signal-to-noise ratio by maximizing the opacity of the source grid, this grid is actually comprised of three layers of printed

transparency, superposed. The cutoff grid, although otherwise fabricated in the same way, is only a single layer of transparency film, for best alignment. The opaque lines of the cutoff grid are thicker than they would be as a photographic negative of the source – this further improves signal-to-noise ratio by additionally cutting off unwanted residual light that bleeds through the opaque regions of the source grid.

The lens is a three-element achromat 155 mm in diameter with a 195 mm focal length (*f*/1.25). The cutoff grid is mounted on a series of fine-resolution kinematics which allow for precision adjustment in the axial direction (for focus), tilt on two axes (for grid alignment), and vertical motion (for cutoff adjustment). Adjustment of the grids is performed by backlighting the cutoff grid from behind the image plane, and aligning its projection onto the source grid, ensuring proper magnification, focus, alignment, and cutoff.

Before installation in the M6QT, the focused schlieren system was briefly characterized on the bench. Figure 4–5 below shows a simple test of the system's depth-of-field and sensitivity. A camera was placed in the image plane, and two compressed air jets were placed in the optical path, separated by 12 mm along the optical path axis. In Figure 4–5*(a)*, the horizontal jet is in the plane of sharp focus, whereas in Figure 4–5*(b)*, the jets have been displaced such that the diagonal jet is instead in the plane of sharp focus. In each case, the jet which is out-of-plane by only 12 mm is out of focus, with no visible small scale structures.

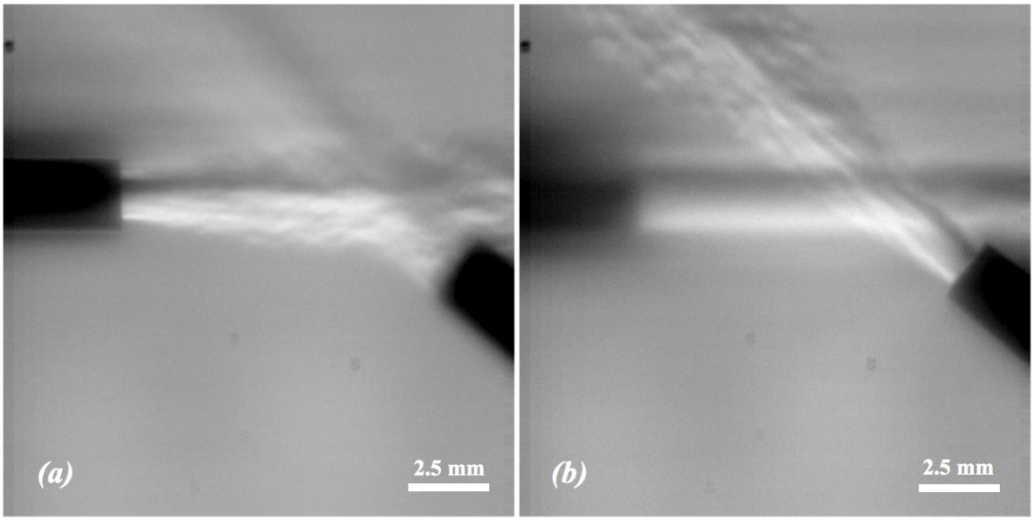

Figure 4–5. A bench test of the focal depth of the focused schlieren system. Two jets of compressed air are placed in the optical path, separated by 12 mm along the axis of the optical setup, and imaged with a high-speed camera in the image plane. In (a), the horizontal jet is in the plane of sharp focus. In (b), the diagonal jet is in the plane of sharp focus. Note the lack of small-scale flow detail in the out-of-plane jet.

Figure 4–6 shows a depiction of the optical access available in the M6QT facility and how it is utilized for the present experiments. High-quality dual surface optical flats mounted in the test section walls provide optical access through an aperture 190 mm in diameter, within which the nozzle exit and base of the cone are visible. Within this available optical pathway, the focused schlieren apparatus is positioned to select an effective field of view approximately 40 mm in diameter. For these experiments, the field of view is selected to be at the base of the upper surface of the cone, as shown in Figure 4–6. The fiber optic is positioned in the image plane such that its location in the cone boundary layer corresponds to an axial station, $X_c = 495$ mm, and mean height of approximately 1.3 mm, previously observed to be the height of maximum instability

amplitude for zero angle of attack. This height is adjusted as necessary for best measurement of leeward and windward conditions.

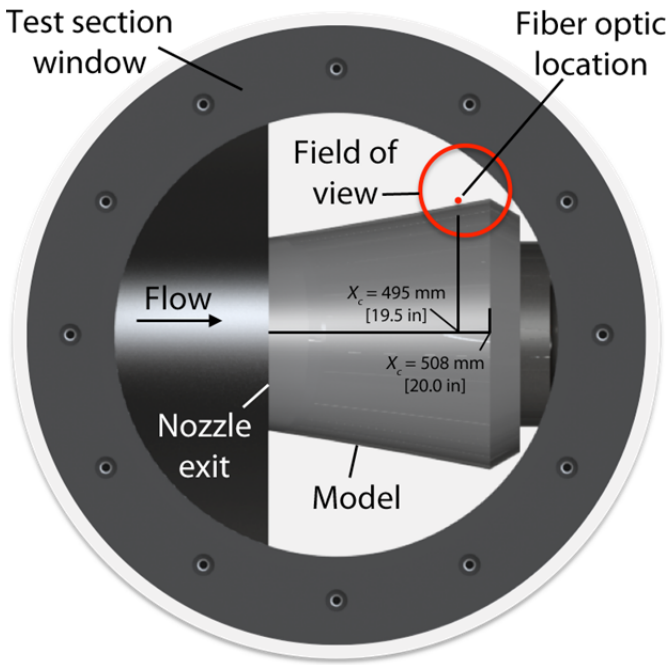

Figure 4–6. A schematic of the optical access available in the M6QT. Depicted is the field of view of the optical system and effective location of the fiber optic as placed for boundary-layer measurements shown (X_c = 495 mm).

The fiber optic is then coupled to a Thor Labs APD110A avalanche photodetector, which offers a voltage output with high sensitivity and a bandwidth of 50 MHz. The signal from the photodetector is fed to a Stanford Research Systems SR560 signal conditioner, amplified by a factor of 50, and bandpass filtered from 1 kHz to 1 MHz (–6 dB/decade). Both the raw and filtered/amplified signals are acquired during the run at a sampling rate of 2 MHz.

5. FREESTREAM FLOW QUALITY CHARACTERIZATION

5.1. Overview

Following successful initial shakedown testing of the Mach 6 Quiet Tunnel within the infrastructure of the TAMU NAL and the subsequent nozzle repolishing effort, the first experimental priority was to conduct a thorough survey of the quiet flow performance of the nozzle. Through comparison to the previously-reported performance of the facility as installed at NASA Langley, the suitability of the facility to perform similar stability and transition experiments can be established, and context for comparison of current and past experiments can be provided. Additionally, the present measurements of the details of the flow environment, including mean quantities as well as disturbance amplitudes and spectra, can be incorporated into modern simulations as initial conditions.

Several techniques were employed in the freestream characterization efforts described in the sections below. Spatial surveys of mean and fluctuating pressure from a Kulite pressure sensor mounted in the Pitot configuration provide insight into the spatial uniformity of freestream Mach number and the spatial extent and spectral character of the quiet test environment at two key unit Reynolds numbers. Additionally, the same Kulite sensor was held at several fixed points along the centerline during continuous sweeps across unit Reynolds number conditions in order to more completely understand the process by which quiet flow is lost in the nozzle with increasing Reynolds number. Finally, a PCB piezoelectric pressure sensor with substantially higher bandwidth was

employed in a similar fashion to characterize the evolution of the spectral character of the disturbance environment with unit Reynolds number with the nozzle bleed valves either closed (BVC; noisy mode) or open (BVO; quiet mode).

Whenever appropriate, the data below are presented with comparison to historical results and with discussion as to the suitability of the present test environment for stability and transition experiments. All data presented below were taken subsequent to the nozzle repolishing effort described in Section 2.

5.2. Mach number uniformity and spatial quiet flow maps at select *Re*

In order to map the extent of the quiet test core of the M6QT, spatial scans of Mach number uniformity and fluctuating Pitot pressure were acquired. For this study, a Kulite XCEL-152-10A transducer was mounted to the two-axis traversing mechanism in the Pitot configuration per Figure 3–5(*b*) and systematically maneuvered throughout the tunnel freestream over a series of runs. Within each 30- to 40-second tunnel run, dynamic Pitot pressure data were acquired at 20 to 24 locations within the ground-parallel center plane of the nozzle. At each location, the raw and amplified, filtered Kulite data were sampled at 1 MHz for 100 ms. Data from six successive runs at identical run conditions were concatenated to form complete contours of Mach number and noise level within the aft half of the nozzle. This procedure was repeated for two key test conditions, which are summarized in Table 5–1.

Table 5–1. Nominal run conditions for spatial scans of freestream M and $\tilde{p}_{t2}/\overline{p}_{t2}$.

Parameter	Condition 1	Condition 2
Nominal M	5.9	5.9
p_{t1}	710 kPa [103 psia]	917 kPa [133 psia]
T_{t1}	430 K [314 °F]	430 K [314 °F]
Re	7.9×10^6/m [2.4×10^6/ft]	10.2×10^6/m [3.1×10^6/ft]

Figure 5–1 presents Mach number contours at these two key conditions. Nominal tunnel Mach number is first achieved on the nozzle centerline at approximately $X_0/L = 0.5$. The most-upstream tip of the nominally Mach 6 flow region is relatively blunted, approximately 2-3 cm in width. Just downstream, near $X/L = 0.62$, a region of locally higher Mach number is present, approximately 1.5% higher than average Mach numbers in the majority of the nozzle flowfield. The blunted onset of the uniform flow region and subsequent overshoot in Mach number is consistent with the 1997 observations of Blanchard *et al.*, who suggested this was due to errors in the coupled inviscid and boundary-layer codes used to initially design the nozzle contour.

A direct comparison with the center-plane Mach number contours of Blanchard *et al.* is presented in Figure 5–2 for both $Re = 8\times10^6$ m^{-1} and 10×10^6 m^{-1}. Although the current data were taken at a lower spatial resolution than Blanchard's data, yielding more jagged contours, a striking similarity in the character of the Mach contours is evident. Indeed, after the relocation and reinstallation of the facility and repolishing of the nozzle, the character of the freestream Mach number contours remain largely unchanged. The blunted upstream tip of the uniform flow region on the centerline, the subsequent overshoot in Mach number near $X/L = 0.62$, and even two opposing lobes of

high Mach number near X/L = 0.75 can still be discerned in the present results. Note that the present data globally show slightly lower Mach numbers (by nominally 0.05) than the 1997 data. This is considered to be within the levels of measurement uncertainty since, for example, the effect of Kulite sensor temperature on its zero offset was not explicitly accounted for in the static calibration.

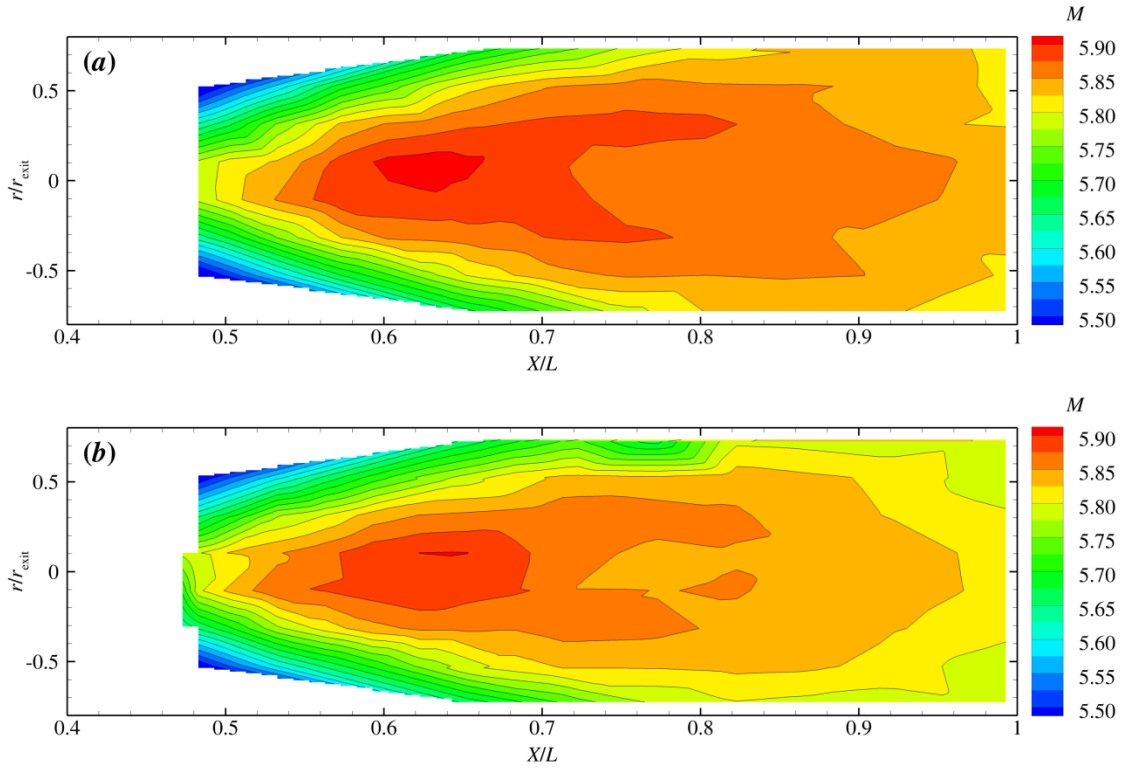

Figure 5–1. Contours of freestream Mach number, M. Freestream conditions are (*a*) $Re = 7.9\times10^6$ m^{-1} and (*b*) $Re = 10.2\times10^6$ m^{-1}.

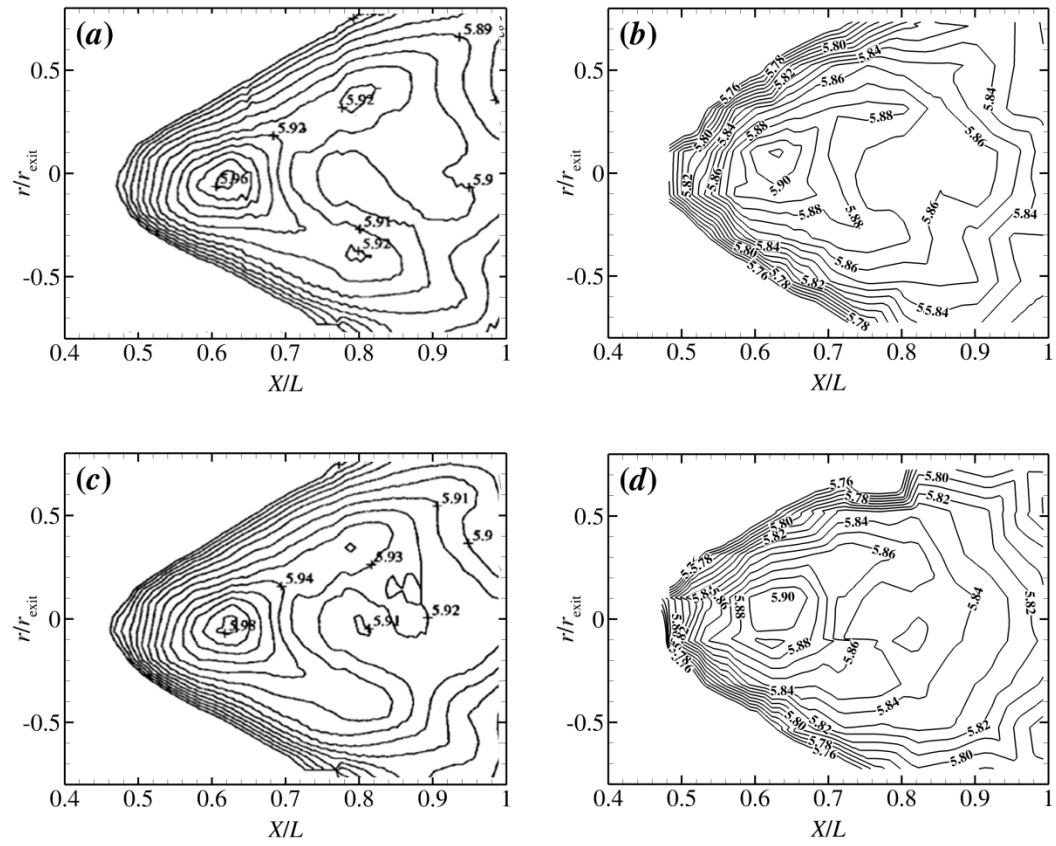

Figure 5–2. Contours of freestream Mach number versus Blanchard *et al.* (1997). Subfigures (*a*) and (*c*) show the data from the NASA Langley experiments at $Re = 8\times10^6$ m^{-1} and $Re = 10\times10^6$ m^{-1}, respectively. Subfigures (*b*) and (*d*) show the current data set for $Re = 7.9\times10^6$ m^{-1} and $Re = 10.2\times10^6$ m^{-1}, respectively.

Freestream noise contours are presented in Figure 5–3 again for both unit Reynolds number conditions. In both cases, a large region of nominally low-disturbance flow is observed, bounded downstream by the acoustic disturbances radiating into the flow along Mach lines which originate at transition of the nozzle boundary layer. Along the centerline, freestream noise begins below the electronic noise floor of the sensor at 0.05%, and gradually increases to 0.5% RMS at the centerline of the exit plane. Using as a threshold the Mach line along which the freestream fluctuations are 1% (where the

noise *gradient* is highest), the nozzle-wall transition location, $X_{T,W}$, was determined by extrapolation outside the scanned area to be at approximately $X_{T,W}/L = 0.7$ for $Re = 8\times10^6$ m^{-1}, moving forward to $X_{T,W}/L = 0.6$ for $Re = 10\times10^6$ m^{-1}.

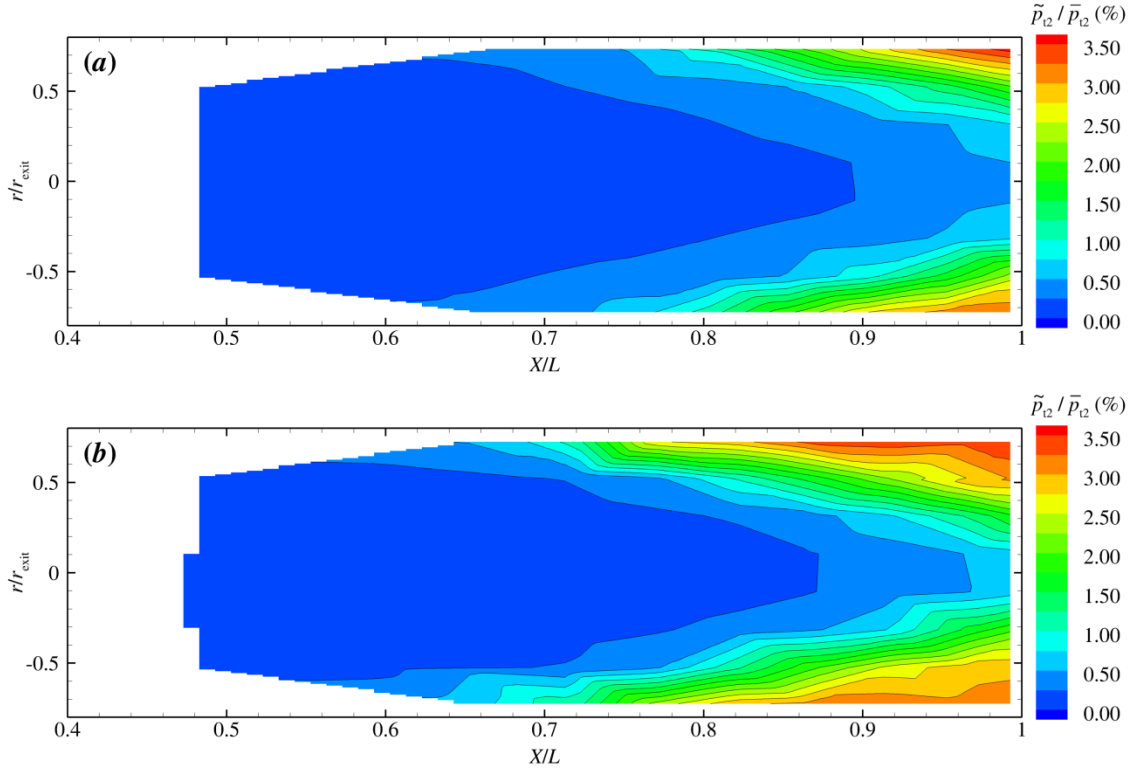

Figure 5–3. Contours of normalized freestream RMS Pitot pressure, $\tilde{p}_{t2}/\bar{p}_{t2}$. Freestream conditions are (*a*) $Re = 7.9\times10^6$ m^{-1} and (*b*) $Re = 10.2\times10^6$ m^{-1}.

Extrapolating this line aft of the exit to determine the downstream extent of quiet flow on the centerline of the nozzle, $X_{T,C}$, the quiet test core length, $\Delta X = X_{T,C} - X_0$, can be approximated and cast in terms of a quiet core length Reynolds number $Re_{\Delta X}$. In Figure 5–4, the current quiet core length Reynolds numbers are plotted against the historical data published by Chen *et al.* in 1993 (prior to an electroplating of the nozzle

interior) and by Blanchard in 1997 (after the electroplating effort and subsequent repair), together with theoretical expectation based on an *N*-factor for the Görtler instability of 7.5 at transition. Although the trend and values appear to agree quite well with Blanchard's data, it must be noted that Blanchard characterized the extent of the quiet core based simply on the location at which uncalibrated hot-wire voltage fluctuations exceeded his electronic noise floor, and since this level is unknown and is not reproducible, it is unlikely that the two chosen thresholds for quiet flow extent are identical.

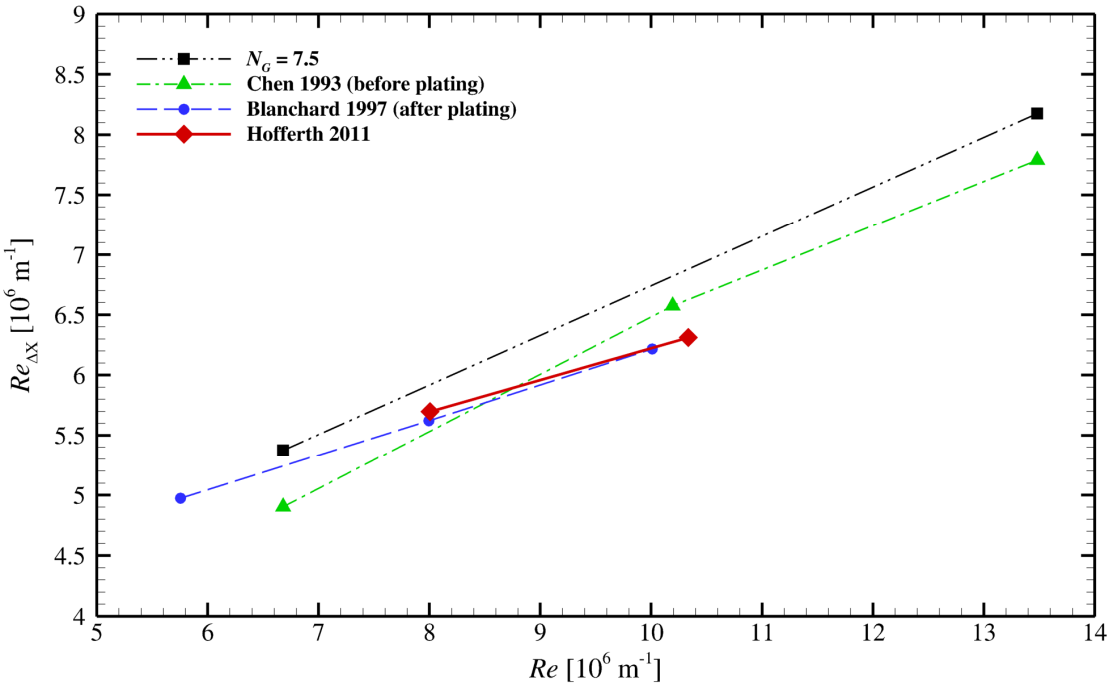

Figure 5–4. Quiet core length Reynolds number, $Re_{\Delta X}$, versus freestream *Re*. Shown for comparison are data from the M6QT's former installation at NASA Langley, as well as the design prediction based on a nozzle-wall Görtler number N_G = 7.5.

Finally, Figure 5–5 and Figure 5–6 show the spatial evolution of the spectral content of the freestream noise at $Re = 8\times10^6$ m^{-1} and 10×10^6 m^{-1}, respectively. Power spectra are computed using Welch's method (Hamming window, 50% overlap, 2000 points per window, sampling frequency of 1 MHz), and are displayed versus X/L for each of four distinct lateral locations in subfigures (*a*)–(*d*). The signal has been low-pass filtered at 100 kHz, but is only shown to 60 kHz, as frequencies higher than this may be affected by the sensor's resonant frequency of 150 kHz.

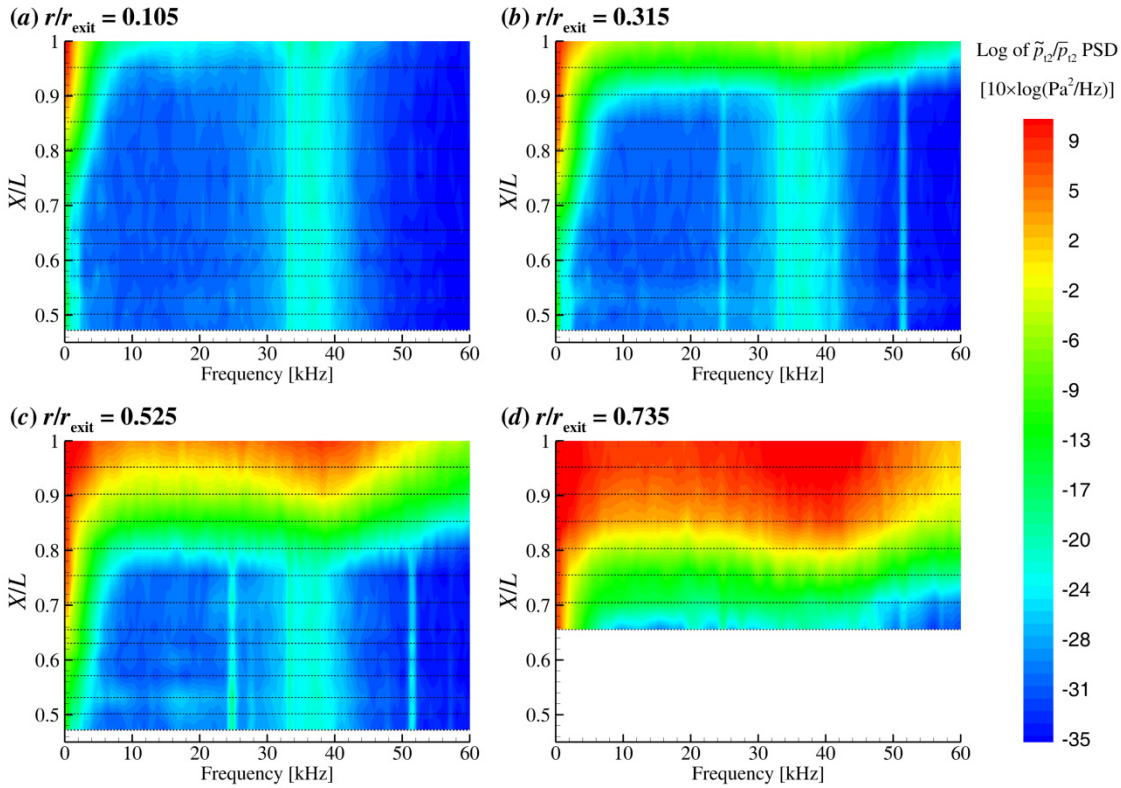

Figure 5–5. Spatial evolution of freestream noise spectra for $Re = 8\times10^6$ m^{-1}. Shown are contours of the log of the amplitude of the power spectral density of $\tilde{p}_{t2}/\bar{p}_{t2}$ for (*a*) $r/r_{exit} = 0.105$, (*b*) $r/r_{exit} = 0.315$, (*c*) $r/r_{exit} = 0.525$, and (*d*) $r/r_{exit} = 0.735$. Dashed lines indicate the discrete X/L locations at which the data were taken.

Note that in those portions of the figures which show a nominally quiet flow, a substantial amount of electronic noise is present, in particular at 25 kHz, 52 kHz, and a broad band of frequencies between 32 and 42 kHz. These are present in a flow-off electronic noise floor test as well, and represent noise introduced by the switching power supply of the Endevco Model 136 signal conditioner. This noise does not contribute significantly to the RMS noise measurements presented earlier.

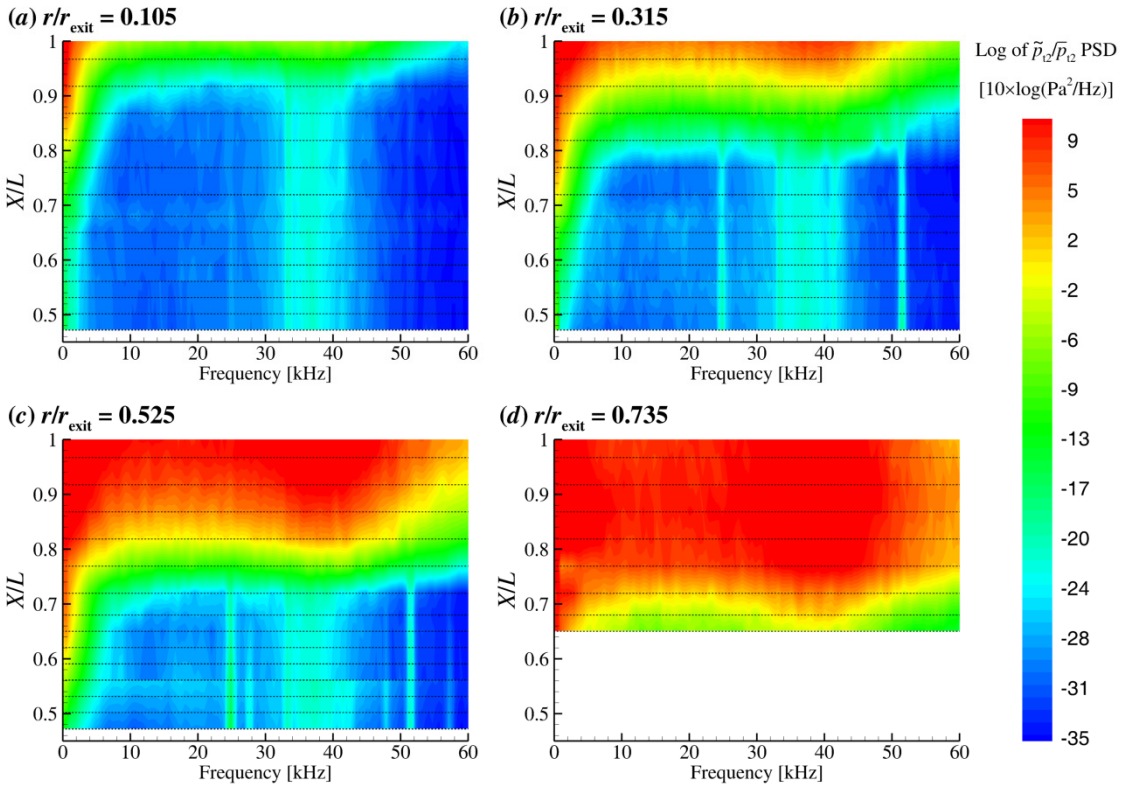

Figure 5–6. Spatial evolution of freestream noise spectra for $Re = 10\times10^6$ m^{-1}. Shown are contours of the log of the amplitude of the power spectral density of $\tilde{p}_{t2}/\overline{p}_{t2}$ for (*a*) $r/r_{exit} = 0.105$, (*b*) $r/r_{exit} = 0.315$, (*c*) $r/r_{exit} = 0.525$, and (*d*) $r/r_{exit} = 0.735$. Dashed lines indicate the discrete X/L locations at which the data were taken.

In regions of nominally quiet flow, the only measurable energy in the pressure signal is relatively low in amplitude and exists only at frequencies < 10 kHz. For $Re = 8\times10^6$ m^{-1}, the evolution from quiet flow to fully-turbulent noisy flow at any lateral location occurs over an axial distance of approximately 20–25 cm. This process appears more rapid for $Re = 10\times10^6$ m^{-1}, occurring over a distance of approximately 15 cm. Of note is that the spectra show a uniform onset of a broadband turbulence; if the nozzle-wall boundary-layer transition process is characterized by the growth of any particular frequency which later breaks down, the effect of this instability frequency is not measurable in the noise radiated into the freestream flow. It is also possible that the transition process on the nozzle wall is due to a more-rapid breakdown mechanism; this possibility is discussed in further detail in later sections.

Section 5.4 provides additional spectral information in the freestream with substantially higher bandwidth through the use of a PCB sensor.

5.3. Performance at select locations on the nozzle centerline versus *Re*

5.3.1. Mach number and freestream noise

Whereas the spatial mapping shown in Section 5.2 demonstrates the character of the freestream flow environment at two unit Reynolds numbers which precede the total loss of quiet flow in the nozzle, it is also instructive to obtain insight into the evolution of flow quality at a fixed location on the nozzle centerline vs. *Re*, including the nature of a total loss of quiet flow, which occurs near $Re \approx 11\times10^6$ m^{-1}.

Again a Kulite sensor in the Pitot configuration was employed in the same manner as above. For each run, the probe remained fixed at a given *X/L* location on the nozzle centerline for the duration of a single run, during which time the stagnation pressure, p_{t1}, was steadily increased in order to vary *Re*. Temperature was nominally held to $T_{t1} = 430 \pm 5$K. Data were sampled at 200 kHz for approximately 90 discrete segments of time each 250 ms in duration. The signal conditioner used for these runs was of the Purdue design discussed in Section 4.2.1. In contrast to the Endevco Model 136 used for the spatial mapping of Section 5.2, this unit uses a linear power supply and low-noise amplifiers, yielding a substantially cleaner electronic noise profile free of the 25–50 kHz content evident in Figure 5–5 and Figure 5–6.

Figure 5–7 shows the evolution of both $\tilde{p}_{t2}/\overline{p}_{t2}$ and *M* with *Re* for probe locations of *X/L* = 0.53, 0.72, and 1.00. In regions of nominally quiet flow, fluctuating Pitot pressure, $\tilde{p}_{t2}$, is calculated from the output of the second stage of the Purdue signal conditioner, with a total gain of 69.2 dB (2880×) applied to the 100 mV full-scale sensor output. In regions of transitional and noisy flow, however, this channel is overloads the data acquisition unit (peak voltage > 10V) and so $\tilde{p}_{t2}$ is then calculated from the output of the first stage of the signal conditioner, with a gain of 40 dB (100×).

The data are consistent with the spatial maps of Section 5.2 in that very low levels of freestream noise $\tilde{p}_{t2}/\overline{p}_{t2}$ are observed in the interior of the quiet core for $Re = 8\times10^6$ m^{-1} and $Re = 10\times10^6$ m^{-1}, with slightly higher levels ($\tilde{p}_{t2}/\overline{p}_{t2} \approx 0.5\%$) observed at the exit plane.

In the NASA Langley experiments of Blanchard *et al.* (1997), a sharp rise in uncalibrated hot-wire (≈ mass flux) fluctuation was observed at the nozzle exit plane on the centerline at $Re = 10.0\times10^6$ m^{-1}. In the current data set, a similar rapid rise is observed in the $\tilde{p}_{t2}/\overline{p}_{t2}$ data of Figure 5–7(*a*) at $Re \approx 10.7\times10^6$ m^{-1} at the same probe location, and is seen only slightly later at $Re \approx 11.2\times10^6$ m^{-1} for the most-upstream probe location of $X/L = 0.53$. In this regard, the nozzle's current and historical quiet-flow performance appear very similar, although as mentioned before, it is inappropriate to draw strong conclusions from a comparison of uncalibrated hot-wire data and the present calibrated Pitot data.

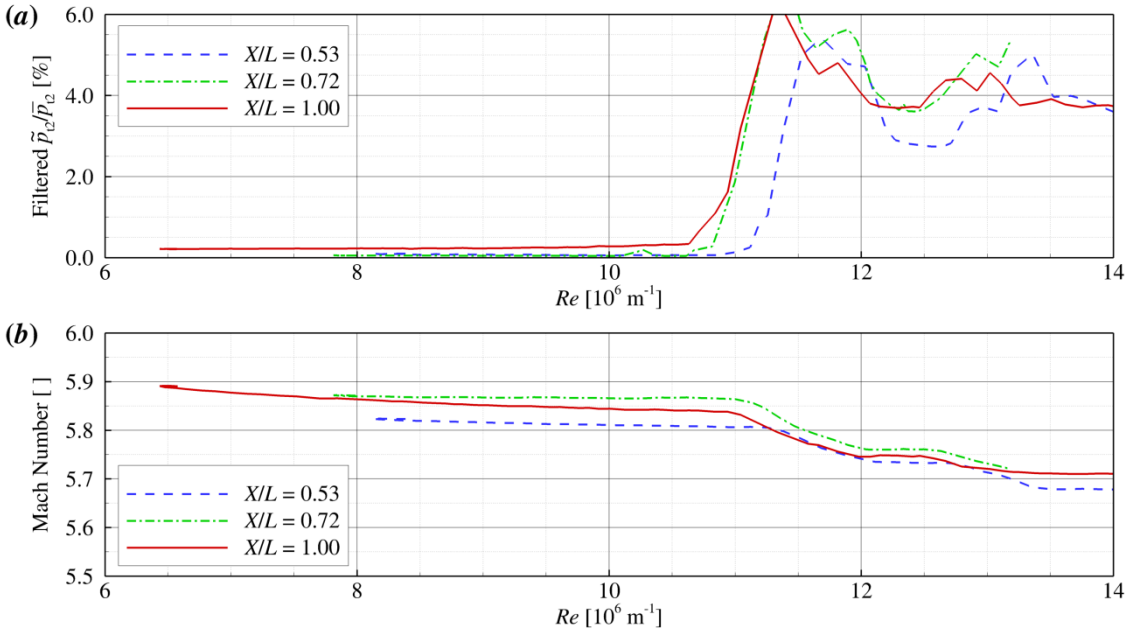

Figure 5–7. Centerline $\tilde{p}_{t2}/\overline{p}_{t2}$ and Mach number vs. Re for select axial probe locations. Notable are the two distinct peaks in $\tilde{p}_{t2}/\overline{p}_{t2}$ amplitude near $Re = 11.5\times10^6$ and $Re = 13\times10^6$, coinciding with a two-stage reduction in Mach number, suggesting the possibility of an azimuthally-nonuniform transition process on the nozzle wall.

The rapid forward movement of the nozzle-wall transition front with Re likely indicates a bypass mechanism, potentially involving defects in the nozzle wall.

Also of note in Figure 5–7(a) are the two distinct peaks in $\tilde{p}_{t2}/\overline{p}_{t2}$ amplitude near $Re = 11.5\times10^6$ m^{-1} and $Re = 13\times10^6$ m^{-1}, which are seen to coincide with a two-stage reduction in Mach number in Figure 5–7(b). The high peaks of $\tilde{p}_{t2}/\overline{p}_{t2}$ amplitude (4–6%) are indicative of heavily-intermittent, late-stage transitional fluctuations in the nozzle boundary layer, whereas noise radiated by a fully-turbulent nozzle boundary layer has lower amplitudes (3–4%). The appearance of multiple transitional peaks in the RMS amplitude suggests the possibility of a multiple-stage transition process. That is, it is likely that the isolated defects leading to rapid-onset transition cast only narrow wedges of turbulence behind them, and do not cause the entire circumference of the nozzle surface to undergo transition simultaneously. As additional defects become critical, then, additional sections of the nozzle circumference become transitional and break down, leading to additional peaks in the $\tilde{p}_{t2}/\overline{p}_{t2}$ amplitude.

This theory is supported by the two-stage reduction in Mach number seen in Figure 5–7(b), suggesting that the nozzle boundary-layer displacement thickness around the azimuth increases to turbulent values in stages, changing the effective area ratio in several discrete steps.

It would be instructive to investigate this behavior further by directly studying the state of the nozzle boundary layer around the azimuth, perhaps using hot-film anemometry. If the defects responsible for the initial transition of the nozzle boundary

layer could be identified and repaired, the performance of the nozzle could potentially be substantially improved.

Surveys of $\tilde{p}_{t2}/\overline{p}_{t2}$ versus unit *Re* for fixed probe locations, exemplified by the data of Figure 5–7, are performed regularly in the M6QT – especially after periods of downtime and between model changes – as a means to monitor the quiet flow performance of the tunnel. Since the installation of the M6QT following the nozzle repolishing effort of early 2010, its quiet flow performance has been remarkably consistent, and no extraordinary measures (disassembly for cleaning, further polishing, etc.) have been necessary.

5.3.2. Time series of Pitot pressure and intermittent disturbances

In addition to the general trends of RMS $\tilde{p}_{t2}/\overline{p}_{t2}$ and Mach number presented in the previous subsection, it is also instructive to investigate in further detail the character of the breakdown of the quiet flow environment at high *Re* through an inspection of the time series. For a representative example, Figure 5–8 presents the time series output of the Kulite Pitot sensor for the centerline probe location $X/L = 0.72$, as freestream *Re* was slowly increased from approximately $Re = 8\times10^6$ m^{-1} to $Re = 13\times10^6$ m^{-1}. For reference, these are the source data from which the RMS trends of Figure 5–7(*a*) were calculated.

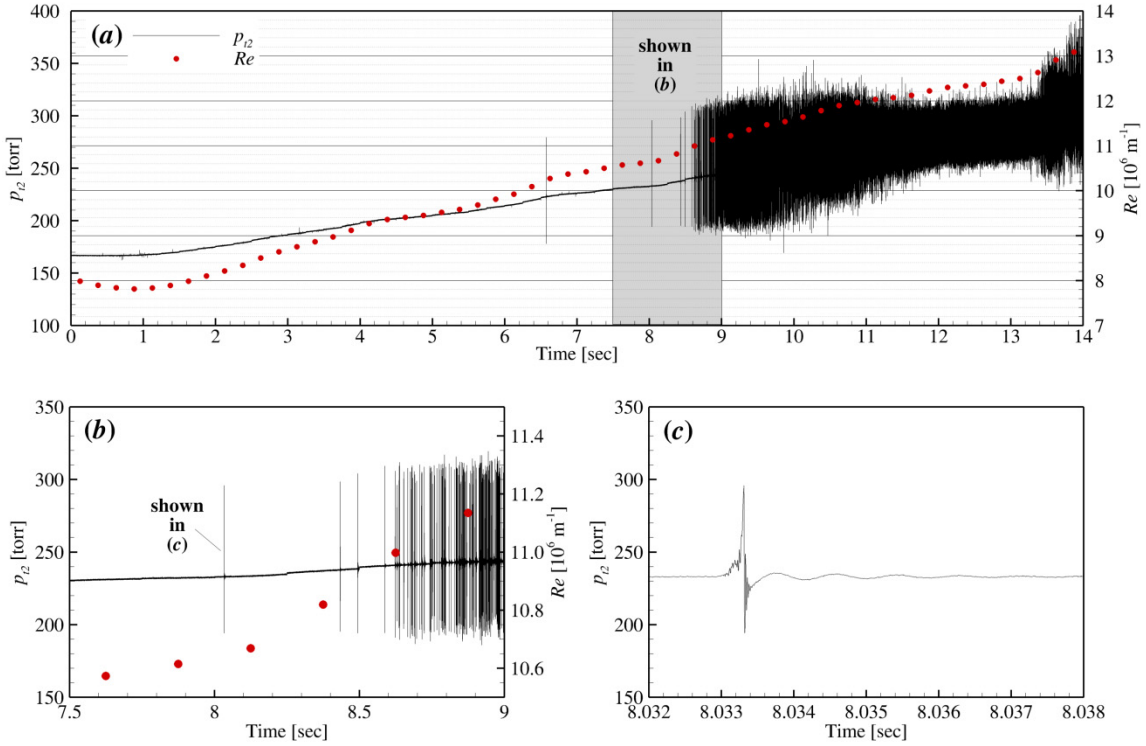

Figure 5–8. Time history of Pitot pressure, p_{t2}, during a continuous *Re* variation. $X/L = 0.72$. Shown are (*a*) the entire time series for the run, (*b*) a short segment of the run between $Re = 10.6$ and 11.3×10^6 m^{-1} as the intermittency becomes saturated, and (*c*) a single representative intermittent disturbance, characterized by an exponential rise in p_{t2}, a sharp decrease, and a gradual return to the nominal pressure. The *O*(1 kHz) oscillations thereafter are likely due to a ringing in the filter's impulse response.

Figure 5–8(*a*) shows – in the black lines – the time-series Pitot data versus time for the entire on-condition duration of the run. The red circular markers indicate the unit *Re* condition at each time step, and are referenced to the secondary ordinate. Most evident in this figure is the striking difference in the magnitude of the fluctuation of the time series for nominally-quiet ($t < 8.5$ sec; $Re < 11\times10^6$ m^{-1}) and nominally-noisy flow. Upon closer inspection (see Figure 5–8(*b*)), it becomes apparent that the initial onset of noisy flow at $Re = 11\times10^6$ m^{-1} is characterized by a rapidly-increasing density of

isolated, intermittent impulse disturbances. It is the increasing frequency of these high-amplitude intermittent disturbances which accounts for the overshoots in the RMS amplitudes shown in Figure 5–7(*a*) prior to total breakdown of the boundary layer and the resulting lower noise amplitudes. Occasionally, these intermittent disturbances occur in single isolated events at lower *Re*, as seen at 8.0 seconds for the current run.

These intermittent disturbances have been observed in the hot-wire surveys conducted at NASA Langley (cf. Fig. 11 of Blanchard *et al.* 1997 or Fig. 1 of Wilkinson *et al.* 1994). They are characteristic of large-amplitude turbulent packets in the nozzle boundary layer passing the upstream location on the wall which is the acoustic origin of the sensor on the centerline. Thus, the sensor sees single, isolated acoustic-mode disturbances as an impulse. Viewed closely in Figure 5–8(*c*), these disturbances have a typical nominal duration of 1 ms, and are characterized by a region of exponential growth, a sudden amplitude decrease (as if due to a passing weak shock wave), and an exponential recovery to the nominal level. In the current data, an *O*(1 kHz) oscillation is also seen subsequent to the impulse, but this is thought to simply be a result of the impulse response characteristics of the analog filtering and amplification circuitry. Also seen is a much higher-frequency ringing effect immediately following the sudden amplitude decrease; this is likely attributed to excitation of the sensor's natural frequency.

Knowledge of this behavior is important in providing context for interpretation of results near the typically-observed threshold for reliable quiet flow of $Re = 10\times10^6$ m^{-1}, and indeed beyond it, as the intermittent nature of the onset of noisy flow permits useful

durations of quiet flow (several milliseconds) as high as $Re = 11\times10^6$ m^{-1}. This will be discussed further in the interpretation of Figure 7–4 in Section 7.5.

5.4. High-bandwidth freestream spectra versus *Re* in quiet and noisy modes

In order to supplement the Kulite data of Sections 5.2 and 5.3 to provide a characterization of the spectral content of the freestream with higher bandwidth, a PCB-132A31 sensor (§4.2.2) was installed in the Pitot configuration. With a resonant frequency near 1 MHz, the PCB sensor provides meaningful spectral data with a bandwidth of at least 500 kHz. It is, however, internally high-passed at 10 kHz, so DC pressures and low-frequency fluctuations are not obtained.

Runs were conducted with the PCB probe located at either of two axial positions on the nozzle centerline, $X/L = 0.77$ and $X/L = 1.0$. For each probe location, one run was conducted with the tunnel in the noisy mode (with bleed valves closed), and one in the quiet mode (with bleed valves open). During each of the four runs, the stagnation pressure, p_{t1}, was slowly varied from nominally 700 kPa [100 psia] to 1100 kPa [160 psia]. In each case, the stagnation temperature, T_{t1}, was nominally 430 K. Signals from the PCB sensor were bandpass filtered from 1 kHz to 1 MHz (–6 dB/decade) using the Stanford Research SR560 and additionally low-pass filtered with a 500 kHz, 8-pole (–48 dB/decade) Krohn-Hite butterworth filter for anti-aliasing. Data were sampled at 2 MHz for ninety discrete 100 ms segments throughout the duration of each run. For each segment, power spectra were computed using Hamming windows 4096 points in length, with 3500-point overlap.

Figure 5–9 and Figure 5–10 present the evolution of the spectral content on the freestream centerline at X/L = 0.77 and X/L = 1.0, respectively, for both BVO and BVC modes of tunnel operation. In each case, subfigure (*a*) shows as a contour plot the complete evolution of the spectra for all p_{t1} for BVO and BVC, while subfigures (*b*), (*c*), and (*d*) show, for clarity, data extracted from the segments where $Re = 10\times10^6$ m^{-1}, $Re = 11.5\times10^6$ m^{-1}, and $Re = 12\times10^6$ m^{-1}, respectively.

These data show several interesting general features. In the noisy mode, the spectra (see translucent gray surfaces in both Figure 5–9(*a*) and Figure 5–10(*a*)) are of a broadband nature, and change very little throughout the entire range of *Re*; the distribution of dynamic content in the freestream under a fully-turbulent nozzle wall with BVC does not significantly vary with *Re*.

In the BVO mode, the spectral evolution of the noise with increasing *Re* – shown in the colored surfaces of subfigures (*a*) – follows expectation based on the Kulite results of Section 5.3. That is, the flow is nominally quiet at both forward and exit-plane probe locations until $Re \approx 10.5\times10^6$ m^{-1}, at which point the noise level rapidly rises in a broadband fashion – transition on the nozzle wall likely rapidly moves far forward, suggesting a bypass mechanism.

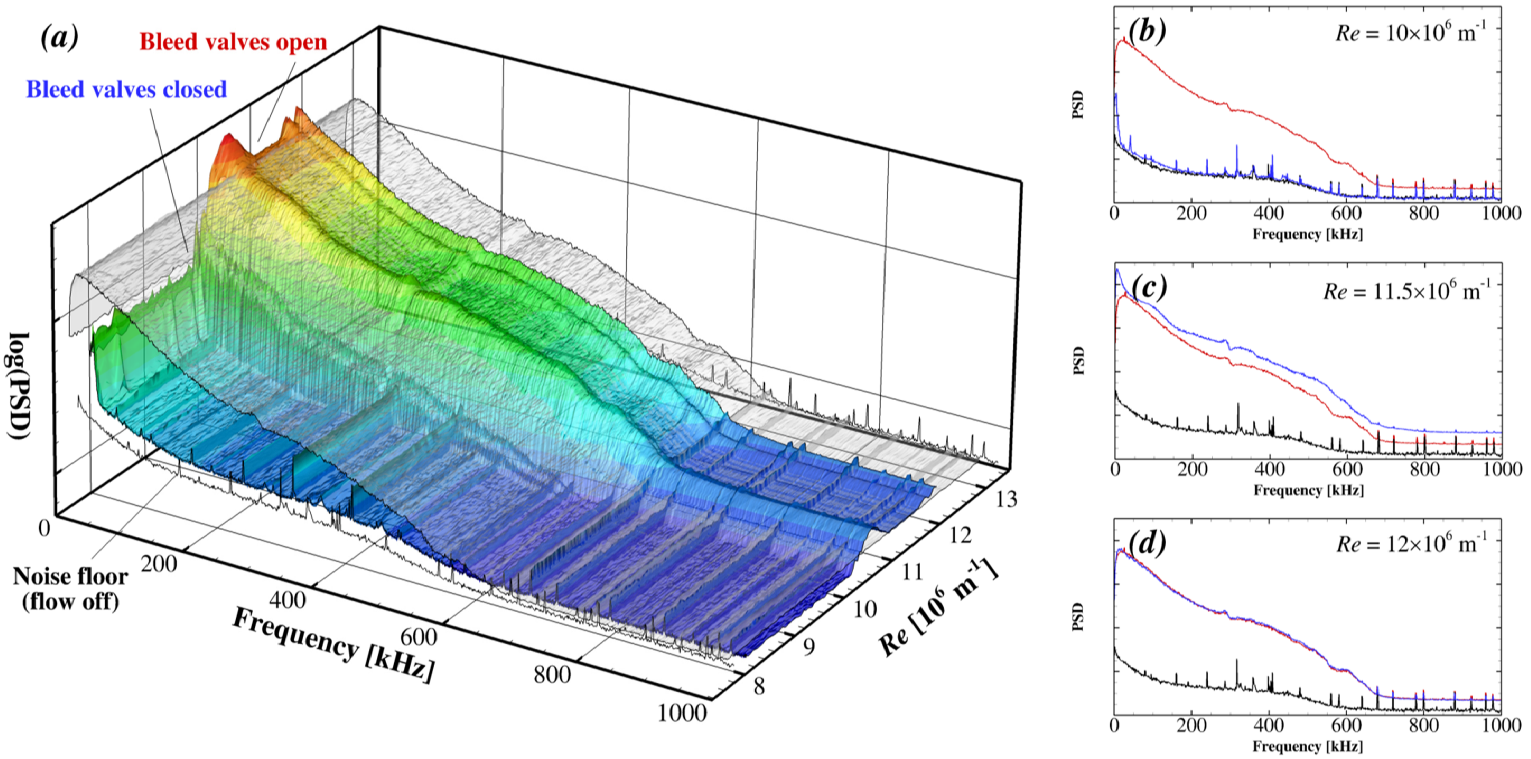

Figure 5–9. High-bandwidth spectra from PCB Pitot sensor at $X/L = 0.77$. Quiet (BVO) and noisy (BVC) configurations. Shown is *(a)* the overall comparison of BVC and BVO spectra, and select data shown for (*b*) $Re = 10\times10^6$ m^{-1}, (*b*) $Re = 11.5\times10^6$ m^{-1}, and (*d*) $Re = 12\times10^6$ m^{-1}.

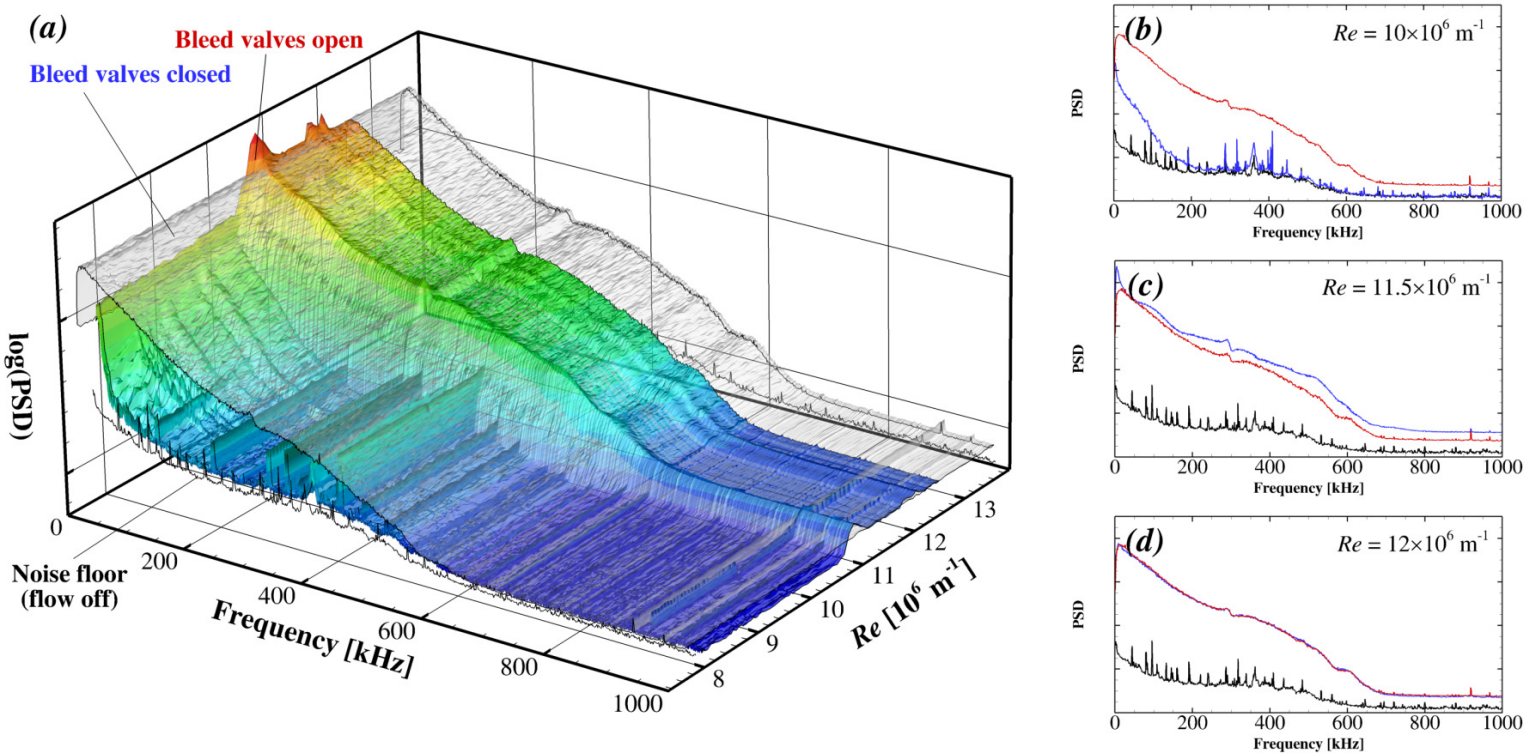

Figure 5–10. High-bandwidth spectra from PCB Pitot sensor at X/L = 1.00. Quiet (BVO) and noisy (BVC) configurations. Shown is *(a)* the overall comparison of BVC and BVO spectra, and select data shown for for (*b*) $Re = 10\times10^6$ m^{-1}, (*b*) $Re = 11.5\times10^6$ m^{-1}, and (*d*) $Re = 12\times10^6$ m^{-1}.

Subfigures (*b*) show a comparison of spectra for BVO and BVC at each probe location for $Re \approx 10\times10^6$ m^{-1}. At the upstream probe location (Figure 5–9(*b*)), the spectra for the BVO case (blue), are effectively identical to the electronic noise floor of the instrument (black). That is, the fluctuating disturbances in the freestream are too small to effectively measure across the entire bandwidth of the PCB sensor. For the downstream probe location at the same unit Reynolds number, shown in Figure 5–10(*b*), some measurable low-level fluctuation is present below 200 kHz.

In addition, the two distinct peaks of fluctuation intensity seen in the Kulite data near $Re = 11.5\times10^6$ m^{-1} and 13×10^6 m^{-1} are visible in the PCB spectra across the full bandwidth. Subfigures (*c*) show direct comparisons of spectra in the BVO and BVC for $Re \approx 11.5\times10^6$ m^{-1}, where the first transitional peak occurs. Here, it is evident that the increased levels of fluctuation – likely due to the intermittent, transitional state of the nozzle boundary layer – occur at a wide range of frequencies up to 600 kHz. In particular, the levels are relatively highest (with respect to the BVC case) for frequencies less than 50 kHz and greater than 150 kHz.

Finally, subfigures (*d*) show a comparison of BVO and BVC spectra at $Re \approx 12\times10^6$ m^{-1}, between the first and second peaks in intensity. Here, it is seen that the noise spectra in the BVO and BVC modes are effectively identical; the state of the boundary-layer bleed valves does not affect the freestream Pitot pressure spectra for unit Reynolds numbers at which the freestream is under a fully-developed turbulent nozzle boundary layer with BVO.

5.5. Location of the flared cone model in the quiet test core

To provide context for the flared-cone stability & transition experiments discussed in the following two major sections, it is important to briefly discuss the physical placement of the cone model within the freestream environment described above. For the remainder of the work discussed, the tunnel was nominally operated at $Re = 10\times10^6$ m^{-1}, and the flared cone model was positioned on the nozzle centerline at a nominal zero degree incidence with the base of its contour positioned 102 mm from the nozzle exit plane.

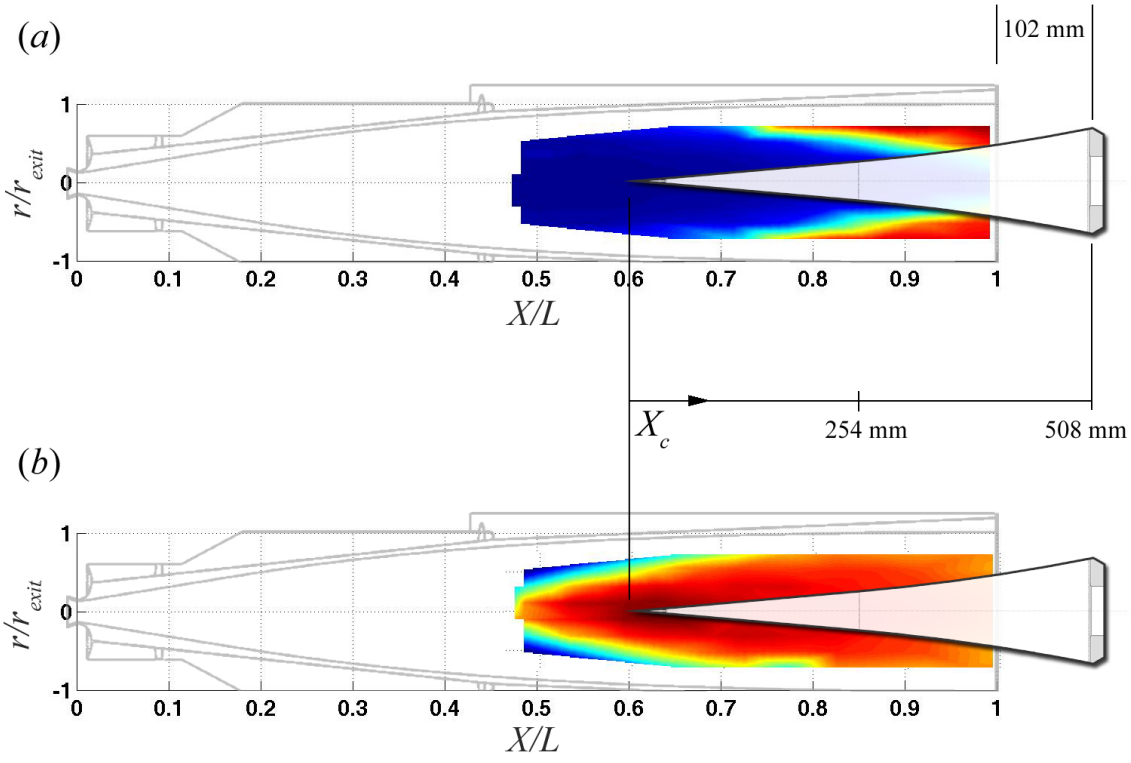

Figure 5–11. Freestream flow environment with installed cone location. $Re = 10\times10^6$ m^{-1}. Shown are qualitative contours of (*a*) RMS Pitot noise $\tilde{p}_{t2}/\overline{p}_{t2}$ and (*b*) Mach number, superimposed with the Langley 93–10 flared cone model in test position.

Figure 5–11 presents the previously-shown contours of (*a*) $\tilde{p}_{t2}/\overline{p}_{t2}$ and (*b*) freestream *M* for $Re = 10\times10^6$ m^{-1}, this time with a physical 1:1 aspect ratio and superimposed with depictions of the nozzle contour and the installed location of the flared cone model. As before, axes are normalized by the nozzle exit radius, r_{exit}, and nozzle length, *L*. Clearly visible in the freestream $\tilde{p}_{t2}/\overline{p}_{t2}$ data of Figure 5–11(*a*) is the onset of nozzle-wall transition and the resulting impingement of pressure disturbances onto the flared cone model. Here, it can be seen that a substantial portion of the upstream part of the cone lies within a low-disturbance portion of the freestream environment, whereas the portion of the cone model downstream of $X_c \approx 350$ mm lies within a region of higher disturbance levels. This is not significantly dissimilar from the extent of noise impingement present for the previous experiments at NASA Langley; Lachowicz *et al.* (1996) noted noise impingement for $X_c > 362$ mm for a slightly lower $Re = 9.3\times10^6$ m^{-1}, and Blanchard *et al.* (1997) depicted noise impingement on the "91–6" cooled-wall cone model for $X_c > 337$ mm at $Re = 9.35\times10^6$ m^{-1}.

Although the author considers the freestream environments of the historical and present experiments to be very similar, the effect of this noise on the instability growth and transition of the cone boundary layer is an issue that must be considered. Is the boundary layer receptive to acoustic radiation at these downstream locations on the cone, and at the appropriate scales? If so, is the growth of the resulting instabilities sufficient to interfere with measurements taken in this region? Future work should explicitly address the receptivity of the boundary layer to downstream noise impingement and the resulting impact on stability and transition.

6. SECOND-MODE INSTABILITY MEASUREMENTS ON A FLARED CONE WITH COMPUTATIONAL COMPARISON*

6.1. Overview

With the understanding of the behavior and reliability of the quiet tunnel's test environment provided by the previous section's characterization efforts, and with confirmation that the present flow quality performance is highly similar to its historical NASA Langley levels, the initial stability and transition experiments in the facility's Texas A&M installation were conducted. As a substantial first step toward the goal of using the M6QT as a platform for validation of stability computations, hot-wire anemometry is employed here in the study of the growth of the second-mode instability on a flared cone at zero angle of attack, with comparison to simulations based on linear parabolized stability equations (LPSE).

Because this initial campaign represents the first hypersonic stability experiments to be conducted in a newly-established facility, using newly-established diagnostic capabilities, the NASA Langley 93–10 flared cone test article (described in Section 3) was selected. This cone model has been previously studied in the quiet tunnel's former installation at NASA Langley by Lachowicz (1995) at zero degree incidence, by Doggett (1996) at 2º and 4º, and later by Horvath *et al.* (2002) in a conventional facility. In this sense, it serves in the present campaign as a 'benchmark' test article, allowing

* Portions of this section are reprinted with permission from "Boundary-Layer Instability and Transition on a Flared Cone in a Mach 6 Quiet Wind Tunnel" by Hofferth, J. W., Saric, W. S., Kuehl, J., Perez E., Kocian T., and Reed H. L., 2013. *Int. J. Eng. Sys. Modelling and Simulation* **5**(1/2/3):109–124., Copyright 2013 by Inderscience Enterprises Ltd.

comparisons to can be made to the previous work. The experiments described here then serve primarily as an opportunity to develop and demonstrate the new diagnostics and further qualify the facility for future work, although new insight is provided both here and in Section 7.

The data and analyses of this section are presented in several stages. First, representative cone-wall thermocouple data provides context for the instability measurements by establishing the transition location in the tunnel's quiet (BVO) and noisy (BVC) modes.

Next, uncalibrated boundary-layer profiles of mean and fluctuating hot-wire voltage (representative of mass flux) are presented for several axial locations on the cone. Spectral energy content is observed at second-mode frequencies, f_0, between 250 and 310 kHz. Growth of this high-frequency content is compared with N-factor results from computations, and possible sources of a ≈17% disagreement between the experimental and computed frequencies for second-mode growth are discussed.

To experimentally investigate one of these possible sources of error, a parametric study is conducted in order to determine the sensitivity of f_0 to small angles-of-attack of the test article about 0º. A strong sensitivity is observed, which provides a valuable uncertainty band for comparison with computations and motivates an even higher level of care in both the initial experimental setup and in cooperation with those performing computational simulations. This parametric study is conducted using focused schlieren deflectometry, the high-bandwidth (≈1 MHz) optical technique described in Section 4.3 and later applied more heavily in the nonlinear analyses of Section 7.

6.2. Cone transition location

As the simplest available diagnostic for the initial flared-cone experiments, transition on the model was monitored using the embedded array of 51 thermocouples. In previous experiments conducted in the tunnel at NASA Langley, where available tunnel run times exceeded 30 minutes at constant condition, this thermocouple array was used to determine adiabatic wall recovery temperatures, identifying regions of transitional or turbulent flow by the higher steady-state temperatures present due to a higher recovery factor. However, in the tunnel's present installation, where run time does not exceed 40 seconds, the model surface does not have sufficient time to reach adiabatic conditions. Furthermore, because 10 to 15 minutes of subsonic convective preheating of the tunnel facility is required to establish the proper stagnation temperature prior to a full tunnel run, the cone model begins the run with wall temperatures higher than the adiabatic condition by approximately 10%. Therefore, for the duration of a given tunnel run, the cone wall temperature varies, and transition can only be observed in the differing rates of temperature change; the wall is cooled relatively slowly in regions of laminar flow, is cooled quickly under a turbulent boundary layer, and is relatively heated in regions of transitional flow.

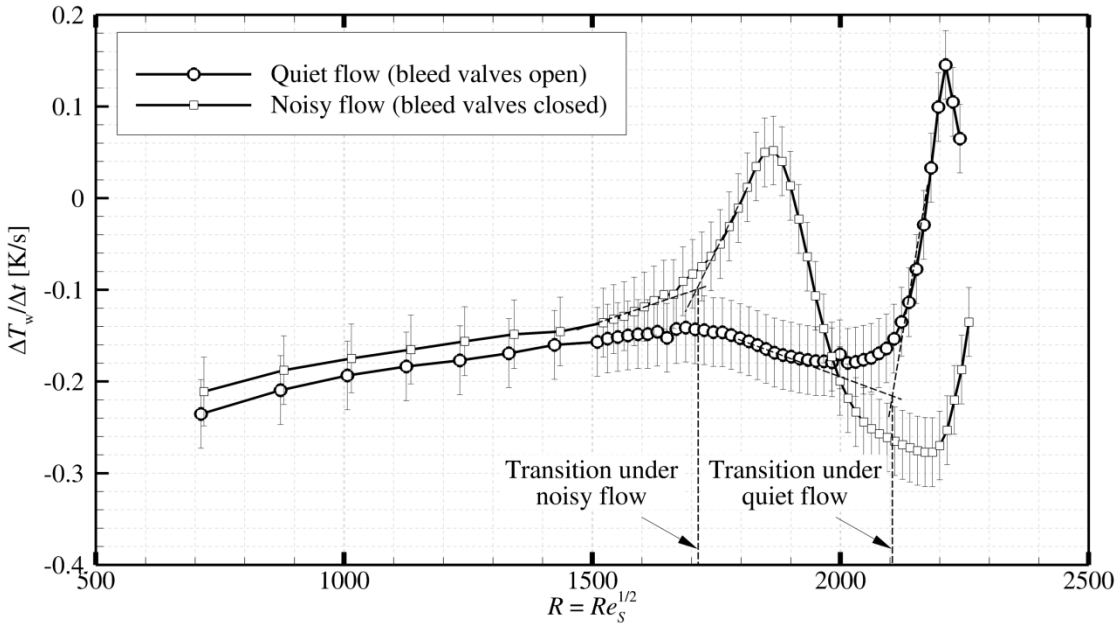

Figure 6–1. Cone transition location using wall temperature change rates. Data are shown for tunnel operated in quiet mode (bleed valves open) and noisy mode (bleed valves closed) at $Re = 9.9\times10^6$ m^{-1}. Note: error bars indicate typical drift in rates over run duration.

Figure 6–1 presents typical profiles of the rate of temperature change along the axis of the cone for both quiet and noisy flow at $Re = 9.9\times10^6$ m^{-1}. The noisy flow condition was obtained with the nozzle-throat boundary-layer extraction valves closed; this is only ever done only for demonstration purposes, and does not represent a relevant flow condition. Cone axial stations have been cast in terms of cone Reynolds number, defined using freestream conditions and the distance along the cone arc surface, S:

$$R = \sqrt{Re_S} = \sqrt{\frac{\rho_\infty U_\infty S}{\mu_\infty}}, \tag{6.1}$$

where ρ_∞ and U_∞ are the freestream density and velocity, respectively, and μ_∞ is the freestream absolute viscosity evaluated using Sutherland's Law. Error bars in Figure 6–1

represent the slight slowing of the rate of temperature change over the duration of the run as the adiabatic condition is approached (but never reached); magnitudes of the drift are typically 0.05 to 0.1 K/s for a typical run. This drift does not substantially change the character of the curve and thus does not significantly affect the interpretation of transition location.

Under noisy conditions (square markers), transition appears to begin near $R = 1700$ ($X_c = 0.3$ m), with fully-turbulent flow for $R > 2000$. The slower transient response aft of $R = 2200$ is an artifact of the thermal inertia of the 13 mm-thick mounting structure at the cone base. With the bleed valves opened (circular markers), a low-disturbance test environment is created, and transition onset moves aft to $R = 2100$ ($X_c = 0.44$ m), and fully turbulent flow is not observed on the cone.

Table 6–1 compares the transition-onset Reynolds numbers observed in the current campaign with those observed by Lachowicz (1995), here cast in terms of Re_S for easier comparison.

Table 6–1. Comparison of flared cone transition Reynolds numbers.

Data set	Freestream unit Re [m^{-1}]	Reynolds number at transition onset, $Re_{S,tr}$ [m^{-1}]	Notes
Lachowicz (1995)	9.3×10^6	4.2×10^6	Adiabatic wall; $Re_{S,tr}$ calculated from recovery temperatures; Noise impingement for $X_c > 362$ mm
Hofferth (2012)	9.9×10^6	4.4×10^6	$T_w = f(X_c,t)$; $Re_{S,tr}$ calculated from temperature *rates*; Noise impingement for $X_c > 305$ mm

Although the agreement here (≈5% in $Re_{S,tr}$ for similar freestream Re) is quite encouraging, the authors are reluctant to draw any strong conclusions from the direct comparison, as the differences in the experiments are numerous; these include any differences in facility flow quality, uncertainty in model angles of attack, and, most importantly, the necessarily and substantially different thermal conditions on the model wall and the difference in thermocouple interpretation that this requires. Thus, the most important conclusion to be drawn from this comparison is a general one: after years of storage, relocation and reactivation of the M6QT facility and its models, transition onset on the Langley 93–10 model remains very near its base at the tunnel's high-Reynolds number quiet flow condition, as it was before.

Current practice is to monitor the thermocouple array in the above manner during all tunnel runs to provide a convenient independent verification of the state of the boundary layer during hot-wire measurements.

6.3. Boundary-layer mean and RMS profiles

Hot-wire profiles of mean and fluctuating properties are obtained at $Re \approx 10\times10^6$ m^{-1} for four locations on the flared cone model, depicted in Figure 6–2.

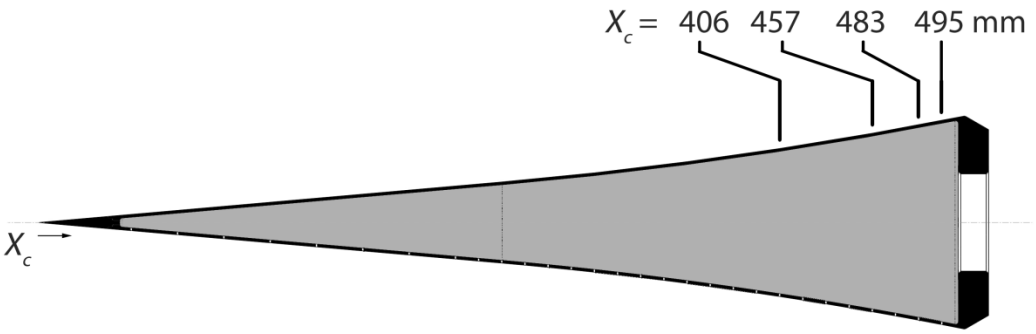

Figure 6–2. Hot-wire profile locations on the Langley 93–10 flared cone model.

Relevant run conditions for the hot-wire measurements presented are listed in Table 6–2. Average cone temperature is provided but is to be considered only notional, as it is nonuniform both spatially along the cone axis and temporally as it cools per the data of Section 6.2. Furthermore, because the thermocouple array is beneath the ray of hot-wire motion, there is a noticeable rise in measured wall temperature behind the probe as it descends into the boundary layer.

Table 6–2. Run conditions for hot-wire measurements.

Run Number	**Cone axial station X_c [mm]**	**P_{t1} [kPa]**	**T_{t1} [K]**	**Average Cone Temp T_w [K]**	**Unit *Re* [10^6 m^{-1}]**	***R* = *sqrt(Re$_S$)***
1266	406	906	443	410	9.7	1991
1261	457	909	429	399	10.3	2174
1263	483	906	427	398	10.3	2240
1264	495	905	428	397	10.3	2264

Platinum-rhodium hot wires of 2.5 μm core diameter were used as described in detail in Section 4.1. Tuning of the anemometer circuit was optimized during a tunnel run at the location of maximum RMS voltage intensity in the boundary layer. An impulse-response time constant of ≈2.5 μs was achieved in the boundary layer, indicating a –3 dB rolloff point in the frequency response near 333 kHz.

Uncalibrated mean and RMS anemometer output voltage are plotted normalized in Figure 6–3 for each axial location surveyed. Profiles of mean CTA voltage are displayed as solid black lines, normalized by the maximum and minimum CTA voltages encountered in the scan (an approximately 3-volt spread, pre-normalization). Profiles of RMS CTA voltage (calculated from the broadband signal) are in dashed lines, normalized by the maximum RMS voltage in each boundary layer.

The shape of the mean voltage profiles is largely well behaved and consistent with expectation, although a mild overshoot in the mean voltage is present near the boundary-layer edge. Kendall (1957) observed an overshoot in impact pressure profiles on a flat plate at Mach 5.8 acquired when using only the largest of three Pitot probes. It is believed that the overshoot observed in the present data set is likely due to a similar probe-interference effect, whereby a static pressure rise due to the probe lifts the boundary layer and modifies the effect of the probe shock to produce the overshoot. Future studies will employ smaller, more-streamlined probe bodies to test this hypothesis. Note also in the mean flow profiles that data at locations nearest the wall may include additional effects not present elsewhere in the boundary layer, chief among them the modified response of the hot wire in transonic/subsonic flow.

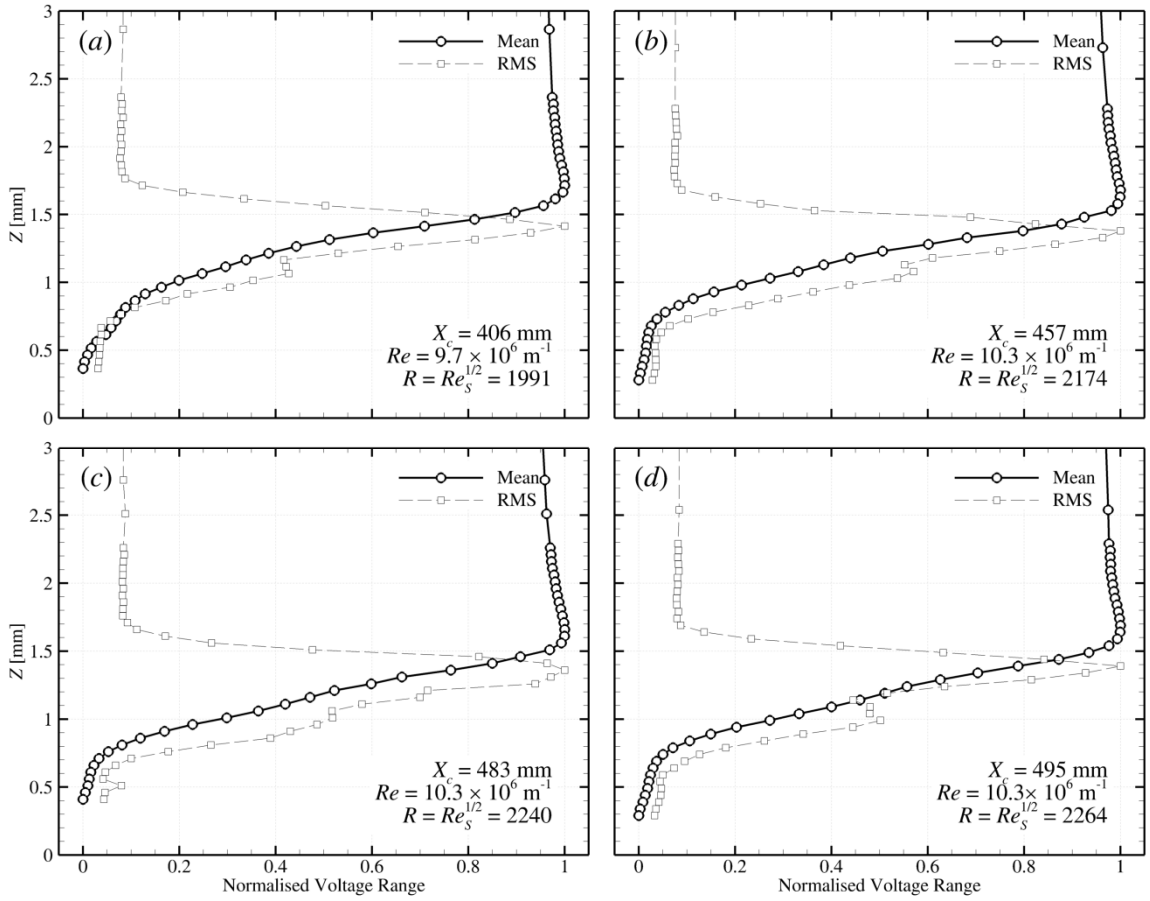

Figure 6–3. Uncalibrated CTA voltage profiles (high overheat ratio; ~ mass flux).

At each axial location considered, the height at which the maximum RMS fluctuation is observed corresponds to 80–90% of the boundary-layer thickness, in agreement with theoretical expectation based on the location of the critical layer, with the present computations for mode shapes of ρU disturbances, and with the observations of Lachowicz (1995).

Figure 6–4 presents – for observation of general trends only – the experimental mean boundary-layer profiles together with computed mass flux profiles, each

nondimensionalized by their local edge values. In contrast to Figure 6–3, the experimental data here have been normalized between 0.1 and 1 to casually reflect that the measurements do not actually reach the wall, and that sensitivity of the hot wire becomes complicated as the flow becomes subsonic (e.g., the "kink" in the data of Figure 6–4(*b*) near the amplitude of 0.1). Due to this and to the fact that hot-wire voltage does not vary linearly with mass flux, a direct comparison between experiment and computation cannot occur until calibrated hot-wire measurements are obtained. One additional difficulty in making such comparisons – one that would be present even if the hot wire were calibrated – is that the cone wall temperature is slowly varying as the boundary layer is being scanned. That is, the shape and thickness of the boundary layer is being physically distorted while it is being measured. Specifically, the boundary layer thins (due to the cooling of the wall) as the measurement point is traversed top-to-bottom. Thus, a different experimental profile is obtained when the boundary layer is scanned bottom-to-top instead. This may be accounted for in future simulations by performing several "quasi-steady" computations at different wall temperatures, according to the wall temperatures at the time each point was acquired in the experimental profile.

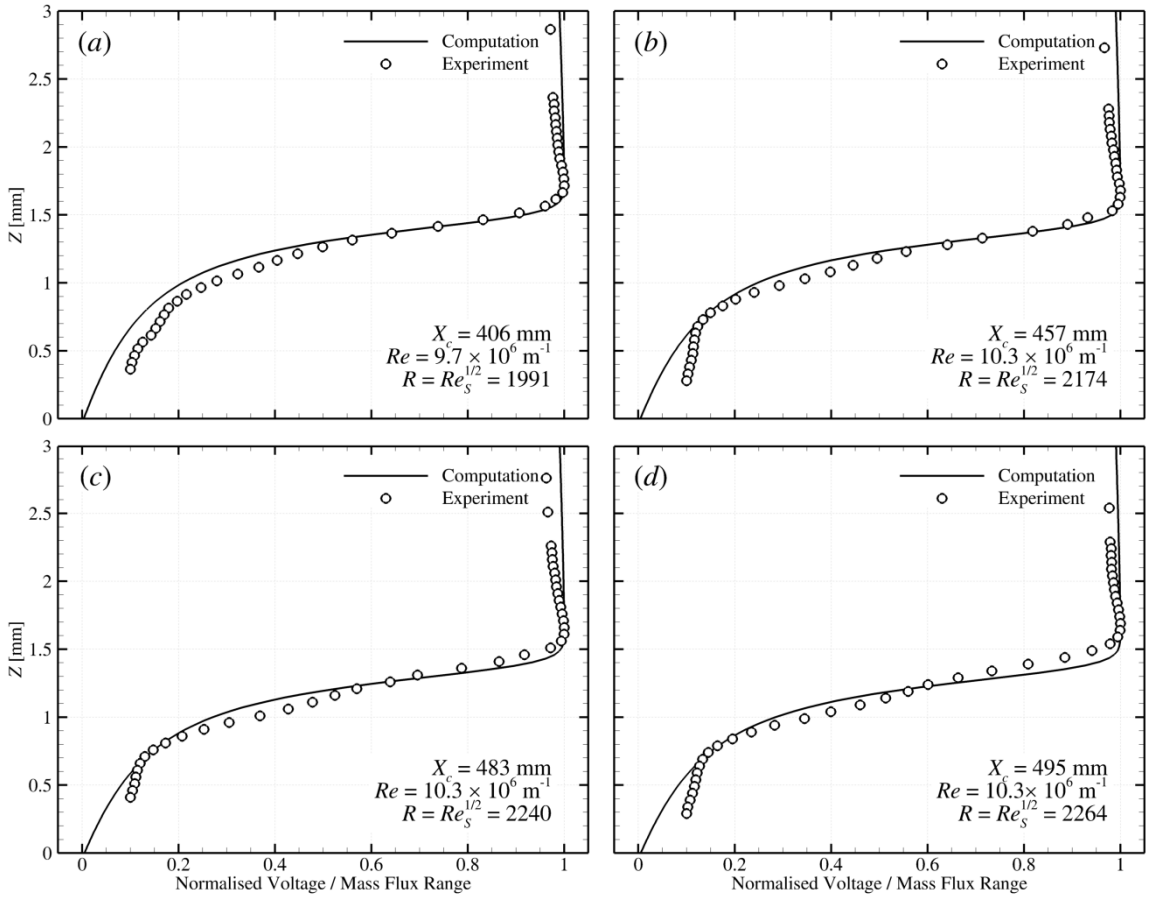

Figure 6–4. Normalized, uncalibrated CTA voltage profiles (high overheat; ~ mass flux) vs. normalized mass flux profiles from computed basic state.

For the present computational simulations, a structured two-dimensional grid was generated in the *Pointwise* meshing software. The grid size encompasses 599 grid points along the cone surface and 1499 in the wall-normal direction, with 912 in the shock layer and 330 in the boundary layer. Emphasis was placed on clustering cells in the boundary layer and shock region to capture regions of high gradients. The flow over the cone is solved as steady-state laminar flow using GASP (General Aerodynamic Simulation Program) computational software, Version 5.1. The code solves the unsteady

Navier-Stokes equations using a cell-centered finite volume scheme. The flow simulation was performed in GASP as an axisymmetric case at zero angle of attack (i.e., the slight model misalignment is not accounted for in the simulation). The computations are performed using the Roe-Harten implementation for the inviscid fluxes, with a van Albada limiter equal to 0.33 and a 3rd-order upwind biased spatial accuracy. A no-slip wall boundary condition was applied at the cone surface with a wall temperature of $T_w = 398$ K. Stability computations were performed on solutions from several grids of varying mesh density, and the present mesh was determined to be grid-converged by comparison of the LPSE *N*-factors, which are sensitive to very small changes in primary flow quantities (Perez *et al*. 2012).

Without attempting to draw unreasonably significant conclusions from Figure 6–4 given the aforementioned caveats, one can verify that indeed the boundary-layer thicknesses and general shape of the laminar boundary layer are at least very similar. The differences in boundary-layer thickness, δ_{99} (see also Figure 6–5), calculated at 0.99 times the edge mass flux, may be due to the spatial and temporal variation in the cone wall temperature (modeled computationally as a constant 398K). The slightly windward misalignment of the experimental measurement ray relative to the axisymmetric computation is likely not a dominant factor in the differences in δ_{99}, as this would manifest in the opposite direction, with the experimental δ_{99} less than the computed value.

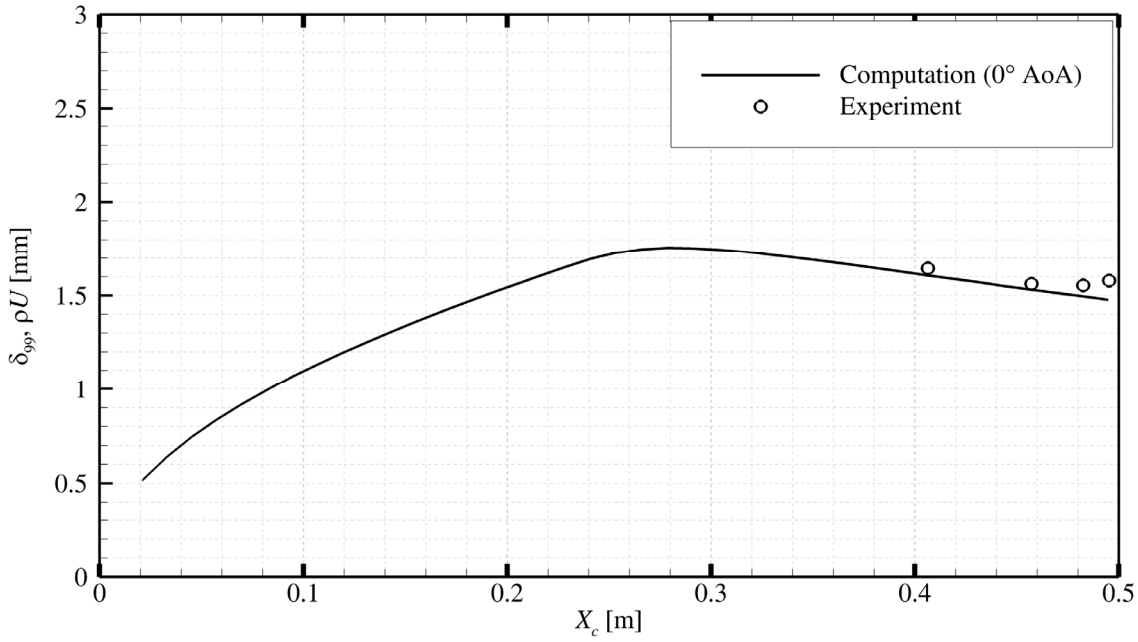

Figure 6–5. Boundary-layer thickness distribution, with comparison to computation.

6.4. Boundary-layer spectra and the second-mode instability

Figure 6–6 presents spectrograms of the unsteady hot-wire signal for each of the four axial cone stations sampled. Power spectra were computed from the anemometer voltage output using Welch's method (4096 points per Hamming window, 3500 point overlap) at each height in the boundary layer. Spectra were then smoothed for additional clarity using frequency averaging over bins 1 kHz wide. The smoothed spectra were then plotted as contours to show the spatial variation of the measured frequency content across the boundary layer. Grayscale levels in the spectrogram are mapped to the log of the amplitude of the power spectra, and the four images use the same scale.

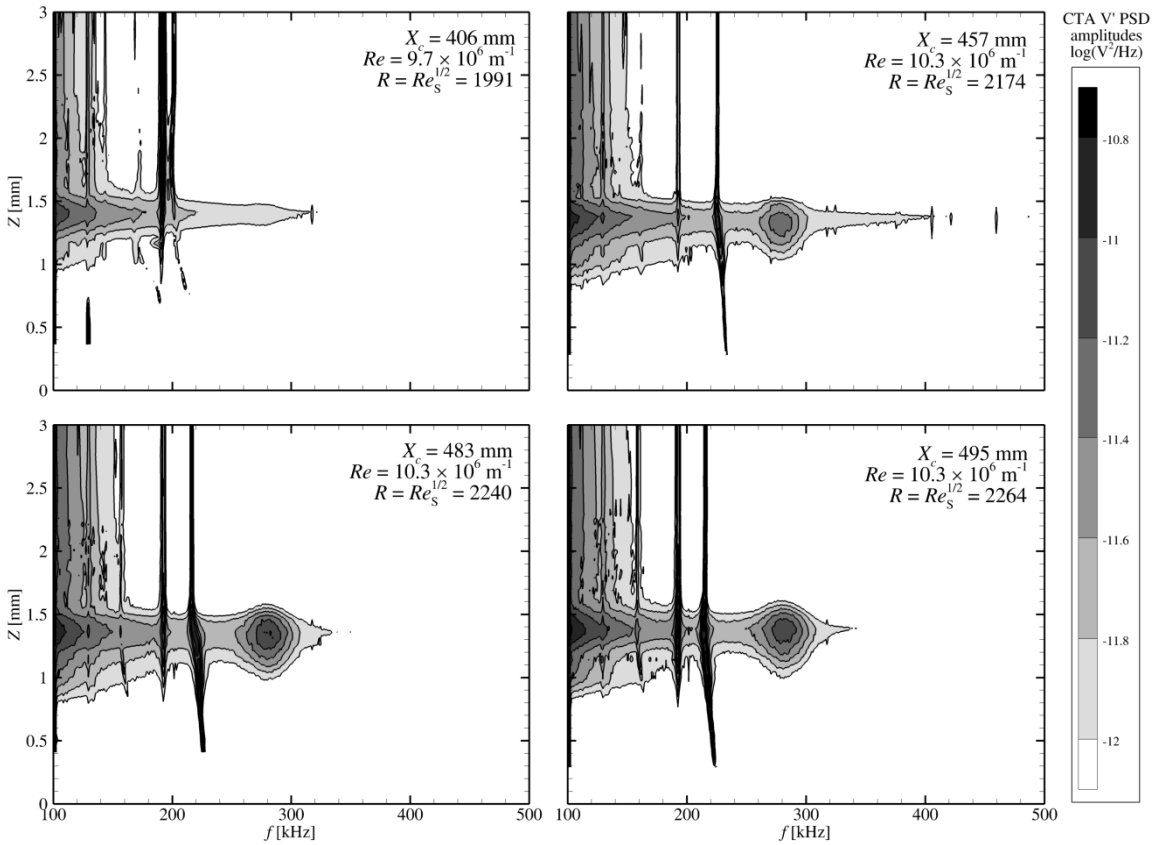

Figure 6–6. Spectra across the boundary layer at each axial station. $Re \approx 10\times10^6$ m^{-1}. Colormap ranges are consistent between stations.

The most notable feature in the spectrograms is the prominent development of second-mode energy content between f_0 = 250 and 310 kHz, first appearing at X_c = 457 mm, larger in intensity at X_c = 483 mm, and present but without additional growth at X_c = 495 mm. This represents the first measurement of energy content within the expected regime for second-mode instabilities in the M6QT at its Texas A&M installation. Earlier studies (Hofferth 2012) had used 5-μm wires with a bandwidth insufficient to resolve fluctuating content above ~150 kHz. Though the tuning for the present study is much improved and is sufficient to observe the presence of content at

these frequencies, suspicion remains regarding their amplitudes, as the nature of a –3 dB (50%!) rolloff near 333 kHz implies some attenuation of frequencies lower than this. Further characterization of the frequency response in the rolloff region is required in order to obtain confidence in amplitudes of second-mode measurements. Further optimization of bridge tuning may also be required.

Also evident in the spectrograms is the presence of at least two additional sharp peaks throughout the data set near 190 and 210–225 kHz. The peak at 190 kHz remains for all runs and does not shift as a function of height in the boundary layer. The second peak occurs at slightly different frequencies in each run, and for all axial stations the frequency slightly increases (to 225–240 kHz) as distance from the wall is reduced. Both peaks appear excited by the presence of high flow fluctuation levels, with higher amplitudes observed over much of the boundary layer relative to outside it. Neither of these sharp peaks is present in a "flow-off" data set, taken with the wire operating at the same temperature as during a run with all tunnel electronics prone to interference (e.g. traversing mechanism, tunnel heaters) active, but in a quiescent test section. However, it is still expected that these peaks may be related to probe vibration and/or strain-gaging effects rather than actual flow phenomena. These probe effects may indeed manifest in the signal only under the presence of flow and have their frequencies modified by either the changing velocities or effective overheat ratio in the boundary layer. This will be investigated in detail in future work. As mentioned in Section 4.1, the first step in determining the cause of these sharp peaks will be to follow established guidelines (Kovasznay 1953, Smits *et al.* 1983, Smits & Dussauge 1989) by providing

slack in the wire and/or dampening on the mounting joints to minimize the detrimental effects of strain-gaging and vibration.

Spectra at the locations of maximum RMS voltage at each axial location are extracted from Figure 6–6 and plotted together in Figure 6–7.

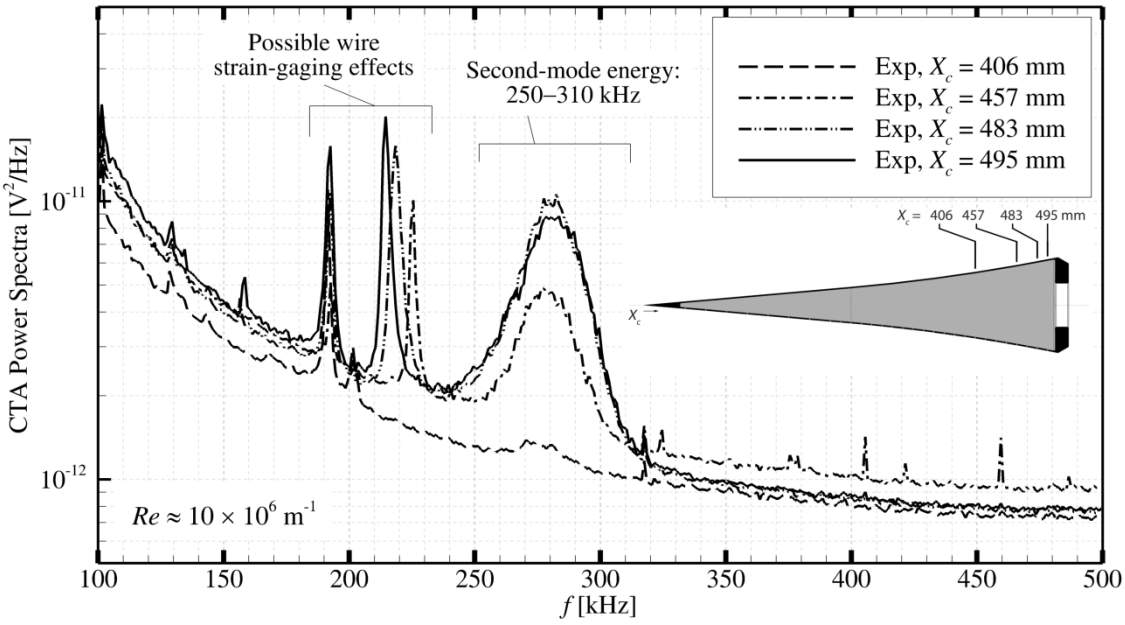

Figure 6–7. Spectra from the maximum-RMS heights at axial stations surveyed.

This view offers more quantitative insight into the development of frequencies and amplitudes along the cone axis. Significant growth of the second-mode energy content is observed between X_c = 406 mm to 483 mm, but amplitudes between X_c = 483 mm and 495 mm remain largely unchanged. Additionally, one can observe the center of the energy band indeed shifting slightly toward higher frequencies at downstream stations (e.g. between X_c = 406 mm to 483 mm), as expected due to the

slight thinning of the boundary layer in accordance with the pressure gradient imposed by the flare. A comparison between these spectra and computed *N*-factors from stability computations is presented next.

6.5. Instability growth and comparison to computation

6.5.1. Computational methods

Stability computations were conducted for comparison with experiment using an internally developed stability code, JoKHeR, described in detail by Kuehl *et al.* (2012) and Reed *et al.* (2012). This code calculates first- and second-mode and crossflow stability in a 3D boundary layer but is restricted to assume that the flow is uniform perpendicular to the chosen arbitrary marching path. It is written in a general orthogonal curvilinear coordinate system and uses a primitive variable formulation. Analyses using linear stability theory (LST) and the linear parabolized stability equations (LPSE) are considered in this work.

6.5.1.1. Linear stability theory

Linear stability theory (LST) has been the most widely used approximate method for stability analysis in the aerospace community. In this approach, the total flow is separated into a steady basic state and an unsteady disturbance of the form $\phi(y)e^{i(\alpha x+\beta z-\omega t)}$. The basic state is, itself, a solution to the full Navier-Stokes equations and represents the flow that exists in the absence of any environmental disturbances or forcing. The basic state is assumed locally parallel so that the wall-normal velocity is set

to zero and the flow quantities are functions of the wall-normal direction only. The disturbances are assumed to be small enough, allowing the nonlinear terms to be neglected. With these approximations and homogeneous boundary conditions, the disturbance equations feature coefficients which depend on the wall-normal coordinate only, and thus the separation of variables into normal modes is possible. This results in a local eigenvalue problem. The inclusion of surface and trajectory curvature terms in this formulation is not standard, as they tend to balance the neglected nonparallel boundary layer effect. However, in the case of cones and other highly curved bodies, these curvature terms play a significant role and are therefore retained in the present LST analysis.

6.5.1.2. Parabolized stability equations (PSE)

The parabolized stability equations (PSE) lie between the extremes of LST and direct numerical simulations (DNS) and account for curvature, nonparallel, and nonlinear effects. Validation of the PSE with experiments has been proven by the community; with appropriate modeling of the operating and disturbance input conditions, the agreement among theory, computations, and experiments has shown to be remarkable.

As with LST, the flow is decomposed into a basic state plus a disturbance, and one assumes the basic state to be a solution to the original equations of motion. A scaling analysis based on the slow growth of the boundary layer in a direction parallel to the surface (for example, the local inviscid streamline direction) allows second derivatives

in that direction to be neglected, which nearly parabolizes the disturbance equations and permits a marching solution. Unless otherwise stated, we will refer to the local marching direction, the wall normal direction, and the mutually perpendicular direction to the prior two as x, y, and z, respectively.

For quasi 3-D disturbances, the variables $\phi = \left[u, v, w, \rho, T\right]^T$ take the form

$$\phi\left(x, y, z, t\right) = \bar{\phi}\left(\bar{x}, y\right) + \phi'\left(x, y, z, t\right), \tag{6.2}$$

and Fourier (normal mode) decomposition of the disturbances leads to

$$\phi' = \sum_{-K}^{K} \sum_{-K}^{K} \left[\tilde{\phi}\left(\bar{x}, y\right) A\left(x\right) e^{i\left(k\beta z - n\omega t\right)} \right], \tag{6.3}$$

where $\bar{x} = x / Re$ and $A\left(x\right) = e^{i\int \alpha(\bar{x})dx}$ with complex streamwise wave number $\alpha\left(\bar{x}\right)$. A normalization condition is applied to the shape function, $\tilde{\phi}\left(\bar{x}, y\right)$, in order to maintain the assumption that the shape function is slowly varying in the marching direction. Thus, exponential growth is accounted for by the amplitude function, $A(x)$, leaving the shape function amplitude order one. Harmonic balancing is used to identify nonlinear modal interactions, though in the present work linear PSE (LPSE) is applied in which nonlinear effects are neglected and only a single monochromatic wave is considered.

6.5.2. Computational results and comparison with experiment

Using the basic state results selectively shown in Figure 6–4, local growth rates from LST were computed and are presented in Figure 6–8. As expected, the frequencies for significant local growth rates for the second mode instability are highly tuned to the boundary-layer thickness.

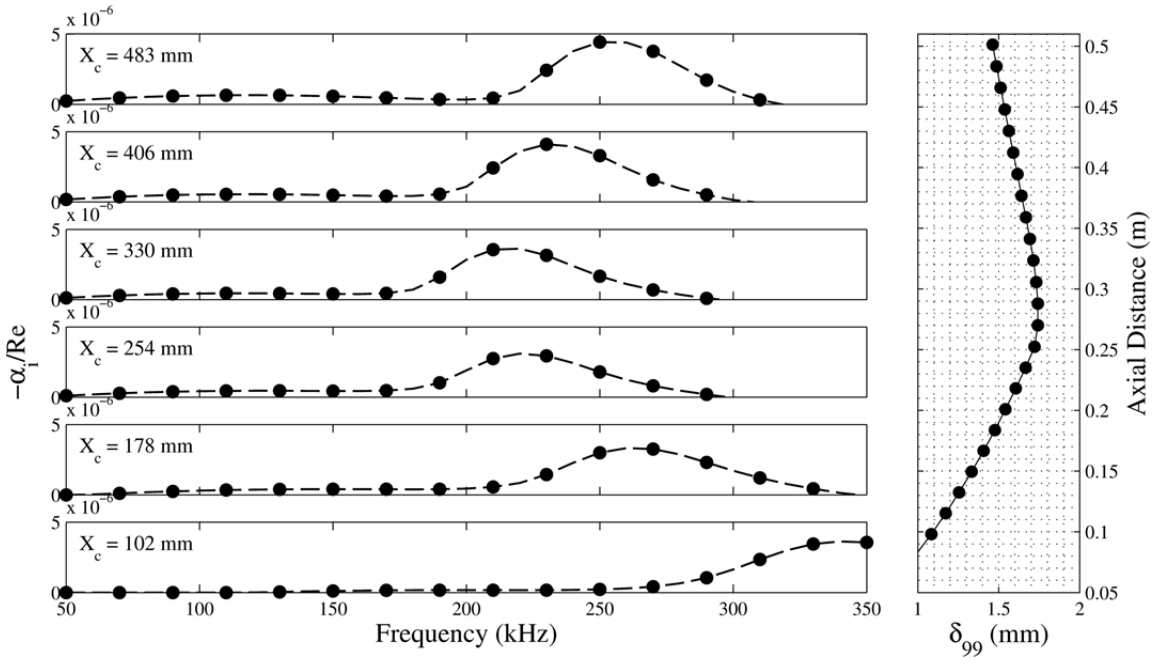

Figure 6–8. LST-computed local growth rates along the cone axis.

Although the LST calculation of Figure 6–8 is both readily obtained and instructive in demonstrating the high degree of sensitivity of the unstable second-mode passband to boundary-layer thickness, the LPSE technique was used for subsequent analyses due to its inclusion of curvature and nonparallel effects. First, Figure 6–9 presents normalized, LPSE-computed mode shapes of mass flux perturbations for the locally most-amplified frequency, with comparison to experimental profiles of fluctuating voltage at each axial station on the cone. In contrast to the broadband RMS profiles presented in Figure 6–3, the RMS profiles here are generated from data filtered to include only the 230–330 kHz passband where the second mode is observed in order to more-directly compare to the single-frequency LPSE profiles. The agreement in instability mode shapes here is excellent, with locations of maximum RMS only

diverging from the computation slightly at the last two axial stations in an amount commensurate with the divergence in observed δ_{99} seen in Figure 6–5, likely attributed to the early stages of transition onset.

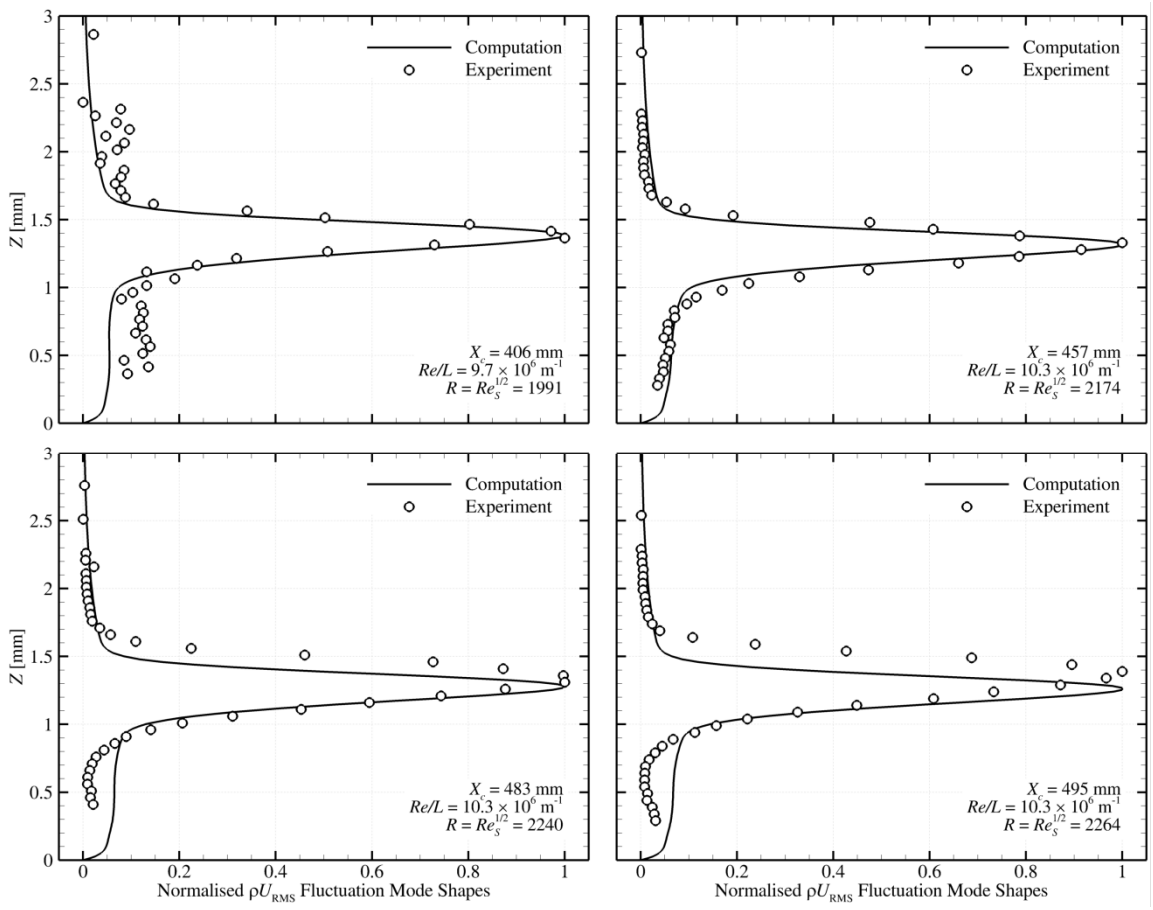

Figure 6–9. Experimental and LPSE-computed instability mode shapes. Computational mode shapes are of fluctuating mass flux for locally-most-amplified frequencies; experimental fluctuating voltage profiles are filtered to the second-mode passband, 230–330 kHz.

To determine integrated growth for comparison to experiment, *N*-factors were computed from amplitudes of mass flux disturbances calculated using LPSE. These are

shown in Figure 6–10 for frequencies between 180 kHz and 312 kHz. At X_c = 0.44 m, where transition onset was observed in the surface temperature data of Section 6.2, the *N*-factor is approximately 13.5.

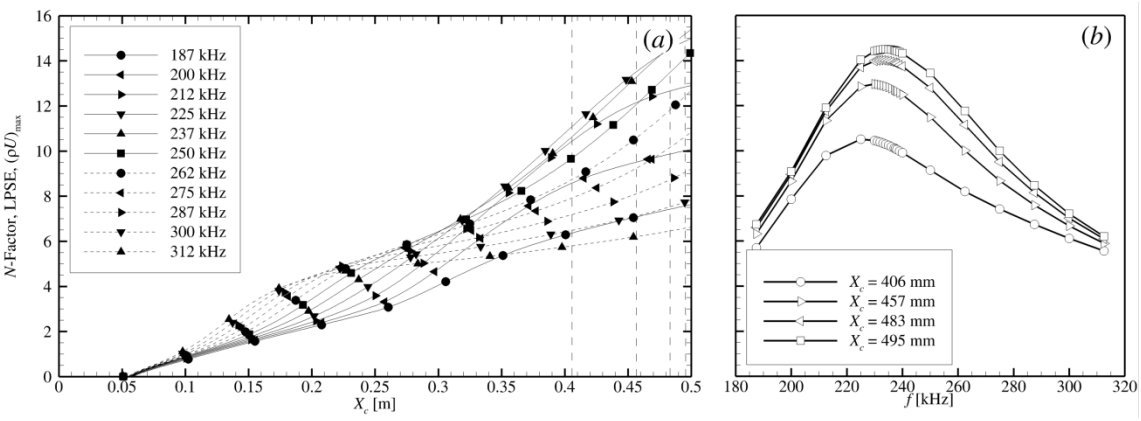

Figure 6–10. LPSE-computed *N*-factor evolution along the cone. Shown (*a*) for various frequencies with streamwise development along the cone axis, and (*b*) versus frequency for the four axial stations surveyed experimentally.

Figure 6–11 provides a comparison of the experimental spectra of Figure 6–7 with the LPSE *N*-factor results of Figure 6–10 at each of the surveyed axial stations on the cone. Because the hot-wire data are currently uncalibrated, proper scaling of the experimental spectra relative to the LPSE *N*-factor results is not possible, and meaningful comparisons of relative amplitude growth cannot be made. It remains instructive, however, to notionally plot the two data sets together to identify frequencies for peak growth and how they evolve downstream. Most evident in Figure 6–11 is the key discrepancy between experiment and computations: the most amplified frequency increases from f_0 = 226 kHz at X_c = 0.4 m to f_0 = 236 kHz at X_c = 0.50 m as computed by

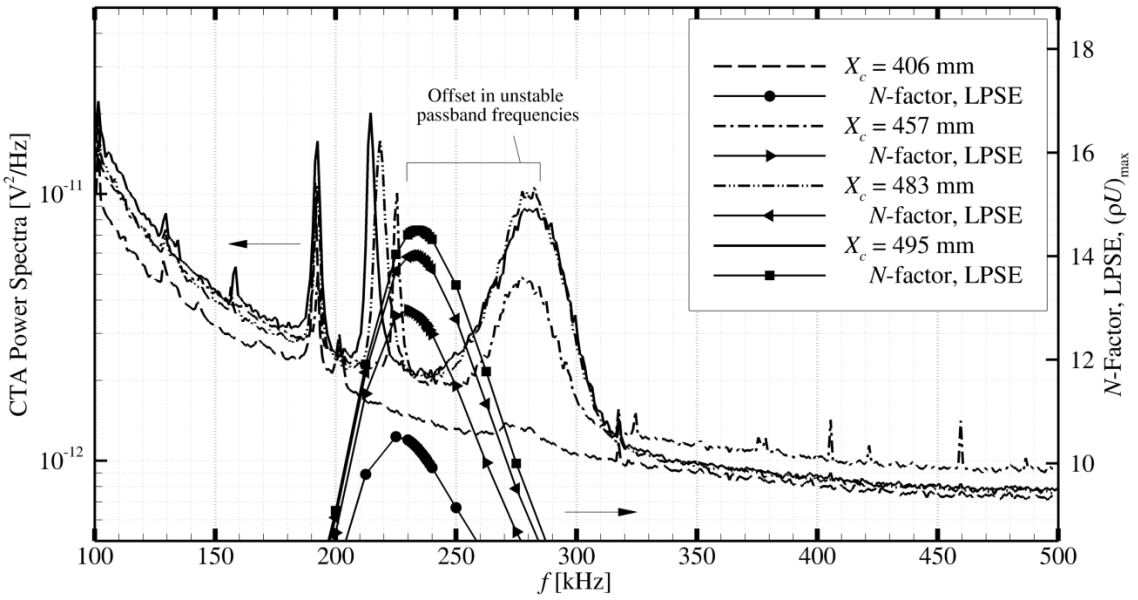

Figure 6–11. LPSE *N*–factors compared with experimental spectra. At each axial station, spectra are those taken at the local height of maximum RMS.

the LPSE method, whereas the experimental data show the center of energy near $f_0 = 280$ kHz. This seems to contradict the comparison between computed and experimental boundary-layer thickness presented in Figure 6–5, which would have suggested slightly *lower* experimental second-mode frequencies due to the relatively higher observed δ_{99}. However, it is important to again highlight the many complications with the current notional comparison of computed and experimental δ_{99}, from lack of calibration to cone wall temperature variation. Considering these complications in comparing δ_{99}, the agreement in the unstable frequency band is the more appropriate indicator of agreement between computation and experiment. Two key remaining issues in the computation may affect this agreement: (1) the slight windward misalignment of the model not accounted for in the 2-D simulation, and (2) the non-uniform experimental

cone wall temperature, currently modeled in the simulation as a constant. It remains possible that implementing the slightly windward misalignment of the cone in the computation will thin the computed boundary layer and increase the computed frequencies for second-mode growth to more closely match experiment. Similarly, implementing the non-uniform average cone wall temperature will better model the evolution of the boundary-layer thickness, affecting local growth rates and frequencies for peak integrated growth. All of these effects are being quantified in on-going computational and experimental studies, the first of which is described below in Section 6.6.

6.6. Cone misalignment sensitivity determination with optical diagnostics

The above comparisons between LPSE simulations and experiments using hot-wire anemometry revealed a discrepancy in the observed and expected frequencies of the second-mode instability. As was seen in Figure 6–11, computed most-amplified frequencies for the second mode at zero angle of attack were over 40 kHz lower than those observed in the hot-wire experiments (234 kHz versus 280 kHz, respectively). Figure 6–12 again provides a comparison of power spectra from experiment for X_c = 495 mm and $Re = 10\times10^6$ m^{-1}. Additionally included here are data acquired using the focused schlieren diagnostic described in Section 4.3 and leveraged more extensively in Section 7. Computations of integrated growth from LPSE are shown as well.

Possible explanations for this discrepancy are numerous, including model misalignment along the measurement ray, wall temperature variations not fully

accounted for in the simulation, or possibly an under-damped hot-wire transfer function artificially amplifying higher frequencies. Believed to be dominant among these was the effect of slight model misalignment, although the sensitivity to this was not well understood.

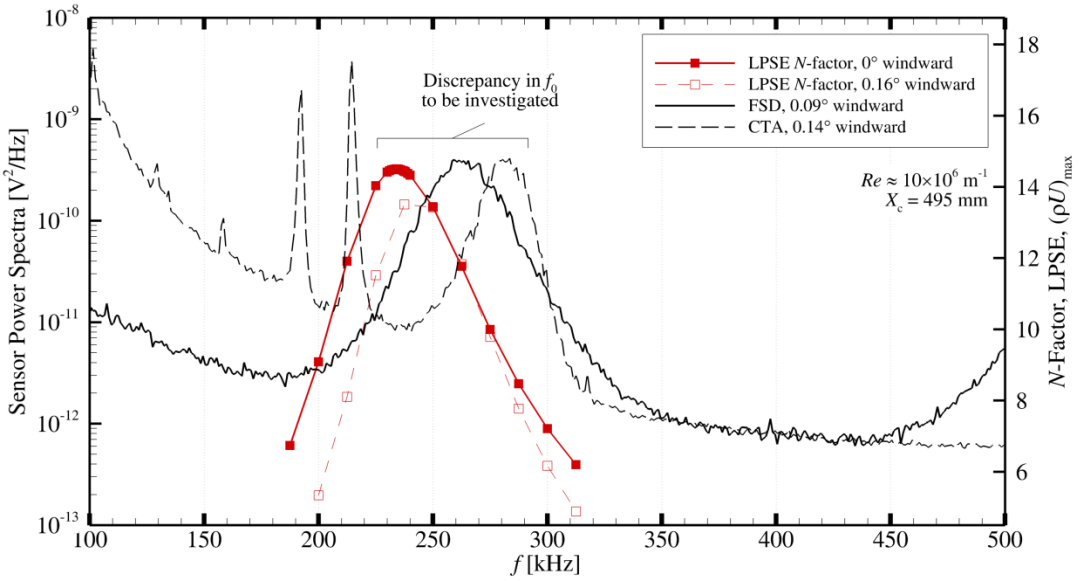

Figure 6–12. Second-mode spectra from CTA and FSD experiments and LPSE. X_c = 495 mm. Re = 10×10^6 m^{-1}. Significant discrepancy in f_0 motivates investigation into sensitivity to model incidence and other factors.

In order to experimentally determine the sensitivity of f_0 to small angles of incidence, the model incidence was set for each in a series of 8 runs to a different pitch angle between -1º and +1º, taking care to minimize the yaw angle, which was typically kept under 0.2º. Geometric alignment for each run was quantified using the confocal laser scan method described in Section 3.1.3. The robust, non-intrusive nature of the focused schlieren system made it an excellent candidate for a tedious campaign such as

this, which required a substantial amount of work inside the test section between runs, carefully manipulating the model alignment and then setting up and conducting a new scan with the confocal laser each time.

For each run, a typical Reynolds number sweep was conducted. From the $Re = 10\times10^6$ m^{-1} condition, an averaged spectra was computed, from which the fundamental frequency, f_0, was programmatically identified. Figure 6–13 shows the values of f_0 identified for each of the model incidences at $Re = 10\times10^6$ m^{-1} as empty circular markers. Also plotted here are the curious hot-wire data from Sections 6.4 and 6.5 as well as three LPSE-computed results from the work of Perez *et. al.* (2012). The slope of the best-fit line through the deflectometry data is –84 kHz per degree (or 8.4 kHz per a mere 0.1º misalignment). Note in particular the red error bars of Figure 6–13. These serve to provide a notional prediction of the effect of small out-of-plane misalignment (< 0.3º for each point) as measured by the laser scan technique. When the measurement ray is under a nominally windward condition, any out-of-plane misalignment serves to thicken the boundary layer and reduce f_0. When the measurement ray is under a nominally leeward condition, any out-of-plane misalignment thins the boundary layer, and increases f_0. Because the effect of this is one-sided, the 8.4 kHz/0.1º best-fit slope is necessarily over-predicted for purely in-plane misalignments. The three data points available from the LPSE computations (blue squares) show a sensitivity of 6.5 kHz per 0.1º – indeed, a shallower slope. Regardless, this direct knowledge of a practical sensitivity to pitch misalignment within practical limits of attainable out-of-

plane residual misalignment is valuable for motivating an increased level of caution when installing and aligning the model for second-mode study at 0º nominal incidence.

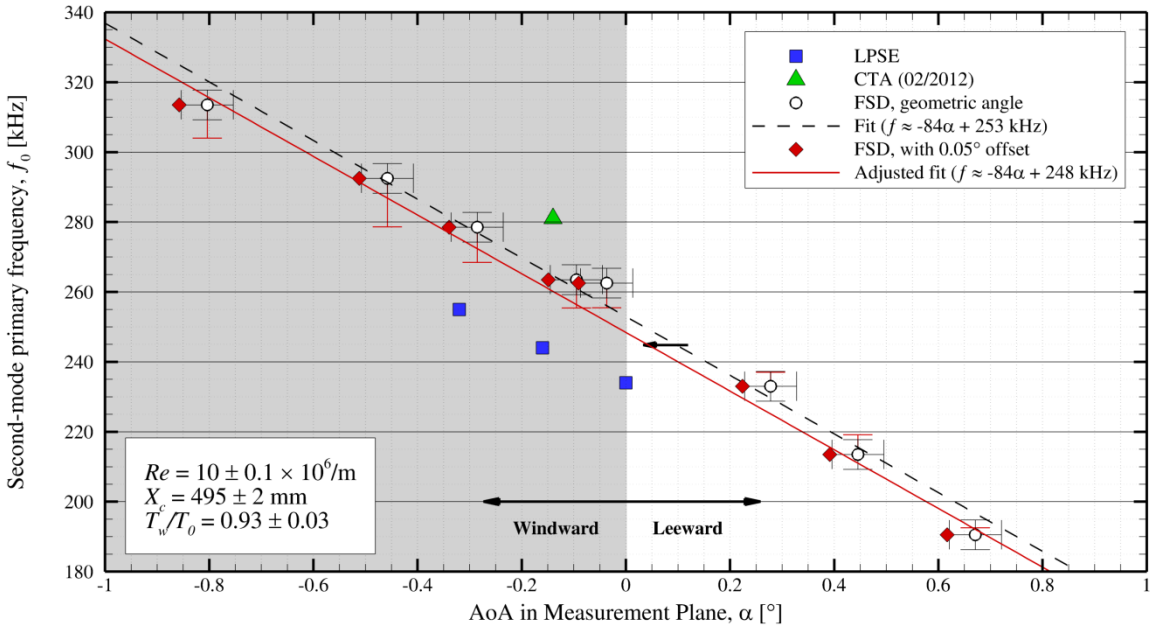

Figure 6–13. Experimentally-observed variation in f_0 versus model angle of attack. Empty circles denote data at geometric angle of attack, while red circles are corrected for an estimated 0.05º offset derived from the data of Figure 6–14. Black error bars denote uncertainty in the laser-scan alignment technique. Red error bars provide a notional estimate of the effect of residual out-of-plane misalignment.

Subsequent to these eight runs, the focused schlieren apparatus was repositioned such that the fiber optic was located at $X_c = 495$ mm on the *underside* of the model, and the final run of the angle-of-attack campaign was repeated. For this run, the geometric alignment was indicated as 0.04º windward in pitch, with an indicated yaw misalignment of 0.1º. For these runs, the unit Reynolds number was varied from 6.5 to 10.5×10^6 m^{-1}, and the frequencies of the first two peaks of instability were again identified

programmatically. Plotted in Figure 6–14 are the frequencies f_0 and $2f_0$ versus Re for the measurements on the upper and lower rays. Considering specifically the case of $Re = 10.0\times10^6$ m^{-1}, a difference in f_0 of 15.4 kHz is observed between instabilities on the upper and lower rays of the cone.

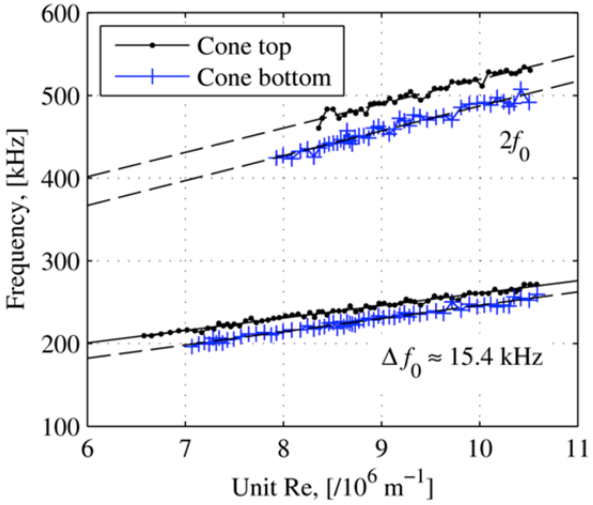

Figure 6–14. Fundamental and harmonic frequencies f_0 and $2f_0$ vs. Re. Shown for both upper and lower cone surfaces. X_c = 495 mm.

Comparing this 15.4 kHz frequency difference to the observed 8.4 kHz-per-0.1º misalignment sensitivity, one can hypothesize that the upper ray of the model is at an 0.09º windward misalignment, not 0.04º as was determined geometrically. The 0.05º offset between these two values is relatively small, and is within the assumed repeatability of the laser-scan alignment technique. Still, a systematic difference between aerodynamic and geometric alignment is possible. As one possibility, one might conjecture that the nozzle wall boundary layer may be slightly thicker on its upper

surface than below, as it is likely the nozzle wall temperature may be higher on the upper surface following periods of convective preheating or natural convection in periods of idle time between runs. This would indeed bias the nozzle flow slightly down upon the model, creating a windward condition on the upper surface. This temperature non-uniformity has yet to be explicitly quantified at the Texas A&M M6QT, but a similar effect has been observed at the Boeing/AFOSR Mach 6 Quiet Tunnel at Purdue University (Steen 2010).

If we assume that this alignment offset is based entirely on a nozzle effect – and therefore constant for the various model alignments tested, we can apply this shift uniformly to the previous data set as depicted by the red markers in Figure 6–13. Indeed, this offset effect indeed brings the experimentally observed frequencies closer to those calculated by LPSE methods. A significant difference between experiment and computation remain; 10 to 15 kHz remain unaccounted for. This could still be an artifact of the thermal state of the model, nose bluntness, misalignment or flow angularity about the yaw axis, or other effects. However, now that the sensitivities are known, it is valuable to be able to confidently state that the remaining difference between experiment and computation amounts to perhaps only 0.2º in model misalignment. Although this number is small and may be regarded as within practical limits of error, the effect on f_0 is large, motivating even closer collaboration between experiment and computation, as well as improved model alignment adjustment & characterization techniques for future work.

7. HIGH-BANDWIDTH OPTICAL MEASUREMENT OF THE SECOND-MODE INSTABILITY AND ANALYSIS OF NONLINEAR INTERACTIONS*

7.1. Overview

The focused schlieren deflectometry (FSD) optical diagnostic was originally implemented and employed in the M6QT as a simple, inexpensive complement to hot-wire anemometry in order to provide additional confidence in the dynamic hot-wire results and to serve as a robust diagnostic for the cone misalignment sensitivity campaign of the previous section. During these efforts, however, an iterative optimization of the system components provided a measurement bandwidth of approximately 1 MHz and high signal-to-noise ratio. At a wide range of unit *Re* conditions prior to the loss of quiet flow, the FSD revealed in the cone boundary layer not only the most-amplified second-mode frequency f_0, but the presence and growth of significant disturbance content at $2f_0$ and $3f_0$ not detectable with the hot-wire diagnostics used previously. This observation was not unexpected, but the availability and richness of the FSD data provided an opportunity for further study expanding upon other historical work.

A variety of pioneering hypersonic stability experiments in the 1980's observed disturbance growth in hypersonic laminar boundary layers at significantly higher frequencies than the most-unstable second mode (see Stetson 1988 and the references

* Portions of this section are reprinted with permission from "High-Bandwidth Optical Measurements of the Second-Mode Instability in a Mach 6 Quiet Wind Tunnel" by Hofferth, J. W., Humble, R. A., Floryan, D. C., and Saric, W. S., 2013. *AIAA Paper 2013–0378*, Copyright 2013 by the American Institute of Aeronautics and Astronautics, Inc.

cited therein). Linear stability theory could not account for these unstable frequencies, and their precise identity at the time could not be determined. It was known, however, that these dominant frequencies were two and three times the most-unstable second-mode frequencies, and they did not occur until significant second-mode growth had taken place. This led to the belief that they were in fact harmonics of the second mode, and were being generated by nonlinear interactions. It soon became clear that evaluation of nonlinear effects must be a prerequisite to the application of linear stability theory (LST) to hypersonic problems (Stetson 1988).

Higher-order spectral techniques, such as the bispectral analysis, have demonstrated great practical utility in characterizing nonlinear interactions (see Kim & Powers 1979). In an influential paper, Kimmel & Kendall (1991) first utilized the bispectrum to examine the effects of nonlinear interactions in a hypersonic laminar boundary layer under conventional freestream conditions. They found that nonlinearity explained the generation of a harmonic of the most-unstable second-mode disturbance, but questions remained regarding the influence of the conventional freestream disturbance environment. Motivated by this work, Chokani (1999) carried out the first bispectral analysis under low-disturbance (so-called "quiet") freestream conditions, to determine if there were any differences in nonlinear disturbance behavior. He found essentially the same harmonic generation of the second mode, but also an initial difference interaction within the sidebands that was then followed by a possible low-frequency modulation, as initially suggested by Kimmel & Kendall (1991).

The basic structure of the second-mode disturbances; namely, that they are two-dimensional oscillations primarily in density rather than velocity, has motivated the implementation of optical-based measurement techniques (see Laurence *et al*. 2012). Recently, VanDercreek (2010) applied focused schlieren in combination with a photomultiplier tube to study the second-mode instability on a 7-degree straight cone at Mach 10 in AEDC's Tunnel 9. He observed photomultiplier signal frequencies consistent with those measured with PCB® pressure sensors embedded in the model surface. Laurence *et al*. (2012) have also recently obtained time-resolved schlieren visualizations to determine the structural and propagation characteristics of second-mode instability waves within a hypersonic boundary layer. Almost all other previous hypersonic stability experiments – including those of Chokani in the M6QT at NASA Langley – have used single-point, hot-wire anemometry. The attendant limited frequency response, which is typically O(400 kHz), has hampered efforts to identify potentially higher harmonics and provide a more complete picture of the second-mode disturbance evolution process.

In the present study, it is therefore interesting to revisit previous second-mode instability measurement efforts in the low-disturbance freestream environment using the focused schlieren deflectometry (FSD) system described in Section 4.3, in view of the impressive spectral range achievable (in the present case, up to 1 MHz).

7.2. Bispectral analysis

A brief description of the bispectral analysis is provided to aid the interpretation of the results later on. Consider a fixed location within the cone boundary layer where a finite record of fluctuating light intensity is extracted as the data series $I'(n)$, $n = 0, 1, \ldots, T-1$, where T is the length of the time-series data. This time series can be divided into K segments, $i = 0, 1, \ldots, K-1$, each of length M. Let the ith segment of $I(n)$ therefore be $I_i(n)$, $n = 0, 1, \ldots, M-1$. The auto-bispectrum $B_i(f_1, f_2)$ may be computed by

$$B_i(f_1, f_2) = X_i(f_1) X_i(f_2) X_i^*(f_1 + f_2), \tag{7.1}$$

where f is a discrete frequency, * is the complex conjugate, and $X_i(f)$ the ith discrete Fourier transform (DFT) for each segment. In practice, estimates from all K segments may be averaged to give

$$B(f_1, f_2) = \frac{1}{K} \sum_{i=0}^{K-1} B_i(f_1, f_2). \tag{7.2}$$

The bispectrum $B(f_1, f_2)$ is a measure of the degree of nonlinear quadratic phase coupling between the signal components at frequencies f_1 and f_2. Phase coupling occurs when the sum of the phase of the frequency components f_1 and f_2 is equivalent to the phase of the sum frequency $(f_1 + f_2)$. If the triad of waves f_1, f_2 and $(f_1 + f_2)$ are nonlinearly coupled, then $f_1 + f_2 \rightarrow (f_1 + f_2)$, where "$\rightarrow$" denotes "generates by phase-coupled interaction" (see e.g., Chokani 1999). Furthermore, because the phase at the sum frequency, ϕ_3, is simply the sum of the phases of the component frequencies, $\phi_1 + \phi_2$, then the biphase $\phi(f_1, f_2)$ at that frequency will be zero (or small), where the bicoherence is relatively high. Statistical averaging ensures that only meaningful nonlinear coupling

between frequency components are retained. The bispectrum therefore discriminates between nonlinearly coupled waves and spontaneously excited waves, because spontaneously excited waves are generated independently of the other components, and thus have independent amplitudes and phases.

By virtue of the bispectrum symmetry,

$$B(f_1, f_2) = B(f_2, f_1) = B(-f_1, -f_2) = B(-f_1, f_1 + f_2), \tag{7.3}$$

which limits the total (useful) area to

$$0 \le f_2 \le (f_N / 2), f_2 \le f_1 \le (f_N - f_2), \tag{7.4}$$

where f_N is the Nyquist frequency. There are a few difficulties, however, with the direct implementation of the bispectrum in this way. In particular is the fact that energetic spectral components with a moderate degree of phase coherence can dominate weaker spectral components with a higher degree of phase coherence. To resolve this and other issues, Kim & Powers (1979) suggest the use of the squared bispectrum, normalizing such that

$$b^2(f_1, f_2) = \frac{\left|B(f_1, f_2)\right|^2}{E\left[\left|X(f_1)X(f_2)\right|^2\right] E\left[\left|X(f_1 + f_2)\right|^2\right]}, \tag{7.5}$$

where E is the expectation operator and $b^2(f_1, f_2)$ is known as the *bicoherence*. In what follows, the bicoherence is used, the advantage being that it is bounded by 0 and 1. A bicoherence of zero means completely independent waves, whereas a value of unity means completely coupled waves. It is worth noting that this is not the only way of normalizing the bispectrum (see Hinich & Wolinksy 2005 for further discussion), although it is one of the most popular and is sufficient for the present purposes. Due to

the normalization, the symmetry relations for the bicoherence are different from the bispectrum. A symmetry has been lost, and we now have

$$b^2(f_1, f_2) = b^2(f_2, f_1) = b^2(-f_1, -f_2). \tag{7.6}$$

7.3. Time series and power spectral density

To motivate the discussion, a time series segment (0.5 ms) of the photodetector signal is shown in Figure 7–1 for each of the unit Reynolds numbers considered. Each case was obtained during the same run, and has been digitally high-pass filtered at 100 kHz to highlight the second-mode fluctuations. The fiber optic measurement location for all runs shown is $X_c = 495$ mm. Note that because the fiber optic height is fixed throughout the run, during which the boundary-layer thickness and height of maximum fluctuation change with *Re*, amplitudes should not be directly compared. For each $Re < 10.7\times10^6$ m^{-1}, second-mode disturbances within the range 210–280 kHz are clearly observed. In each case, these instabilities appear in wave packets, with an amplitude envelope much lower in frequency. With increasing *Re*, the signal becomes increasingly irregular. By $Re = 11.0\times10^6$ m^{-1}, the signal appears fully turbulent. This behavior is expected, given the known loss of quiet flow in the M6QT freestream by approximately $Re = 10.7\times10^6$ m^{-1}; in this regard, the observed breakdown to turbulence is not a "natural" process in the conventional sense.

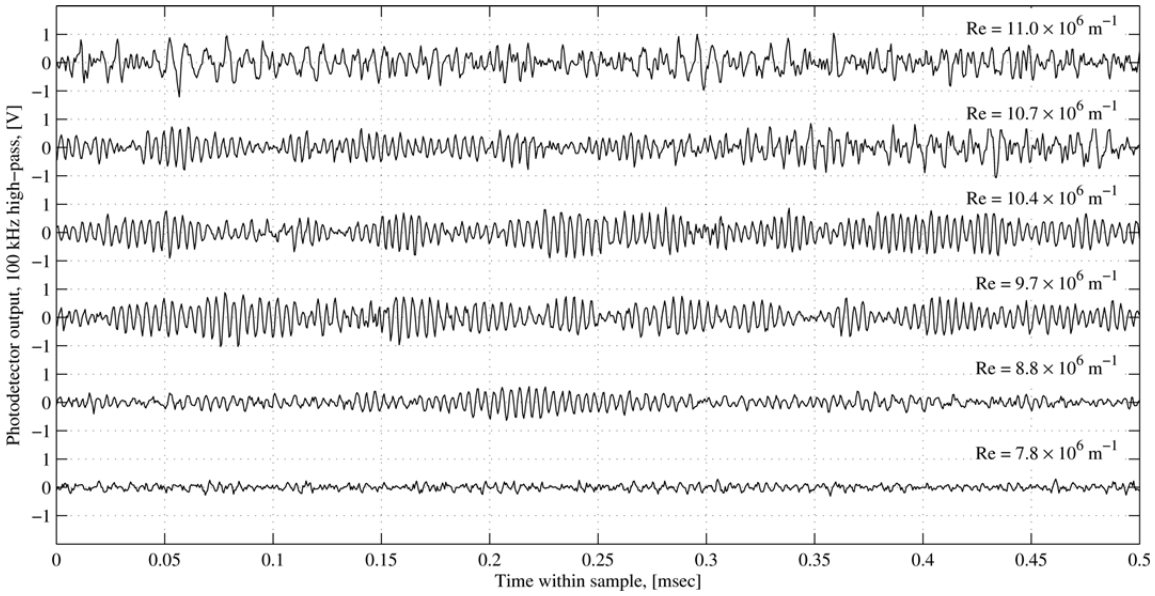

Figure 7–1. Segments of photodetector output time series for select unit *Re*. All segments were obtained during a single run. Voltages are high-passed at 100 kHz to highlight second-mode content between 210–280 kHz for $Re < 10.7\times10^6$ m^{-1}.

The global evolution of the spectral content with *Re* is depicted in Figure 7–2(*a*). Spectra are computed for each 100 ms segment of the run using Welch's method, averaging 50 windows with 75% overlap. At the lowest Reynolds number considered of 7.8×10^6 m^{-1}, only the second-mode frequency f_0 is essentially observed. Harmonics at $2f_0$ and then $3f_0$ become visible as *Re* increases, albeit at lower amplitudes. Note also that the frequencies of the instabilities increase gradually with increasing *Re*, due to the tuning of the second-mode instability to the boundary-layer thickness, δ. A turbulent state abruptly appears at approximately $Re = 10.7\times10^6$ m^{-1}.

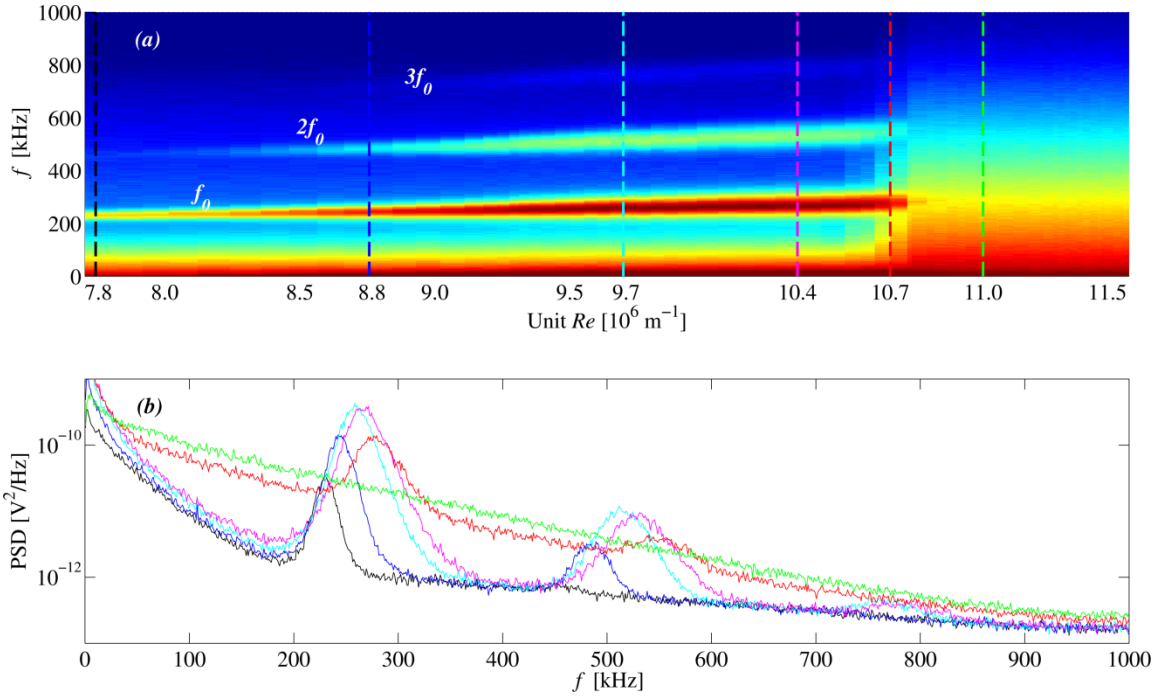

Figure 7–2. Evolution of photodetector spectra vs. unit *Re*. X_c = 495 mm. (*a*) Spectrogram of photodetector power spectral density variation with unit *Re* during a single run. Each power spectrum is averaged over 100 ms of runtime. *Re* = 7.8 to 11.5×10^6 m^{-1}. (*b*) Power spectra at select *Re* taken from (*a*).

Figure 7–2(*b*) shows extracted power spectral densities for the selected unit Reynolds numbers shown, denoted by the dotted lines in Figure 7–2(*a*). The second-mode amplitude increases with increasing *Re*, and then by *Re* = 10.7×10^6 m^{-1}, as the onset of turbulence is imminent, the well-defined peaks of the instability have fallen in amplitude. This is accompanied by valleys at frequencies between the harmonics, which become filled in with broadband fluctuation of turbulence. This suggests the possibility of an energy transfer between the modes. However, a major limitation of this representation is that phase information is lost in the Fourier analysis. To investigate the

nonlinear interactions that give rise to the behavior observed, we turn to a bispectral analysis.

7.4. Analysis of nonlinear interactions

To examine the nonlinear phase-coupled quadratic interactions that give rise to the spectral components described above, a bispectral analysis is carried out. Figure 7–3 shows the magnitude of the normalized bispectrum magnitude, or bicoherence, $b^2(f_1, f_2)$. The bicoherence plots were computed from the unamplified, unfiltered photodetector signal using Hanning windows 256 points in length, with 50% overlap. For clarity, only results for sum interactions within the range (0, 0), (f_N, f_N), (f_N, 0), and for difference interactions within the triad (0, 0), (f_N, 0), (f_N, $-f_N$) are shown.

The results suggest the boundary layer contains a variety of quadratic phase-coupled interactions that appear to undergo a distinct evolution with unit Reynolds number. At $Re = 7.8\times10^6$ m^{-1}, the genesis of nonlinear interactions is just occurring, with weak sum interaction $f_0 + f_0 \rightarrow 2f_0$ and difference interaction $2f_0 - f_0 \rightarrow f_0$. These interactions describe the very early stages of the second-mode's nonlinear growth. Prior to this, the second mode undergoes a purely linear (exponential) growth; in this case no bicoherence peaks are expected to be present.

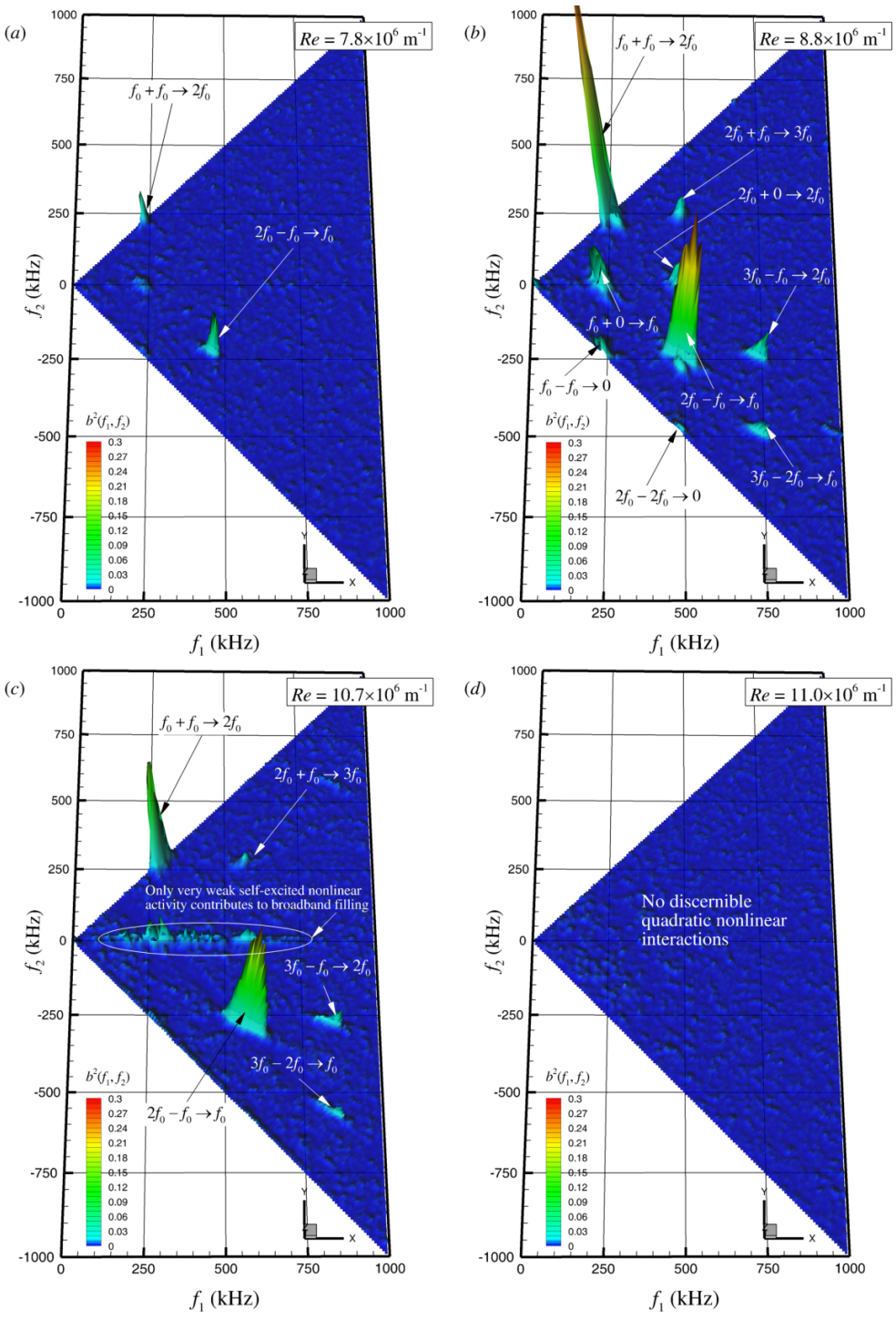

Figure 7–3. Bispectral analysis of the photodetector signal. X_c = 495 mm. (*a*) $Re = 7.8\times10^6$ m^{-1}, (*b*) 8.8×10^6 m^{-1}, (*c*) 10.7×10^6 m^{-1}, (*d*) 11.0×10^6 m^{-1}. Contours of bicoherence magnitude, $b_2(f_1, f_2)$, are shown from 0 to 0.30 in increments of 0.03. See text for further details.

At $Re = 8.8\times10^6$ m^{-1}, a variety of nonlinear interactions emerge, indicating that the second mode undergoes significant nonlinear growth. Because the boundary layer is developing under natural forcing from freestream disturbances, the possibility exists that $2f_0$ (and $3f_0$ etc.) is an independent, spontaneously excited wave. This cannot be determined from the power spectral density alone because phase information is lost. However, from the bicoherence analysis it appears that $2f_0$ is the result of nonlinear wave propagation, because a phase relation exists between f_0 and $2f_0$. This has been observed by Chokani (2005). Sum interactions exist involving the self-excited interaction $f_0 + f_0 \rightarrow 2f_0$, and $2f_0 + f_0 \rightarrow 3f_0$. Thus, a small disturbance at f_0 can reinforce itself substantially and transfer energy to the higher harmonics. Furthermore, because the phase at the sum frequency, ϕ_3, is simply the sum of the phases of the component frequencies, $\phi_1 + \phi_2$, then the biphase $\phi(f_1, f_2)$ at the frequencies associated with significant bicoherence were zero (or at least small).

In addition, the difference interaction $2f_0 - f_0 \rightarrow f_0$ is observed, consistent with the work of Chokani (2005) also under low-disturbance freestream conditions. This is accompanied by somewhat weaker interactions involving $f_0 + 0 \rightarrow f_0$ and $2f_0 + 0 \rightarrow 2f_0$, whose concentration along the abscissa indicates that the valleys between the spectral peaks observed in the power spectrum are being filled. Barely perceptible interactions are also present at $f_0 - f_0 \rightarrow 0$ and $2f_0 - 2f_0 \rightarrow 0$ (running along the lower diagonal line), which would suggest that the second mode and $2f_0$ lead to mean flow distortion. This is consistent with the fact that the boundary-layer profiles still have the characteristics of a laminar boundary layer, in spite of the existence of these large disturbances (§6.3). The

elongated appearance of the bicoherence peaks suggests that the second mode is coupling with frequencies in its sidebands, serving to broaden the bands of the harmonics. Notice how in the earlier stages of the (nonlinear) transition process at $Re = 7.8\times10^6$ m^{-1}, the bicoherence contours appear more circular and more localized in bifrequency space. It is interesting to observe even higher-order harmonic interactions, involving $3f_0 - f_0 \rightarrow 2f_0$ and $3f_0 - 2f_0 \rightarrow f_0$, indicating that ultrahigh frequency components play a role in the nonlinear evolution of the disturbances. These are not generally accessible via hot-wire anemometry, and have not hitherto been reported in the literature.

As the unit Reynolds number increases to $Re = 10.7\times10^6$ m^{-1}, the nonlinear interactions outlined above decrease in bicoherence magnitude. Inspection of the time series reveals that phase-coupled nonlinear interactions take place increasingly intermittently (see also following subsection). The ensemble-averaged bicoherence magnitude therefore decreases. Interactions also occur involving $f_0 + \delta f \rightarrow (f_0 + \delta f)$ and $f_0 - \delta f \rightarrow (f_0 - \delta f)$, as well as $2f_0 + \delta f \rightarrow (2f_0 + \delta f)$ and $2f_0 - \delta f \rightarrow (2f_0 - \delta f)$, where δf spreads along much of the sideband extent. This has also not been previously observed (cf. Chokani 2005), at least not to the same extent. These interactions portray the valleys between the spectral peaks observed in the power spectrum being increasingly filled. However, the very small magnitude of these spectra-filling interactions (< 0.05) supports the earlier observation that the broadband spectral content at this unit Re arises as a result of the onset of tunnel noise – an external forcing poorly phase-correlated with the instabilities on the cone. It is interesting to note, however, that despite the disappearance

of several interactions at this stage, significant sum and difference interactions involving $f_0 + f_0 \rightarrow 2f_0$ and $2f_0 - f_0 \rightarrow f_0$, respectively, still remain.

Finally, at $Re = 11.0\times10^6$ m^{-1}, significant nonlinear phase-coupled interactions are no longer detected. This could be because any nonlinear interactions present are no longer quadratic, or because the remaining fluctuations are now random. The results collectively suggest that high-frequency nonlinear disturbances are not confined to a small region associated with the breakdown to turbulence, but are present for a significant portion of the laminar boundary-layer development (see Stetson 1988), and can be present when only the second-mode frequency exists in the power spectral density.

Since the main features of the bicoherence distributions portraying the nonlinear coupling mechanisms do not change significantly with unit Reynolds number (as verified by considering other intermediate Reynolds numbers not shown here for brevity), this suggests that the spectral valley filling, and the harmonic generation process, are likely governed by the same generic nonlinear interaction mechanisms. Similar conclusions have been drawn by others who have considered the nonlinear dynamics of transitioning flows (e.g., Miksad *et al*. 1983; Ritz *et al*. 1988). The present nonlinear mechanisms appear to be associated with a redistribution of the available energy in the interacting modes, characterized by the higher-order harmonics gaining enough energy to couple with the second mode to generate even higher harmonics, eventually involving frequency components throughout the whole spectrum. The increased spectral bandwidth of the present results compared to previous studies shows

that these nonlinear interactions involve even higher harmonics of the second-mode disturbance than previously observed.

7.5. Second-mode intermittency and amplitude modulation

It is clear from the above that perfect phase-coupling between all of the interactions is not present at all times. To investigate this intermittency, the temporal evolution of the spectral content may be conveniently described by the short-time FFT (256 samples per Hamming window, 50% overlap). These spectrograms are shown in Figure 7–4(*a–c*) for Re = 10.4, 10.7, and 11.0×10^6 m^{-1}, respectively. From these results, it is clear that the appearance of the second-mode instability, its harmonics, and consequently the spectral redistribution of energy between them become increasingly intermittent with increasing Re. It is believed that this intermittency is not representative of any natural process of breakdown of the flared cone boundary layer, but instead directly results from the rapid onset of heavy intermittency of test environment flow quality as the unit Reynolds number increases. That is, the location of the onset of turbulence on the cone surface is likely intermittently alternating between that for quiet flow ($X_c > 430$ mm) and that for noisy flow ($X_c \approx 280$ mm). For further details on the characterization of the freestream flow, the reader is referred to Section 5 (in particular §5.3.2) for discussion of intermittency.

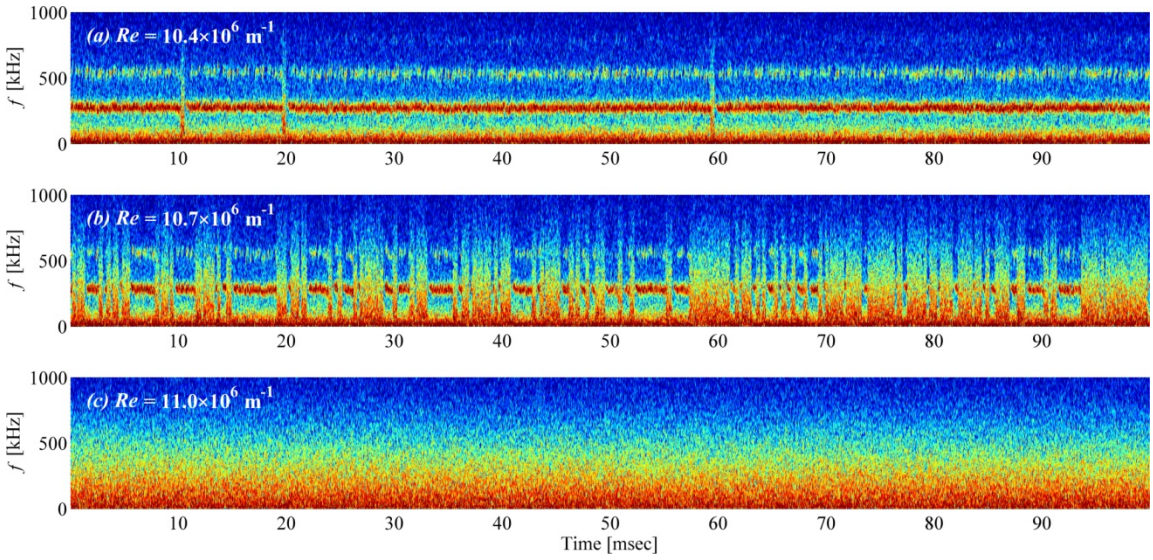

Figure 7–4. Short-time FFT spectrograms of the photodetector signal. X_c = 495 mm. Shown for (*a*) $Re = 10.4\times10^6$ m^{-1}, (*b*) $Re = 10.7\times10^6$ m^{-1}, (*c*) $Re = 11.0\times10^6$ m^{-1}. The freestream condition in (*b*) coincides with the loss of quiet flow in the freestream test environment.

The above intermittency also manifests itself as, or may at least be associated with, an amplitude modulation of the second-mode disturbance. This amplitude modulation may be characterized in more detail by first determining the envelope of the carrier signal. This may be accomplished, among other ways, by creating a complex analytic signal using the Hilbert transform. The real part of the analytic signal is the original signal, and the imaginary part is the Hilbert transform. The signal is band-pass filtered at the carrier frequency f_0 to avoid the demodulation of several signals (using a bandwidth $\Delta f = 20$ kHz, centered on f_0 for each Re), and to focus on the low-frequency amplitude modulations. Figure 7–5(*a*) shows a segment of the Hilbert amplitude, or signal envelope. The second mode disturbance is clearly modulated by amplitudes of various frequencies, which are appreciably lower than f_0 itself.

Premultiplying the usual power spectral density of the signal's envelope by the wavenumber k provides a different interpretation to the results. The usual reason for premultiplying by the wavenumber is to create a logarithmic plot in which equal areas under the graph correspond to equal energies. This stems from the equality: $\int E(k)\, dk = \int kE(k)\, d\log k$; hence, a plot of $kE(k)$ against $\log k$ is variance preserving. This type of representation has been an indispensable tool in turbulence research for investigating large-scale coherent motions, which are typically associated with wavelengths much larger than the boundary-layer thickness (see e.g., Kim & Adrian 1999). In the present study, the abscissa is expressed for convenience in terms of a wavelength $\lambda = 2\pi/k$, normalized by a characteristic length associated with the second mode, in this case 2δ, where δ (= 1.5 mm) is the local boundary-layer thickness (assumed constant in the present study although this does not affect the conclusions drawn). The premultiplied spectra are shown in Figure 7–5(*b*), where all spectra are normalized to unit area, to emphasize their frequency (wavelength) content. The premultiplied spectra were computed from the unamplified, unfiltered signal using a 4096-point FFT with 75% overlap, in order to better resolve the larger wavelengths. The results confirm energetic wavelengths appreciably larger than the one associated with the second mode, implying that the second mode disturbance amplitude is modulated over significantly lower frequencies than f_0. This is consistent with the observations of Chokani (2005), who used complex demodulation to determine his amplitude and phase modulates. A broad range of most-energetic wavelengths are found to occur at around $10\lambda/2\delta$, which corresponds to $O(20)$ kHz. Recognizing a significant variation in amplitude modulation, a typical

wave packet therefore, on average, contains $O(10)$ second mode oscillations. As the *Re* increases, it appears as though energy shifts, within this admittedly narrow *Re* range, from the smaller wavelengths to the larger ones. It is speculated that these modulations are associated with the intermittent nature of the disturbances radiating from the transitioning nozzle-wall boundary layer, and that as the *Re* increases, the attendant increase in intermittency exacerbates the amplitude modulation, thereby reducing the energetic wavelengths of the signal's envelope. However, further work needs to be conducted before any substantial claims can be made.

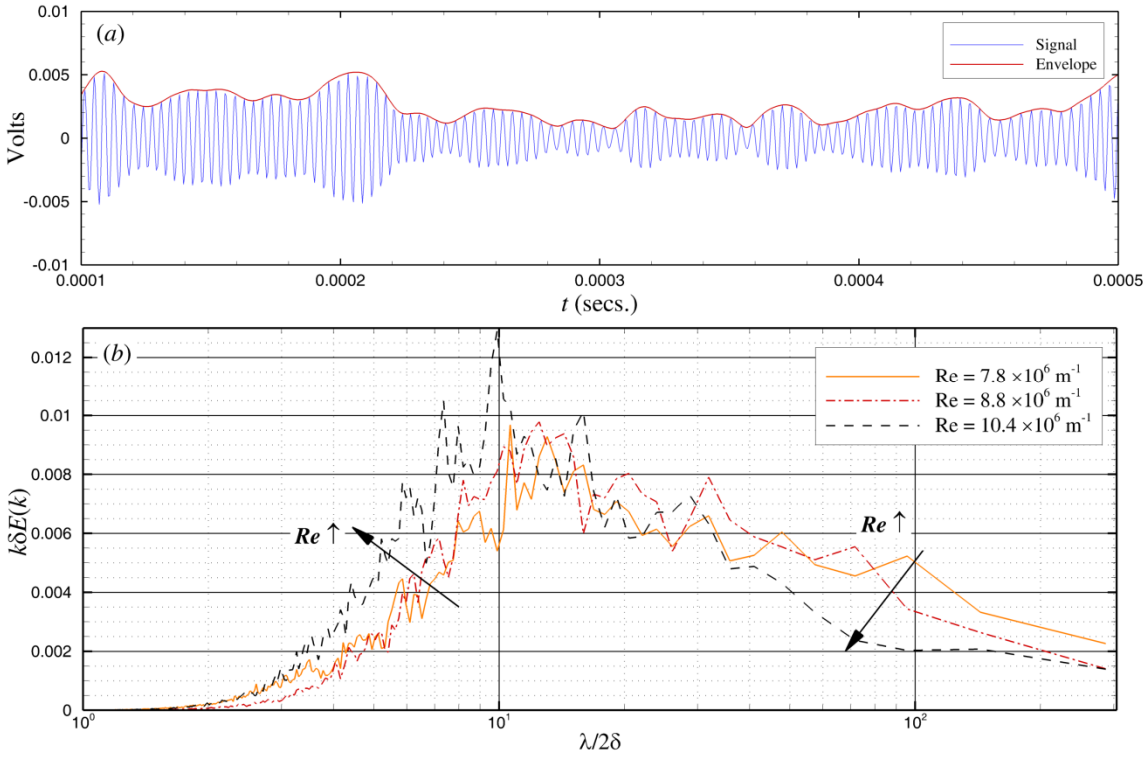

Figure 7–5. Second-mode amplitude modulation analysis. (*a*) Selected portion of the bandpass signal (*blue*) with signal envelope (*red*) for $Re = 10.4\times10^6$ m^{-1}, (*b*) premultiplied power spectrum, $k\delta E(k)$, of the envelope for several *Re*.

8. CONCLUSIONS

It is the objective of this work to experimentally investigate the linear and nonlinear development of the second-mode instability on a sharp, flared cone at Mach 6, for the purposes of providing validation data for computational simulations. As a key component of a larger, integrated theoretical, computational, and experimental effort conducted through the AFOSR/NASA National Center for Hypersonic Laminar-Turbulent Transition Research, this work aims to improve the physics-based understanding of the hypersonic transition process. Such an improved understanding is necessary for the reduction of uncertainty in the prediction of boundary-layer transition, for the application of control techniques, and, ultimately, for the design of more-efficient hypersonic flight and re-entry vehicles.

Due to the high levels of acoustic fluctuations present in the test environment of conventional ground test facilities, it is necessary to conduct the instability experiments in a low-disturbance facility, and, in particular, one with a run time sufficient for the acquisition of hot-wire profiles at constant conditions. A major part of the initial effort for this work, then, is the reconstruction of the Mach 6 Quiet Tunnel (M6QT) formerly of NASA Langley, as well as the establishment of all necessary supporting infrastructure, diagnostics, software, and procedures. The facility now operates as a pressure-vacuum blowdown facility with a nominal 40-second run time at constant conditions.

Prior to the instability experiments, a thorough freestream flow-quality characterization is conducted using Kulite and PCB fast-response pressure transducers. A nominally-quiet ($\tilde{p}_{t2}/\overline{p}_{t2} < 0.1\%$) test environment is present for $Re < 11\times10^6$ m^{-1}. Above this unit Reynolds number, transition on the nozzle wall moves rapidly forward – indicative of a bypass mechanism – and quiet flow is lost. These direct measurements of the freestream flow quality, as well as the observed location of transition onset on the flared cone, indicate that the performance of the facility is remarkably similar to that documented in its former installation at NASA Langley.

With the facility characterized, the NASA Langley 93–10 flared cone model is installed at zero angle of attack, and the development of the second-mode instability is observed for $Re = 10\times10^6$ m^{-1} using constant-temperature hot-wire anemometry. Sensors custom-fabricated for this work exhibit a response up to approximately 330 kHz, and are operated at high overheat ratio to provide data representative of mass flux. The second-mode instability is observed at 250 kHz $< f_0 <$ 310 kHz, and is observed to grow substantially on the aft 20% of the cone's length. Although the hot-wire data presently remain uncalibrated, valuable comparisons to computation and to the original NASA Langley experiments are made. Instability mode shapes predicted by the linear parabolized stability equations (LPSE) agree remarkably well with the experimental profiles of RMS fluctuation in the second-mode passband. Relative growth of the RMS fluctuation notionally agrees with LPSE N-factors, and the most-amplified second-mode frequency, f_0, agrees within 17%. The remaining discrepancy in f_0 is believed to be attributed primarily to a minor misalignment of the cone model, for which the strong

sensitivity is experimentally characterized in a follow-on test series using an optical diagnostic.

This optical diagnostic – a focused schlieren deflectometer – is further optimized to exhibit a remarkable 1 MHz bandwidth and high signal-to-noise ratio for observation of the second-mode instability, and reveals additional insight into its development on the flared cone versus unit *Re*. Two additional harmonics of the second mode are observed near the base of the cone above the noise floor at $2f_0$ and $3f_0$ for $Re > 8\times10^6$ m^{-1} and $Re > 9\times10^6$ m^{-1}, respectively. A bispectral analysis is employed to identify the nonlinear interactions responsible for the development of these harmonics. Several interactions are identified which were not observed in previous hot-wire efforts at NASA Langley due to inadequate sensor bandwidth.

The principal contributions of the work performed for this dissertation are numerous and varied. A new low-disturbance research facility suitable for a wide variety of fundamental studies in the field of hypersonic boundary-layer transition is established, equipped with a diverse suite of research-quality diagnostics, and characterized both through direct measurements of the freestream and by comparison to previously-conducted stability experiments. Comparisons of instability measurements on the flared cone are also made to modern computations from a new parabolized stability equation solver, aiding its ongoing development. Furthermore, the flared-cone experiments conducted expand upon those conducted earlier at NASA Langley, yielding new insight into sensitivity of the second-mode frequency to small angles of attack and into nonlinear interactions of the second mode involving the third harmonic, $3f_0$, which were

unseen by previous hot-wire work. The work additionally sets the stage for the future study of the structure of nonlinear interactions and breakdown of the second-mode in a high-speed equivalent of the classic Klebanoff flat plate experiments.

In order to extend the work in this manner, recommendations for future research in the M6QT are given in the next section, together with additional recommendations for future improvements to the facility and its research diagnostics.

9. RECOMMENDATIONS

Several recommendations are made for the future operation of the M6QT and the studies conducted therein. Below, these recommendations are discussed as they pertain to diagnostics, the facility, and research objectives.

9.1. Diagnostic improvements

Is it strongly recommended that it be a continuing goal for M6QT researchers to further improve its primary research diagnostics. Principally, hot-wire calibration must be implemented, whether accomplished through the use of a separate calibration facility, an in-situ technique, or using a wedge in the M6QT freestream as proposed in Section 4.1.4. This capability is essential to enable proper comparisons to computation for measured boundary-layer profiles and integrated instability growth.

In addition to calibration, the current hot-wire anemometry technique should otherwise be further improved. At the conclusion of this work, several anemometer circuits were returned to the manufacturer for further optimization of their dynamic response, but additional improvements can also be made to the fabrication of the hot-wire probes and sensor elements themselves for both robustness and data quality. Specifically, probe bodies should be further miniaturized and streamlined to minimize their influence in thin boundary layers, and wire sensors should be fabricated with larger aspect ratios and mounted with slack in order to avoid end- and strain-gaging effects.

With regard to pressure measurements, a direct Kulite sensor temperature measurement should be incorporated for explicit zero-shift correction and resulting decrease in uncertainty and of DC pressure and computed quantities like Mach number. Furthermore, ongoing developments in the community toward the calibration of the PCB-132 high-bandwidth sensors for application in quantitative measurement of the second-mode should be monitored and leveraged as appropriate in new test articles.

9.2. Facility and infrastructure

Although the results and conclusions of the freestream characterization of Section 5 are valuable, aspects of the quiet flow performance remain to be investigated, and further study is recommended. For example, it would be instructive to scan additional, off-center planes of the nozzle interior in order to more-rigorously establish the three-dimensional spatial extent of the quiet core at various $Re < 11\times10^6$ m^{-1}. Hot-wire anemometry should also be employed in addition to the Kulite and PCB sensors used for the present work. This would enable the characterization of the mass-flux disturbance environment – including transverse fluctuations $(\rho V)'$ and $(\rho W)'$ as measured with a cross-wire probe – in addition to the acoustic environment, and thus more-completely identify the initial conditions for experiments.

Future experimental work on cone models should be repeated with the model installed at several axial positions in the nozzle in order to explicitly evaluate the effect of the impingement of the radiated acoustic disturbances on the aft portions of the cone.

Additionally, it would be instructive to further study the process of the rapid, complete loss of quiet flow observed for $Re > 11\times10^6$ m^{-1}. For example, hot-film sensors should be employed on the nozzle surface in order to investigate the asymmetry of this process suggested by the present data.

A brief note on operation of the tunnel infrastructure going forward is also in order. At the conclusion of this work, the laboratory's two aging 1960s-era high-pressure compressors were replaced with two brand-new, fully automated CompAir compressors, albeit with significantly reduced capacity. Until additional pumping capacity can be procured and installed, this will reduce the number of full-duration M6QT/ACE tunnel runs achievable in one typical working shift from perhaps 7 to 4. To maximize the productivity of the M6QT and other laboratory facilities within this constraint, it is recommended that future experimental campaigns be planned especially deliberately, executed especially carefully, and scheduled via open communication with other users of the air system. Researchers operating the M6QT and ACE facilities may additionally consider operating in staggered shifts, should safe procedures for doing so be devised. Finally, inexpensive additions and/or modifications to the tunnel heating apparatus and procedure could help matters by reducing the air demands required for the process of pre-heating the tunnels prior to an actual run.

9.3. Research objectives

The natural, recommended extension to the present work is the further study of the nonlinear interactions present at the base of the cone. Recent DNS by

Sivasubramanian & Fasel (2012a, 2012b) as well as recent NPSE by Reed's computational group have revealed the presence of an interaction between the streamwise second-mode fundamental and oblique waves in the form of a fundamental (or Klebanoff-type) resonance. This leads to an azimuthal modulation in the form of *Λ*-vortex structures and streamwise streaks. An initial exploratory experimental campaign has been conducted on the 93–10 flared-cone model using the azimuthal, fixed-height hot-wire-traversing mechanism described in Section 3.2.4. This preliminary work suggests some weak modulation is present at wavenumbers typical of this phenomenon, motivating further study. A full three-axis azimuthal traversing mechanism is being developed, as are methods to introduce patterns of discrete roughness elements in order to encourage the development of interactions at preferred azimuthal wavenumbers. In a sense, this would serve as a novel hypersonic equivalent of the classic experiments of Klebanoff, Tidstrom & Sargent (1962), which used input from a vibrating ribbon and cellophane tape to clarify the three-dimensional nature of the nonlinearities present in flat-plate, incompressible boundary-layer transition.

For this work, it may also prove necessary to obtain larger growth of the second-mode instability within the M6QT test environment, to achieve later-stage nonlinear interactions on the model. This will likely require the use of a different test article geometry. It may be useful in this regard to use the Langley "91–6" cooled cone model (Blanchard and Selby 1996) along with its refrigeration system, and obtain higher *N*-factors through active cooling of the wall. Alternatively, and with less complexity, researchers at Purdue obtain high *N*-factors by using a cone with a continuous circular

arc of a radius chosen to maintain a near-constant boundary-layer thickness on the model and thereby most-strongly excite a single second-mode frequency for the full length of the model. It has been proposed that the two groups work together to design a single test article geometry which can be studied with similar diagnostics in each of the two hypersonic quiet tunnels and other conventional facilities. Performing common experiments such as this is strongly recommended by the Transition Study Group (Reshotko 1976) in order to best understand facility effects and provide context for the overall conclusions.

Finally, there remains tremendous opportunity to expand beyond the second-mode subject matter of the original Lachowicz, Doggett, and Blanchard studies at NASA Langley and, for the first time, apply the M6QT's extended-duration quiet flow capability both to parametric surveys and detailed studies of other instability mechanisms. As a first step, experiments are being prepared now which will soon study transient growth due to roughness on a blunted 5º-half-angle cone and crossflow on the now-canonical 7º-half-angle sharp cone at 6º angle-of-attack. These efforts will include controlled disturbance input via prescribed roughness, discrete roughness elements, and/or plasma actuators, and will be conducted with strong cooperation with computational efforts.

REFERENCES

ABNEY, A., WARD, C., BERRIDGE, D. C., GREENWOOD, R., and SCHNEIDER, S. P. 2013. Hypersonic Boundary-Layer Transition Experiments in the Boeing/AFOSR Mach-6 Quiet Tunnel. *AIAA Paper 2013–0375.*

ANDERS, J. B., STAINBACK, P. C., KEEFE, L. R., and BECKWITH, I. E. 1977. Fluctuating Disturbances in a Mach 5 Wind Tunnel. *AIAA J.* **15**(8):1123–1129.

BECKWITH, I. E., HARVEY, W. D., HARRIS, J. E., and HOLLEY, B. B. 1973. Control of Supersonic Wind Tunnel Noise by Laminarization of Nozzle-Wall Boundary Layers. *NASA Technical Report TM-X-2879.*

BECKWITH, I. E. 1975. Development of a High Reynolds Number Quiet Tunnel for Transition Research. *AIAA J.* **13**(3):300–306.

BECKWITH, I. E., CHEN, F.-J., and MALIK, M. R. 1988. Design and Fabrication Requirements for Low-Noise Supersonic/Hypersonic Wind Tunnels. *AIAA Paper* 1988–0143.

BERRIDGE, D. C. 2010. *Measurements of Second-Mode Instability Waves in a Hypersonic Boundary Layers with a High-Frequency Pressure Transducer.* M.S. Thesis. Purdue University, West Lafayette, Indiana.

BERRIDGE, D. C., CHOU, A., WARD, C. A. C., STEEN, L. E., GILBERT, P. L., JULIANO, T. J., SCHNEIDER, S. P., and GRONVALL, J. E. 2010. Hypersonic Boundary-Layer Transition Experiments in a Mach-6 Quiet Tunnel. *AIAA Paper 2010–1061.*

BLANCHARD, A. E. and SELBY, G. V. 1996. An Experimental Investigation of Wall-Cooling Effects on Hypersonic Boundary-Layer Stability in a Quiet Wind Tunnel. NASA CR 198287.

BLANCHARD, A. E., LACHOWICZ, J. T., and WILKINSON, S. P. 1997. NASA Langley Mach 6 Quiet Wind-Tunnel Performance. *AIAA J.* **35**(1):23–28.

BOEDEKER, L. R. 1959. *Analysis and Construction of a Sharp Focussing Schlieren System*. M.S. Thesis. Massachusetts Institute of Technology, Cambridge, Massachusetts.

BOWERSOX, R. D. W. 1992. *Compressible Turbulence in a High-Speed High Reynolds Number Mixing Layer.* Ph. D. Dissertation. Virginia Polytechnic Institute and State University, Blacksburg, Virginia.

BURTON, R. A. 1949. A Modified Schlieren Apparatus for Large Areas of Field. *J. Optical Society of America* **39**(11):907–908.

CHEN F.-J., WILKINSON S. P., and BECKWITH, I. E. 1993. Görtler Instability and Hypersonic Quiet Nozzle Design. *J. Spacecraft and Rockets* **30**(2):170–175.

CHOKANI, N. D. 1999. Nonlinear Spectral Dynamics of Hypersonic Boundary Layer Flow. *Phys. Fluids* **11**(12):3846–3851.

CHOKANI, N. D. 2001. Perspective: Stability Experiments at Hypersonic Speeds in a Quiet Wind Tunnel (Invited). *AIAA Paper 2001–0211.*

CHOKANI, N. D. 2005. Nonlinear Evolution of Mack Modes. *Phys. Fluids* **17**(1):014102.

DEMETRIADES, A. 1974. Hypersonic Viscous Flow Over a Slender Cone Part III: Laminar Instability and Transition. *AIAA Paper 1974–0535.*

DOGGETT, G. P. 1996. *Hypersonic Boundary-Layer Stability on a Flared-Cone Model at Angle of Attack*. Ph.D. Dissertation, Mechanical and Aerospace Engineering Dept., North Carolina State University, Raleigh, North Carolina.

FEDOROV, A. 2011. Transition and Stability of High-Speed Boundary Layers. *Ann. Rev. Fluid Mech.* **43:**79–95.

FEDOROV, A., TUMIN, A. 2011. High-Speed Boundary-Layer Instability: Old Terminology and a New Framework. *AIAA J.* **49**(8):1647–1657.

FISH, R. W. and PARNHAM, K. 1950. Focussing Schlieren Systems. Report CP-54, British Aeronautical Research Council.

HINICH, M. J. and WOLINSKY, M. 2005. Normalizing Bispectra. *J. Statistical Planning and Inference* **130**:405–411.

HOFFERTH, J. W. and SARIC, W. S. 2012. Boundary-Layer Transition on a Flared Cone in the Texas A&M Mach 6 Quiet Tunnel. *AIAA Paper 2012–0923.*

HOFFERTH, J. W., HUMBLE, R. A., FLORYAN, D. C., and SARIC, W. S. 2013a. High-Bandwidth Optical Measurements of the Second-Mode Instability in a Mach 6 Quiet Wind Tunnel. *AIAA Paper 2013–0378.*

HOFFERTH, J. W., SARIC, W. S., KUEHL, J., PEREZ, E., KOCIAN, T., and REED, H. L. 2013b. Boundary-Layer Instability and Transition on a Flared Cone in a Mach 6 Quiet Wind Tunnel. *Int. J. Eng. Sys. Modelling and Simulation* **5**(1/2/3):109–124.

HORVATH, T. J., BERRY, S. A., HOLLIS, B. R., CHANG, C. L. and SINGER, B. A. 2002. Boundary-Layer Transition on Slender Cones in Conventional and Low Disturbance Mach 6 Wind Tunnels. *AIAA Paper 2002–2743.*

KANTROWITZ, A. and TRIMPI, R. L. 1950. A Sharp-Focusing Schlieren System. *J. Aero. Sci.* **17**:311-319.

KEGERISE, M. A. and SPINA, E. F. 2000a. A Comparative Study of Constant-Voltage and Constant-Temperature Hot-Wire Anemometers: Part I – The Static Response. *Exps. Fluids* **29**:154–164.

KEGERISE, M. A. and SPINA, E. F. 2000b. A Comparative Study of Constant-Voltage and Constant-Temperature Hot-Wire Anemometers: Part II – The Dynamic Response. *Exps. Fluids* **29**:165–177.

KENDALL, J. M. 1957. An Experimental Investigation of Leading Edge Shock-Wave – Boundary-Layer Interaction at Mach 5.8. *J. Aero. Sci.* **24**(1):47–56.

KENDALL, J. M. 1975. Wind Tunnel Experiments Relating to Supersonic and Hypersonic Boundary-Layer Transition. *AIAA J.* **13**(3):290–299.

KIM, K. C. and ADRIAN, R. J. 1999. Very Large-Scale Motion in the Outer Layer. *Phys. Fluids* **11**:417–422.

KIM, Y. C. and POWERS, E. J. 1979. Digital Bispectral Analysis and its Applications to Nonlinear Wave Interactions. *IEEE Trans. Plasma Science* **7**:120–131.

KIMMEL, R. L. and KENDALL, J. M. 1991. Nonlinear Disturbances in a Hypersonic Boundary Layer. *AIAA Paper 1991–0320*.

KLEBANOFF, P. S., TIDSTROM, K. D., and SARGENT, L. M. 1962. The Three-Dimensional Nature of Boundary-Layer Instability. *J. Fluid Mech.* **12**(1):1–34.

KOVASZNAY, L. S. G. 1950. The Hot-Wire Anemometer in Supersonic Flow. *J. Aero. Sci.* **17**(9):565–572.

KOVASZNAY, L. S. G. 1953. Turbulence in Supersonic Flow. *J. Aero. Sci.* **20**(10):657–674.

KUEHL, J. J., PEREZ, E., and REED, H. L. 2012. JoKHeR: NPSE Simulations of Hypersonic Crossflow Instability. *AIAA Paper 2012–0921.*

LACHOWICZ, J. T. 1995. *Hypersonic Boundary Layer Stability Experiments in a Quiet Wind Tunnel with Bluntness Effects.* Ph.D. Dissertation, Mechanical and Aerospace Engineering Dept., North Carolina State University, Raleigh, North Carolina.

LACHOWICZ, J. T., CHOKANI, N. D., and WILKINSON, S. P. 1996. Boundary Layer Stability Measurements in a Hypersonic Quiet Tunnel. *AIAA J.* **34**(12):2496–2500.

LAUFER, J. 1961. Aerodynamic Noise in Supersonic Wind Tunnels. *J. Aero. Sci.* **28**(9):685–692.

LAURENCE, S. J., WAGNER, A., and HANNEMANN, K. 2012. Time-Resolved Visualization of Instability Waves in a Hypersonic Boundary Layer. *AIAA J*. **50**:243–246.

LIN, T. C. 2008. Influence of Laminar Boundary-Layer Transition on Entry Vehicle Designs. *J. Spacecraft and Rockets* **45**(2):165–175.

MACK, L. M. 1984. Boundary-Layer Stability Theory. *AGARD Rep. No. 709*, Von Karman Inst., Rhode-St.-Genese, Belg.

MATLIS, E. H. 2003. *Controlled Experiments on Instabilities and Transition to Turbulence on a Sharp Cone at Mach 3.5.* Ph.D. Dissertation. Notre Dame University, South Bend, Indiana.

MORKOVIN, M. V. 1959. On Supersonic Wind Tunnels with Low Free-Stream Disturbances. *J. Applied Mechanics* **26**:319–324.

MORKOVIN, M. V. 1969. Critical Evaluation Of Transition From Laminar To Turbulent Shear Layers With Emphasis On Hypersonically Traveling Bodies. *Air Force Flight Dyn. Lab. Rep.* AFFDL-TR-68-149, Baltimore, MD.

MORKOVIN, M. V., RESHOTKO, E., and HEBERT, T. 1994. Transition in Open Flow Systems: a Reassessment. *Bull. APS.* **39**(9):1–31.

MIKSAD, R. W., JONES, F. L., and POWERS, E. J. 1983. Measurements of Nonlinear Interactions during Natural Transition of a Symmetric Wake. *Phys. Fluids* **26**:1402–1409.

OWENS, L. R., KEGERISE, M. A., and WILKINSON, S. P. 2011. Off-Body Boundary-Layer Measurement Techniques Development for Supersonic Low-Disturbance Flows. *AIAA Paper 2011-0284.*

PARZIALE, N. J., SHEPHERD, J. E., and HORNUNG, H. G. 2012. Geometric Acoustics in a Hypervelocity Boundary Layer. *International Workshop on Hypersonic Stability and Transition.* Sedona, Arizona. Oral presentation. October 2012.

PATE, S. R. and SCHUELER, C. J. 1969. Radiated Aerodynamic Noise Effects on Boundary-Layer Transition in Supersonic and Hypersonic Wind Tunnels. *AIAA J.* **7**(3):450–457.

PATE, S. R. 1971. Measurements and Correlations of Transition Reynolds Numbers on Sharp Slender Cones at High Speeds. *AIAA J.* **9**(6):1082–1090.

PATE, S. R. 1978. Dominance of Radiated Aerodynamic Noise on Boundary-Layer Transition in Supersonic-Hypersonic Wind Tunnels – Theory and Application. *Arnold Engineering Development Center. Arnold Air Force Station, TN.* AEDC-TR-77-107.

PEREZ, E., KOCIAN, T. S., KUEHL, J. J. and REED, H. L. 2012. Stability of Hypersonic Compression Cones. *AIAA Paper 2012–2962.*

POPE, A. and GOIN, K. 1965. *High Speed Wind Tunnel Testing.* Wiley, New York.

REDA, D. C. 1979. Boundary-Layer Transition Experiments on Sharp, Slender Cones in Supersonic Free Flight. *AIAA J.* **17**(8):803–810.

REED, H. L., SARIC, W. S., and ARNAL, D. 1996. Linear Stability Theory Applied to Boundary Layers. *Ann. Rev. Fluid Mech.* **28**:389–428.

REED, H. L., KIMMEL, R., SCHNEIDER, S. P., and ARNAL, D. 1997. Drag Prediction and Transition in Hypersonic Flow. *AIAA Paper 1997–1818.*

REED, H. L., KUEHL, J. J., PEREZ, E., KOCIAN, T., HOFFERTH, J. W., and SARIC, W. S. 2012. Nonlinear Parabolized Stability Equation Simulations in Hypersonic Flows. *Presented at RTO AVT-200 Symposium, April 2012. Paper 7.*

RESHOTKO, E. 1976. Boundary-Layer Stability and Transition. *Ann. Rev. Fluid Mech.* **8**:311–349.

RESHOTKO, E. 2007. Is Re_θ/M_e a Meaningful Transition Criterion? *AIAA J.* **45**(7):1441–1443.

RITZ, CH. P., POWERS, E. J., MIKSAD, R.W. and SOLIS, R. S. 1988. Nonlinear Spectral Dynamics Of A Transitioning Flow. *Phys. Fluids* **31**:3577–3588.

ROOD, R., GRIFFITH, C., ENGELHAUPT, D., and CERNOSEK, J. 1992. Mach 6 Electroformed Nickel Nozzle Refurbishment: FNAS Investigation of Ultra-Smooth Surfaces. Internal Report, University of Alabama, Huntsville, Alabama. NAS8-38609. UAH D.O. 007, 5–32762.

SARIC, W. S. 1994. Görtler Vortices. *Ann. Rev. Fluid Mech.* **26**:379–409.

SARIC, W. S., REED, H. L., and KERSCHEN, E. J. 2002. Boundary-Layer Receptivity to Freestream Disturbances. *Ann. Rev. Fluid Mech.* **34**:291–314.

SARIC, W. S. 2012. AFOSR/NASA National Science Center for Hypersonic Laminar-Turbulent Transition. *Presented at RTO AVT-200 Symposium, April 2012. Paper No. 5.*

SCHARDIN, H. 1942. Die Schlierenverfahren une ihre Anwendungen. *Ergebnisse der Exakten Naturwissenschaften*, **20**:303–439. English translation available as NASA TT F-12731, April 1970 (N70-25586).

SCHNEIDER, S. P. 1998. Design of a Mach-6 Quiet-Flow Wind Tunnel Using the e**N Method for Transition Estimation. *AIAA Paper 1998–0547.*

SCHNEIDER, S. P. 2001. Effects of High-Speed Tunnel Noise on Laminar-Turbulent Transition. *J. Spacecraft and Rockets* **38**(3):323–333.

SCHNEIDER, S. P. 2008. The Development of Hypersonic Quiet Tunnels. *J. Spacecraft and Rockets* **45**(4):641–664.

SEMPER, M. S., TICHENOR, N., BOWERSOX, R. D. W., SRINVASAN, R., and NORTH, S. 2009. On the Design and Calibration of an Actively Controlled Expansion Hypersonic Wind Tunnel. *AIAA Paper 2009–0799.*

SIVASUBRAMANIAN, J. and FASEL, H. F. 2012a. Growth and Breakdown of a Wave Packet into a Turbulent Spot in a Cone Boundary Layer at Mach 6. *AIAA Paper 2012–0085.*

SIVASUBRAMANIAN, J. and FASEL, H. F. 2012b. Nonlinear Stages of Transition and Breakdown in a Boundary Layer on a Sharp Cone at Mach 6. *AIAA Paper 2012–0087.*

SMITS, A. J., HAWAKAWA, K., and MUCK, C. K. 1983. Constant-Temperature Hot-Wire Anemometer Practice in Supersonic Flows – Part 1: The Normal Wire. *Exps. Fluids* **1**:83–92

SMITS, A. J. and DUSSAUGE, J-P. 1989. Hot-Wire Anemometry in Supersonic Flow. *AGARD No. 315, Chapt. 5.*

STEEN, L. E. 2010. *Characterization and Development of Nozzles for a Hypersonic Quiet Wind Tunnel*. M.S. Thesis. Purdue University, West Lafayette, Indiana.

STETSON, K. F., THOMPSON, E. R., DONALDSON, J. C., and SILER, L. G. 1983. Laminar Boundary-Layer Stability Experiments on a Cone at Mach 8, Part 1: Sharp Cone. *AIAA Paper 1983–1761.*

STETSON, K. F. 1988. On Nonlinear Aspects of Hypersonic Boundary-Layer Stability. *AIAA J.* **26**(7):883–885.

VANDERCREEK, C. P. 2010. *Hypersonic Application of Focused Schlieren and Deflectometry*. M.S. Thesis. University of Maryland, College Park, Maryland.

WEINSTEIN, L. M. 1993. Large-Field High-Brightness Focusing Schlieren System. *AIAA J.* **31**(7):1250–1255.

WHEATON, B. M. 2010. Aerotech Low-Noise Traverse System. Purdue University internal report obtained via personal communication, July 2010.

WHEATON, B. M. and SCHNEIDER, S. P. 2012. Roughness-Induced Instability in a Hypersonic Laminar Boundary Layer. *AIAA J.* **50**(6):1245–1256.

WILKINSON, S. P., ANDERS, S. G., and CHEN, F.-J. 1992. Supersonic and Hypersonic Quiet Tunnel Technology at NASA Langley. *AIAA Paper 1992–3908.*

WILKINSON, S. P., ANDERS, S. G., and CHEN, F.-J. 1994. Status of NASA Langley Quiet Flow Facility Developments. *AIAA Paper 1994–2498.*

WILKINSON, S. P. 1997. A Review of Hypersonic Boundary Layer Stability Experiments in a Quiet Mach 6 Wind Tunnel. *AIAA Paper 1997–1819.*